Búsquedas fenomenológicas de Nueva Física en los sectores del quark top y un bosón Z' en el LHC

Por

ROSA MARÍA SANDÁ SEOANE

Universidad Nacional de San Martín

UNIVERSIDAD DE SAN MARTÍN
COMISIÓN NACIONAL DE ENERGÍA ATÓMICA
INSTITUTO DE TECNOLOGÍA PROF. JORGE A. SÁBATO

Tesis para optar al título de Doctora en Ciencia y Tecnología,
Mención Física

Director:
Dr. Ezequiel Álvarez

2021

Phenomenological New Physics searches in top and Z' sectors at the LHC

By

Rosa María Sandá Seoane

Universidad Nacional de San Martín

Universidad de San Martín
Comisión Nacional de Energía Atómica
Instituto de Tecnología Prof. Jorge A. Sábato

Thesis submitted for the degree of Doctor in Science and Technology, Physics

Advisor:
Dr. Ezequiel Álvarez

2021

Atención pido al silencio
y silencio a la atención,
que voy en esta ocasión,
si me ayuda la memoria,
a mostrarles que a mi historia
le faltaba lo mejor.

José Hernández. *La vuelta de Martín Fierro.*

Para mi abuela Diana y su pequeña y adorada Rosita, que pasaba tardes enteras con ella en la cocina.

Resumen

A través de los últimos años, los avances logrados en el campo experimental de la Física de partículas, asociados a los logros en el Gran Colisionador de Hadrones (o LHC, su sigla en inglés por *Large Hadron Collider*), han permitido testear como nunca antes al Modelo Estándar (ME). Las predicciones de este modelo se han medido y validado con una precisión sin precedentes, y, sin embargo, la cantidad de fenómenos no explicados y los interrogantes acerca de su extructura no dejan de exhibirla como una teoría efectiva hasta las energías exploradas. La búsqueda de Nueva Física (NF) es uno de los programas claves en el LHC, pero ante resultados que no dan pistas sobre el camino a seguir, las propuestas fenomenológicas cobran mayor relevancia. Estas propuestas pueden resultar fundamentales en los años venideros, no solo para trazar nuevos caminos de búsqueda y para poner límites a teorías más allá del ME, a través de experimentos de detección directa de partículas hipotéticas, sino también para proponer nuevos observables para la detección indirecta de NF que pueda llegar a haber pasado inadvertida hasta la fecha.

Esta tesis presenta una serie de estudios fenomológicos que cubren separadamente las dos líneas de detección de NF anteriormente mencionadas. En el marco de la detección indirecta, presentamos un estudio de la producción de cuatro tops en el LHC como posible prueba de NF liviana y top-fílica. Aprovechando la oportunidad dada al quark top en numeras extensiones del ME como posible mediador a sectores desconocidos de partículas, por ser la partícula más pesada hasta ahora encontrada, estudiamos el impacto en la producción de cuatro tops de la presencia de posibles nuevas partículas de espín 0, 1 o 2, cuyas masas están por debajo de la producción de pares de tops. Proponemos una serie de nuevos observables que identifican y distinguen entre dichas señales, que deben ser tenidos en cuenta en las estrategias venideras para la medición de cuatro tops en el LHC. Por otro lado, en el marco de los experimentos de detección directa, nos centramos en el bosón Z', un mediador hipotético que aparece en una gran variedad de modelos de NF, y teniendo en cuenta el número de búsquedas de Z' que se han llevado a cabo en el LHC, presentamos un software, Z'-explorer, para probar fácilmente modelos de Z' contra todos estos resultados para canales visibles. Simplemente proporcionando acoplamientos y anchos de decaimiento (o alternativamente, la sección eficaz de producción y la tasa de decaimiento para cada canal visible), Z'-explorer permite probar un modelo dado, determinando el canal más sensible para la exclusión/detección de un Z' dado dentro el espacio de parámetros de NF, erigiéndose como una herramienta fenomológica de enlace entre teoría y experimentos. Finalmente, y para incluir la fenomenología que proporciona la interacción con otros sectores escondidos, presentamos además una actualización del software, Z'-explorer 2.0, que incluye las búsquedas en el LHC de bosones Z' acoplando a materia oscura fermiónica. A través de esta propuesta, también exponemos los principales aspectos de la fenomenología de nuevas partículas decayendo en especies invisibles.

Abstract

Over the last few years, the advances made in the experimental field of particle physics, associated with the achievements at the LHC, have allowed the Standard Model to be tested like never before. The predictions of this model have been measured and validated with unprecedented precision, and yet the number of unexplained phenomena and questions about its structure does not stop exhibiting it as an effective theory up to the energies explored. The search for New Physics is one of the key programs at the LHC, but in the face of results that do not give any clue about the way forward, the phenomenological proposals become more relevant. These proposals may prove fundamental in the upcoming years, not only for tracing new search paths and setting bounds to Beyond Standard Model theories through hypothetical direct particle detection experiments but also for proposing new observables for the indirect detection of New Physics that may have gone unnoticed to date.

This thesis presents a series of phenomenological studies that cover separately the two lines of detection of New Physics above-mentioned. In the framework of indirect detection, we present a study of four-top production at the LHC as possible evidence of light top-philic New Physics. Taking advantage of the opportunity given to the top quark in numerous extensions of the Standard Model as a possible mediator to unknown sectors of particles, as it is the heaviest particle ever found, we study through simplified models the impact on the production of four-tops of the presence of possible new particles of spin-0, 1 or 2, whose masses are below top-pair production threshold. We propose a series of new observables that identify and distinguish between these signatures, which should be taken into account in future strategies for measuring four-tops at the LHC. On the other hand, in the framework of direct detection experiments, we focused on Z' boson, a hypothetical mediator that appears in a large variety of New Physics models, and, taking into account the numerous Z' searches that have been carried out at the LHC, we present a software, Z'-explorer, to easily test Z' models against all the available visible data. By providing couplings and partial widths (or alternatively the production cross-section and branching ratios to each visible channel), Z'-explorer allows testing a given model, determining the most sensitive channel for the exclusion/detection of a given Z' within the New Physics parameter space, emerging as a phenomenological link between theory and experiments. Finally, and to include the phenomenology that provides the interaction with other hidden sectors, we also present a software update, Z'-explorer 2.0, which includes searches at the LHC of Z' coupling to fermionic Dark Matter. Through this proposal, we also expose the main aspects of the phenomenology of new particles decaying into invisible species.

Agradecimientos

Acorde a una tesis de doctorado, corresponde que agradezca primeramente al CONICET, al Instituto Sábato, a la UNSAM, al ICAS y a mi director, responsables primarixs de mi formación como doctoranda y de que este trabajo esté finalizado.

Siendo una descreída de la meritocracia, siempre me gusta resaltar que en la vida, para tener éxito cuando se encara una empresa, además del esfuerzo, se tienen que garantizar un montón de condiciones externas y/o relacionadas a la cuestión en sí, que mayormente escapan a nuestro control. Así que el hecho de ser hoy una privilegiada por tener la posibilidad de presentar este trabajo, también se lo debo a muchas personas que confabularon directa o indirectamente para que esto suceda.

Primeramente agradezco a mi familia, en especial a mi mamá por ser la cara de mi hogar estable, y a mi papá (que lamentablemente no pudo llegar a verme defender esta tesis pero andará en algún plano reventado de orgullo), por haberme ayudado todo este tiempo a achicar mi desventaja desde que decidí continuar en una carrera que al día de hoy sigue siendo para unxs pocxs. A Marina y Jorge, por preocuparse y mimarme más de un fin de semana. A mi rey, Brian, por alegrarme el corazón más de una tarde cuando volvía de la oficina, y por recordarme siempre el amor más puro y fiel. Pero el agradecimiento más grande de todos se lo debo a él, Diego, mi compañero de vida desde hace ocho años ya. No hay palabras que resuman por qué una parte de esta tesis es estrictamente tuya, y lo que significás para mí. La vida es más linda con vos al lado.

También quiero agradecer a mis amigxs, por bancarme en todas y por la incondicionalidad de siempre. Y obviamente no puedo dejar de agradecer a lxs que fueron testigos diarixs de mi paso por la oficina de becarixs y mi trabajo. En particular, a Pablo y Leonel, por haber sido de lxs que me mostraron la cara más amable y cálida en el día a día en la oficina. Pero el reconocimiento mayor se lo llevan ellas, Rocío y Mariel, a las que tengo el placer de llamar mis amigas. Tenerlas a ustedes dos de compañeras y compinches es uno de los grandes regalos que me dió el doctorado, le dieron color a mis mañanas y tardes en el ICAS. Tampoco quiero dejar de agradecer a José y Víctor, mis nuevos colaboradores desde que llegó la pandemia, que me ayudaron en todo lo que estuvo a su alcance, pese a la distancia y la virtualidad.

Y no podía faltar el agradecimiento a mi abuela Diana. Más pasan los años y más me doy cuenta que esa fortaleza implacable por avanzar en este mundo de varones y ser sorora la heredé de vos.

Table of Contents

Page

Chapter 1

The Standard Model

En física de partículas, el Modelo Estándar (ME) es el nombre de la teoría cuántica de campos que, al día de la fecha, mejor describe la estructura fundamental de la materia, como asimismo explica 3 de las 4 fuerzas fundamentales conocidas: la fuerza electromagnética, la fuerza débil y la fuerza fuerte. Desde su desarollo formal a principios de los años '70, los resultados experimentales reportados condicen firmemente con sus predicciones, erigiéndola hasta el momento como la teoría más satisfactoria para explicar la naturaleza de todo lo que existe en nuestro universo.

Basado en las ideas de unificación y simetría, el ME propone un lagrangiano de Dirac donde los quarks y los leptones son los objetos fundamentales que componen a la materia. Con el fin de representar a las fuerzas que afectan a estos campos de materia, 3 simetrías locales son necesarias, correspondientes a pedir invariacia frente a las transformaciones del grupo $SU(3) \otimes SU(2) \otimes U(1)$. Así, al reescribir la derivada covariante del lagrangiano de partícula libre, como consecuencia de las invariancias de gauge impuestas, las fuerzas fundamentales quedan representadas como una interacción entre los campos de materia dada a través del intercambio de los llamados bosones de gauge. Sumando al lagrangiano un campo escalar, el campo de Higgs, y su potencial correspondiente, para poder dar masa a todas las partículas elementales (más precisamente, a los fermiones y a los bosones de las interacciones débiles) a través del llamado mecanismo de Higgs, se completa el lagrangiano de la teoría, que se desarrolla en detalle y por partes en las próximas secciones. Dentro de este capítulo, también exponemos algunos fenómenos no explicados y preguntas abiertas que señalan al ME como una teoría efectiva.

In particle physics, the Standard Model (SM) is the name of the quantum field theory that best describes to date the fundamental structure of matter, as it also explains three of the four known fundamental forces: the electromagnetic force, the weak force and the strong force. Since its formal development in the early 1970s, the reported experimental results firmly agree with its predictions, making it the most satisfactory theory so far to explain the nature of everything that exists in our universe.

Based on the ideas of unification and symmetry, the SM proposes a Dirac Lagrangian where quarks and leptons are the fundamental objects that constitute matter. To represent the forces that affect these fields, three local symmetries are necessary, corresponding to request invariance against the transformations of the group $SU_c(3) \otimes SU_L(2) \otimes U_Y(1)$. Thus, when rewriting the covariant derivative of the free particle Lagrangian, as a consequence of the imposed gauge invariances, the fundamental forces are represented as an interaction between the fields of matter given through the exchange of the so-called gauge bosons. Adding to the Lagrangian a scalar field, the Higgs boson, and its corresponding potential, to be able to give mass to all elementary particles (more precisely, to fermions and bosons of weak interactions) through the so-called Higgs mechanism, completes the Lagrangian of the theory, which is developed in detail in parts in the next sections. Within this chapter, we also exposed some remaining questions and unexplained phenomena that point out the SM as an effective theory.

1.1 Symmetry $SU_c(3)$: QCD

The strong nuclear force is responsible for holding together the nucleons (protons and neutrons) that coexist in atomic nuclei, defeating electromagnetic repulsion. Its associated theory is called Quantum Chromodynamics (QCD), named that way for the quantum number effectively introduced to explain this interaction: the color charge. In this theory, quarks, in addition to having an electric charge, have a color charge, and can assume one of three primary colors: red (R), green (G), or blue (B). Antiquarks, meanwhile, are charged with complementary colors: cyan ($\overline{R}$), magenta ($\overline{G}$), and yellow ($\overline{B}$), but for simplification, they can be thought of as anti-colors. The spectrum of hadrons observed in nature is explained by adding that all the particles must be white or colorless (that is, invariant before rotations in the space R, G, B). The color is exchanged thanks to eight different gluons, mediators of the strong interaction, which are bicolored (with color charge and anti-charge), electrically neutral, and massless.

In formal terms, QCD is associated with a local color symmetry $SU_c(3)$ of the Lagrangian of the quarks, symmetry from which arise naturally the boson fields which represent the mediators of this force, the gluons. The Lagrangian for any free quark is defined as [1, 2]

$$\mathscr{L} = \overline{q}(i\gamma^{\mu}\partial_{\mu} - m)q \tag{1.1}$$

where q represents a triple of Dirac spinors, one for each color field

$$q = \begin{pmatrix} q_R \\ q_G \\ q_B \end{pmatrix} \tag{1.2}$$

Require for local symmetry of type $SU(3)$ is equivalent to ask for invariance against transformations of the type

$$q(x) \longrightarrow Uq(x) \equiv e^{i\alpha^a(x)T_a}q(x) \tag{1.3}$$

where T^a, with $a = 1, 2, ..., 8$ are linearly independent 3×3 matrices with zero trace, which are the generators of the symmetry group $SU(3)$. The group is non-abelian since not all generators T^a commute with each other, but instead verify the following commutation relationship

$$[T_a, T_b] = i f_{abc} T_c \tag{1.4}$$

with f_{abc} real numbers, known as the structure coefficients of the group. Consequently, $T^a = \lambda^a/2$ is conventionally used, where λ^a is each of the so-called Gell-Mann matrices.

The required invariance in (1.3) is obtained by replacing the covariant derivative ∂_μ by

$$D_\mu \equiv \partial_\mu + i g_s T_a G^a_\mu \tag{1.5}$$

which allows to introduce the eight gauge fields G^a_μ (the gluons) and the strong coupling g_s. If the infinitesimal version of the transformation U is considered in (1.3)

$$U = 1 + i\alpha_a T_a \tag{1.6}$$

it is obtained that the gauge bosons transform like

$$G^a_\mu \longrightarrow G^a_\mu - \frac{1}{g_s}\partial_\mu \alpha_a - f_{abc}\alpha_b G^c_\mu \tag{1.7}$$

Adding also to the Lagrangian the Lorentz invariant kinetic term associated to the gauge boson fields G^a_μ, finally the QCD Lagrangian can be written as

$$\mathscr{L} = \overline{q}(i\gamma^{\mu}\partial_{\mu} - m)q - g_s(\overline{q}\gamma^{\mu}T_a q)G^a_{\mu} - \frac{1}{4}G^a_{\mu\nu}G^{\mu\nu}_a \tag{1.8}$$

with

$$G^a_{\mu\nu} = \partial_{\mu}G^a_{\nu} - \partial_{\nu}G^a_{\mu} - g_s f_{abc}G^b_{\mu}G^c_{\nu} \tag{1.9}$$

defined that way to respect the transformation in (1.7) and thus achieve the desired gauge invariance in (1.8). It is worth mention that as a consequence of the symmetry group being non-abelian, in (1.8) not only are explicit interaction terms between quarks and gluons but also there are autointeraction terms of the gauge fields, that is, vertices of three and four interacting gluons (with conservation of color charge).

1.2 Symmetry $SU_L(2)\otimes U_Y(1)$: Electroweak unification

The weak force is the interaction between subatomic particles that causes radioactive decay. Experimentally, it is observed that weak interactions occur only between leptons of the same generation, where each of them can be represented as a doublet

$$\begin{pmatrix} \nu_e \\ e \end{pmatrix}\begin{pmatrix} \nu_{\mu} \\ \mu \end{pmatrix}\begin{pmatrix} \nu_{\tau} \\ \tau \end{pmatrix} \tag{1.10}$$

while weak interactions between quarks can occur between pairs of any of the following doublets

$$\begin{pmatrix} u \\ d' \end{pmatrix}\begin{pmatrix} c \\ s' \end{pmatrix}\begin{pmatrix} t \\ b' \end{pmatrix} \tag{1.11}$$

where d', s' and b' are related to d, s and b quarks trought the unitary CKM matrix (in honour to Cabibbo, Kobayashi and Maskawa)[3]

$$\begin{pmatrix} d' \\ s' \\ b' \end{pmatrix} = \begin{pmatrix} V_{ud} \sim 1 & V_{us} \sim 0.2 & V_{ub} \sim 0.003 \\ V_{cd} \sim 0.2 & V_{cs} \sim 1 & V_{cb} \sim 0.04 \\ V_{td} \sim 0.008 & V_{ts} \sim 0.04 & V_{tb} \sim 1 \end{pmatrix}\begin{pmatrix} d \\ s \\ b \end{pmatrix} \tag{1.12}$$

Although historically it was originally proposed as an effective theory that a local $U(1)$ symmetry would explain, on the one hand, electromagnetic interactions (QED, for Quantum Electrodynamics), and on the other, a $SU(2)$ flavor symmetry was proposed to explain the weak interactions, certain unleashed points led to unifying these two theories in an overriding way. The fact that two of the three mediators of the weak interaction must have an electric charge by conservation of charge, implied that they must interact with photons as well as with the fermionic fields of matter. On the other hand, the predictions at that time indicated that if the mass of the mediators of the weak interaction was of the order of 100 GeV, the coupling constant associated with this interaction should be comparable to the electromagnetic one. Also, since neutrinos violate parity in nature, it was necessary to exclude right-handed neutrinos from the theory without excluding the right component of the other leptons (i.e. the electron, the muon, and the tauon). That is, a weak theory was needed only for left-handed neutrinos.

These issues led Weinberg, Glashow and Salam to propose the electroweak model, where both theories are unified under a symmetry $SU_L(2)\otimes U_Y(1)$, where the subfix L in $SU(2)$ refers to the fact that this symmetry only affects the left component of the matter fields (the doublets in (1.10) and (1.11)) , while the subfix Y in $U(1)$ refers to the introduction of a new quantum number, the hypercharge, which can have different values for each of the chirality projections of the fermionic fields

$$\psi_R \longrightarrow \psi'_R \equiv e^{i\beta(x)Y_R}\psi_R \tag{1.13}$$

$$\chi_L \longrightarrow \chi'_L \equiv e^{i[\alpha^a(x)T_a+\beta(x)Y_L]}\chi_L \tag{1.14}$$

Note that in (1.14) appear the three generators of the $SU(2)$ symmetry (the Pauli matrices multiplied by a factor of $1/2$). The hypercharge in each case can be calculated from the electric charge of the fermion (Q, in units where the electric charge of the electron is considered equal to 1) and its projection T_3 (only non-zero for the left projections of the fermions in the doublets)

$$Q = T_3 + \frac{Y_{L/R}}{2} \tag{1.15}$$

After changing the covariant derivatives and introducing the kinetic terms of the gauge bosons ($\mathscr{L}^{\text{kin}}$), the Lagrangian becomes [1, 2]

$$\begin{aligned}\mathscr{L} &= \overline{\chi_L}\gamma^\mu\left[i\partial_\mu - gT_aW^a_\mu - \frac{g_1}{2}Y_LB_\mu\right]\chi_L + \overline{\psi_R}\gamma^\mu\left[i\partial_\mu - \frac{g_1}{2}Y_RB_\mu\right]\psi_R - \frac{1}{4}W^a_{\mu\nu}W_a^{\mu\nu} - \frac{1}{4}B_{\mu\nu}B^{\mu\nu}\\ &= \mathscr{L}^{\text{int}} + \mathscr{L}^{\text{kin}}\end{aligned} \tag{1.16}$$

where $\mathscr{L}^{\text{int}}$ can be separated in the terms of interaction between fields and gauge bosons associated with each symmetry

$$\mathscr{L}^{\text{int}} = \mathscr{L}^{\text{int}}_{SU(2)_L} + \mathscr{L}^{\text{int}}_{U(1)_Y} \tag{1.17}$$

$$\mathscr{L}^{\text{int}}_{SU(2)_L} = -g\overline{\chi_L}\gamma^\mu T_a W^a_\mu \chi_L = -g J^a_\mu W^\mu_a \tag{1.18}$$

$$\mathscr{L}^{\text{int}}_{U(1)_Y} = -\frac{g_1}{2}\overline{\chi_L}\gamma^\mu Y_L B_\mu \chi_L - \frac{g_1}{2}\overline{\psi_R}\gamma^\mu Y_R B_\mu \psi_R = -g_1 J^Y_\mu B_\mu \tag{1.19}$$

If the case of the doublet involving the electron and its corresponding neutrino of (1.10), by (1.15) we get $Y^e_L = -1, Y^{\nu_e}_L = -1, Y^e_R = -2$, and the currents associated with neutral interactions are

$$J^Y_\mu = -\overline{e_R}\gamma_\mu e_R - \frac{1}{2}\overline{\nu_L}\gamma_\mu \nu_L - \frac{1}{2}\overline{e_L}\gamma_\mu e_L \tag{1.20}$$

$$J^3_\mu = \frac{1}{2}\overline{\nu_L}\gamma_\mu \nu_L - \frac{1}{2}\overline{e_L}\gamma_\mu e_L \tag{1.21}$$

In order to obtain the physical bosons associated with the neutral interactions, that is, the photon (A_μ) and the so-called Z boson (Z_μ), from the gauge bosons, the Weinberg angle (θ_W) is entered

$$\begin{pmatrix} A_\mu \\ Z_\mu \end{pmatrix} = \begin{pmatrix} \cos\theta_W & \sin\theta_W \\ -\sin\theta_W & \cos\theta_W \end{pmatrix} \begin{pmatrix} B_\mu \\ W^3_\mu \end{pmatrix} \tag{1.22}$$

where θ_W is uniquely defined as follows

$$\cos(\theta_W) = \frac{g}{\sqrt{g^2 + g_1^2}} \qquad \sin(\theta_W) = \frac{g_1}{\sqrt{g^2 + g_1^2}} \tag{1.23}$$

Inverting relation (1.22), one obtains

$$\begin{pmatrix} B_\mu \\ W^3_\mu \end{pmatrix} = \begin{pmatrix} \cos\theta_W & -\sin\theta_W \\ \sin\theta_W & \cos\theta_W \end{pmatrix} \begin{pmatrix} A_\mu \\ Z_\mu \end{pmatrix} \tag{1.24}$$

Defining further that

$$Q_e = g\sin(\theta_W) = g_1\cos(\theta_W) \tag{1.25}$$

where Q_e is the charge of the electron, our interactions can be obtained as a function of the physical bosons

$$\begin{aligned}\mathscr{L}^{\text{int},0} &= -g_1 J_\mu^Y B_\mu - g J_\mu^3 W_3^\mu = -(g\sin\theta_W J_\mu^3 + g_1\cos\theta_W J_\mu^Y)A^\mu - (g\cos\theta_W J_\mu^3 - g_1\sin\theta_W J_\mu^Y)Z^\mu \\ &= q_e\bar{e}\gamma_\mu e A^\mu - \left(\frac{\sqrt{g^2+g_1^2}}{2}\overline{\nu_L}\gamma_\mu\nu_L - \frac{g_1}{\sqrt{g^2+g_1^2}}\overline{e_R}\gamma_\mu e_R - \frac{(g_1^2-g^2)}{2\sqrt{g^2+g_1^2}}\overline{e_L}\gamma_\mu e_L\right)Z^\mu\end{aligned} \tag{1.26}$$

It should be noted from the result in (1.26) that the electromagnetic current is recovered for the photon (since this boson couples in the same way to the right and left components of the electron), while neutrinos do not effectively interact electromagnetically, since they have zero charges. On the other hand, in the neutral weak current, only the presence of left-handed neutrinos is observed, while it is verified for the electron that the coupling will depend on its chirality projection. On the other hand, continuing with the example of the electron and its corresponding neutrino, if $\mathscr{L}^{\text{int}}$ is intended to be completed, we must consider the weak charged currents, with their respective mediators, W^+ and W^-. Defining

$$W_\mu^\pm = \frac{1}{\sqrt{2}}(W_\mu^1 \mp W_\mu^2) \tag{1.27}$$

is obtained that

$$\mathscr{L}^{\text{int},+/-} = -\frac{g_1}{2}\left[\sqrt{2}\overline{\nu_L}\gamma^\mu e_L W_\mu^+ + \sqrt{2}\overline{e_L}\gamma^\mu\nu_L W_\mu^-\right] \tag{1.28}$$

1.3 Higgs Mechanism

Note that in the previous section, although it is experimentally known that W^+, W^- and Z bosons have masses of order $\mathcal{O}(10^2)$ GeV, there are no mass terms in the Lagrangian associated with them, since adding quadratic terms in the gauge fields would break the symmetry $SU_L(2)\otimes U_Y(1)$. The same justifies the absence of mass terms associated with fermions. To impose that there are massive elementary particles, a new scalar field, the Higgs field, and a potential associated with it, must be added to the Lagrangian. The corresponding boson is a particle without spin, without color charge, and without electric charge (therefore the Higgs does not interact with gluons and photons, preventing them to acquire mass). Formally, to maintain the gauge invariance $SU_L(2) \otimes U_Y(1)$, the following terms are added to the Lagrangian [4]

$$\mathscr{L} = (D_\mu \Phi)^\dagger (D^\mu \Phi) - V(\Phi) \tag{1.29}$$

where Φ is a doublet of complex scalar fields,

$$\Phi = \begin{pmatrix} \Phi^+ \\ \Phi^0 \end{pmatrix} = \frac{1}{\sqrt{2}} \begin{pmatrix} \Phi_1 + i\Phi_2 \\ \Phi_3 + i\Phi_4 \end{pmatrix} \tag{1.30}$$

D_μ is the covariant derivative, defined to have $SU_L(2) \otimes U_Y(1)$ invariance (with $Y = 1$ for Φ),

$$D_\mu = \partial_\mu - i\frac{g_1}{2} B_\mu - igT_a W_\mu^a \tag{1.31}$$

and $V(\Phi)$ is the scalar potential defined as

$$V(\Phi) = \mu^2 \Phi^\dagger \Phi + \lambda (\Phi^\dagger \Phi)^2 \tag{1.32}$$

In the case of $\mu^2 < 0$ and $\lambda > 0$, the potential has a minimum for a finite value of $|\Phi|$

$$\Phi^\dagger \Phi = \frac{1}{2}(\Phi_1^2 + \Phi_2^2 + \Phi_3^2 + \Phi_4^2) = \frac{-\mu^2}{2\lambda} \equiv \frac{v^2}{2} \tag{1.33}$$

where v is the so-called vacuum expectation value. This value allows us to define a minimum Φ_0 around which to develop the $\Phi(x)$ field

$$\Phi_0 = \frac{1}{\sqrt{2}} \begin{pmatrix} 0 \\ v \end{pmatrix} \tag{1.34}$$

Thus, in the mechanism known as spontaneous symmetry breaking (SSB), (1.30) can be rewritten as

$$\Phi(x) = e^{\frac{T_a \theta^a(x)}{v}} \frac{1}{\sqrt{2}} \begin{pmatrix} 0 \\ v + h(h) \end{pmatrix} \longrightarrow \Phi'(x) = \frac{1}{\sqrt{2}} \begin{pmatrix} 0 \\ v + h(h) \end{pmatrix} \tag{1.35}$$

where $h(x)$ is the Higgs field. It is observed in (1.35) that the $\theta^a(x)$ fields (non-massive Goldstone bosons) can be eliminated by doing a gauge transformation, taking advantage of the imposed $SU_L(2) \otimes U_Y(1)$ symmetry.

Finally, to visualize how the bosons of the weak interaction acquire mass, the relevant terms in (1.29) are taken and the transformation given in (1.35) is applied

$$\left| \frac{-ig_1}{2} B_\mu - ig\frac{\sigma_a}{2} W^a_\mu \begin{pmatrix} 0 \\ \frac{v}{\sqrt{2}} \end{pmatrix} \right|^2 = \left(\frac{1}{2} vg\right)^2 W^-_\mu W^{\mu +} + \frac{1}{2}\left(\frac{1}{2} v^2 \sqrt{g^2 + g_1^2}\right)^2 Z_\mu Z^\mu \tag{1.36}$$

from which can be obtained that

$$M_{W^{+/-}} = \frac{1}{2} vg \qquad\qquad M_Z = \frac{1}{2} v^2 \sqrt{g^2 + g_1^2} \tag{1.37}$$

To give mass to leptons, taking again the example of the electron and its respective neutrino in the doublets in (1.10), we must add the following term to the Lagrangian

$$\begin{aligned} \mathscr{L} &= -G_e \left(\overline{\nu_e} \;\; \overline{e}\right)_L \begin{pmatrix} \Phi^+ \\ \Phi^0 \end{pmatrix} e_R + h.c. \\ &= -\frac{G_e v}{2} \overline{e} e - \frac{G_e v}{2} h(x) \overline{e} e \end{aligned} \tag{1.38}$$

where G_e is determined in such a way that

$$\frac{G_e v}{2} \equiv m_e \tag{1.39}$$

with m_e equal to the electron mass. Note in (1.38) that only the electron acquires mass. To generate the mass of the quarks, the process is analogous, except for the fact that to generate the mass of the element of the doublet with up isospin projection, we must work with the conjugated Higgs field

$$\Phi_c = -i\sigma_2 \Phi * = \begin{pmatrix} -\overline{\Phi^0} \\ \Phi^- \end{pmatrix} \longrightarrow \Phi_c' = \frac{1}{\sqrt{2}} \begin{pmatrix} v + h(x) \\ 0 \end{pmatrix} \tag{1.40}$$

Then, taking the case of the u and d quarks

$$\mathscr{L} = -G_d \begin{pmatrix} \overline{u} & \overline{d} \end{pmatrix}_L \begin{pmatrix} \Phi^+ \\ \Phi^0 \end{pmatrix} d_R + h.c. - G_u \begin{pmatrix} \overline{u} & \overline{d} \end{pmatrix}_L \begin{pmatrix} -\overline{\Phi^0} \\ \Phi^- \end{pmatrix} u_R + h.c. \tag{1.41}$$

1.4 Why is the SM not a complete theory of Nature?

Since its formulation, the Standard Model has been extensively tested in high-energy experiments, such as those carried out at Tevatron, but the Large Hadron Collider [5](LHC) is undoubtedly the machine that has most explored its limits and extended its reach. Since its start-up, the greatest and most emblematic discovery made by the LHC was that of the Higgs boson [6, 7], which was one of the main aims of the LHC design and construction. But while the SM is a highly predictive model, and no disagreeing experiment has been reported, numerous questions remain unsolved, highlighting the experimental need to find New Physics (NP), as well as to develop theories Beyond the Standard Model (BSM), which to date are only a theoretical effort to try to find some answers. This is the main reason why the LHC has also pushed the frontiers of knowledge to extraordinary limits by allowing the SM to be validated as an effective theory up to the explored energies ($\sqrt{s} = 13$ TeV), as well as by excluding the existence of new particles over a broad range of masses and couplings in a wide variety NP models.

The state-of-the-art in High Energy Physics (HEP) research is a vast race of obstacles and challenges, between the current TeV energy frontier and the Planck energy scale, in which we are clueless about certain phenomena not explained by the SM. Without intending to make a full review, among these phenomena we can mention:

- Gravity: it is the only fundamental force that could not be included in the theory, and that relies on the problem that quantum mechanics and general relativity have not been able to come together in a fully coherent theory [8].

- Dark energy and Dark matter: their presence is implied in a variety of astrophysical observations [9], including gravitational effects that cannot be explained by accepted theories of gravity unless more matter is present than can be seen, and implies that SM only explains the 4% of the universe that corresponds to ordinary matter [10, 11].

- Neutrino oscillations: this experimentally observed phenomenon [12], which mixes neutrino flavor states with neutrino mass states (analogously to CKM mixing in (1.12)), requires neutrinos to have nonzero masses, a fact that is not contemplated in the SM, where they are assumed to be massless [13].

- The baryon asymmetry problem: there is observational evidence of matter-antimatter imbalance in the early universe, which leads to the remnant matter density we observe today, neither explained by the SM nor the General Relativity [14].

- The strong CP problem: no violation of the CP-symmetry has ever been seen in any experiment involving only the strong interaction, even though in the current QCD mathematical formulation a violation of CP-symmetry in strong interactions could occur [15].

Likewise, certain theoretical questions persist without explanation, which go beyond trying to solve why the model presents the symmetries that it has, why there are three, or if there will be more symmetries, such as the problem of hierarchies in the Higgs mass [4].

All these questions highlight the need to continue exploring our Universe, in search of New Physics. Accessing increasingly higher energies, and/or higher precision experiments, as well as the design of new observables, opens up a new scenario where new phenomena, not currently contemplated in the SM, could be revealed, which in turn would allow us to respond to any of the current questions and/or generate new ones. Moreover, considering that many theoretical forecasts have not been fulfilled so far, a phenomenological approach could be crucial to find new perspectives on persistent problems.

CHAPTER 2

A POSSIBLE WITNESS AND A USUAL SUSPECT WITHIN NEW PHYSICS: TOP QUARK AND *Z'*

Dentro del marco de búsqueda de Nueva Física (NF), en este capítulo describimos la importancia de la física del quark top en búsquedas indirectas como posible encubridor de nuevas partículas, presentando una serie de modelos simplificados que se utilizarán en esta tesis en el Capítulo 3. Por otro lado, describimos un candidato icónico dentro de las búsquedas directas, el bosón Z', presentando su fenomenología como mediador de partículas visibles (también ejemplificado en un modelo $B-L$), así como su fenomenología como mediador de materia oscura fermiónica. Ambos enfoques para el bosón Z' serán motivaciones del software presentado en el Capítulo 4 y el Capítulo 5, respectivamente.

Within the New Physics (NP) search framework, in this chapter we describe the importance of top quark physics in indirect searches as a possible cover-up for new particles, introducing a series of simplified models that will be used in this thesis in Chapter 3. On the other hand, we describe an iconic candidate within direct searches, the Z' boson, presenting its phenomenology as a mediator of visible particles (also exemplified in a $B-L$ model), as well as its phenomenology as a mediator of fermionic dark matter. Both Z' approaches will be motivations of the software presented in Chapter 4 and Chapter 5, respectively.

2.1 The scene: the direct and indirect search of New Physics

The Large Hadron Collider (LHC) has been successfully delivering proton-proton collision data at the unprecedented center of mass energy of 13 TeV. The formidable precision era enabled by the

LHC (and soon by the High-Luminosity LHC, which aims to a total of about 3000 fb^{-1} of data per experiment), has allowed the HEP community to probe like never before the SM predictions and look for cracks that might indicate the presence of NP processes, even if their masses are above the LHC reach [16]. The LHC, like other colliders, has searched for New Physics both through direct and indirect detection experiments and so far has extended the bounds on the NP scale.

Direct detection experiments rely on the reconstruction of the on-shell resonance mass of the sought particle from the momentum and energy of the final state particles after its decay. One of the simplest and most relevant processes that occur at hadron colliders is the Drell-Yan Process, such as the dielectron pair production through an intermediate Z boson ($Z \to e^+e^-$). In a Drell-Yan Process, the invariant mass of the decay products allows to directly measure the resonance mass, since it will have a peak in the mediator mass. Of course, in the case of having invisible/undetectable decay products (like neutrinos) in a given final state, there are other ways to directly detect a resonance (like the location of the so-called Jacobian peak from the transverse mass distribution in $W^+ \to e^+\nu$ events to get the W^+ resonance mass) [3]. In the search of NP, if the expected new resonance states are not too heavy and/or undetectable (like due to overwhelming backgrounds), it may also be possible to extract the corresponding resonance mass itself (without prior knowledge from the LHC).

On the other hand, in the case of being beyond the discovery reach, indirect detection experiments can probe effects of heavy or other undetectable new particles, complementary to direct searches. In hadron colliders such as the LHC, this type of measurement comes from the development of precision measurements, since they often aim to observe quantum effects of NP, such as loop contributions. Indirect searches sometimes are related to the measurement of rare processes, where NP contributions do not compete with large SM lowest-order predictions. Of course, this kind of experiment can indirectly probe for a given NP resonance by exploring deviations from the cross-sections and asymmetries predicted by the SM in one or various final state channels, modeling NP contributions with contact interaction-like operators and/or simplified models.

Direct and indirect searches at the LHC for BSM phenomena will continue to cover previously unexplored ground, with the experimental collaborations pursuing both model-guided and model-independent searches to make sure all options are covered [17]. In this context, on one side, in Section 2.2 we introduce one of the favorites witnesses of possible deviations from the SM predictions in indirect searches, the top quark (t). On the other hand, on the direct searches front, we present in Section 2.4 the Z' boson, one of the cleanest signals for NP that may be discovered early on and a resonance structure with a wide variety of possible identities, predicted to exist in a large number of extensions to the Standard Model (SM). Both particles are separately key ingredients in the phenomenological proposals presented along with this thesis.

2.2 The importance of top quark in the uncover of New Physics

With the largest mass of all quarks, the top quark (t) is the heaviest particle of the Standard Model, and the heaviest elementary particle ever found [18]. In proton-proton colliders, most tops are produced in $t\bar{t}$ pairs, with a minority contribution from single top production from a Wtb vertex. Its mass makes it the only quark capable of decaying semi-weakly, into a real W boson and a bottom quark (b) [19]. That determines its short lifetime, and the fact that decays before hadronization allows preserving some of its properties (like its polarization [20, 21]), directly transferred in the decaying to the kinematic distributions of its subsequent particles, given a unique opportunity for exploring its nature.

The large mass of the top quark makes it a prime candidate to help uncover the dynamics behind NP at the electroweak scale. Several BSM models predict the existence of new particles coupled to the top. This is usually because of the same reason it has a large coupling to the Higgs boson: its large mass provides a large Yukawa coupling, and that not only makes the top quark the perfect mediator to the Higgs sector but also suggest the idea of hidden particles with large coupling to the heaviest SM quark [22–24]. In many NP models, the top quark plays a prominent role, often participating in new interactions related to electroweak symmetry breaking, or preferentially coupling to new degrees of freedom. Far from pretending to make a full review, between those scenarios we can mention supersymmetry[25–28], top-compositeness [29], two-Higgs doublet models [30], and models with extra dimensions [31, 32].

Top quark properties are predicted by the SM and can be modified by NP effects at the production or decay level. Therefore, precision measurements can uncover deviations of SM predictions which could serve as indirect evidence of BSM processes due to particles with masses not currently accessible at the LHC [17]. Possible new phenomena may enhance the SM cross-sections predictions through the production of new particles in association with a heavy top quark. The measurement of these magnitudes within the program of hadron colliders such as the LHC constitutes one of the principal indirect ways to constraint or discard BSM models.

The enhanced or modified coupling to top quark predicted from these kinds of models is also particularly relevant for not yet observed processes with small cross-sections, such as the four-top production ($t\bar{t}t\bar{t}$). In such cases, reinterpretation of an upper limit on SM cross-section has the potential to constrain BSM theories. Moreover, for direct searches of these BSM signatures, the SM production of unobserved processes like $t\bar{t}t\bar{t}$ can be a background. With the larger center-of-mass energy and luminosity of the LHC, the study of more rare processes becomes possible, in which top quark becomes the main gateway to the discovery of possible extensions of the SM.

2.3 Simplified NP models with coupling to top quark

One way to face a phenomenological analysis of the impact generated by a hypothetical new particle (X) in a given final state at the LHC is through the well-known use of simplified models. The main goal of these kinds of models is to present the basic features of a given NP scenario without the theoretical difficulties of a complete theory.

Given the absence of clear NP signals in the analysis of LHC data, and focusing on the case where the new particle couples only to the SM top quark, we can consider a simple NP model containing either a spin-0, spin-1 or spin-2 new particle. The free parameters in such simplified proposals are the coupling of the new particle to the top quark (g_{Xt}) and its resonance mass (M). We present in the following four example models with the new particle being a scalar, a pseudo-scalar, a vector Z', or a graviton. Depending on the magnitude of the parameters in the model, this kind of NP would become visible in different final states containing at least a top quark. In particular, the relative sensitivity of these final states to the NP will change drastically depending on if the new particle mass is heavier or lighter than $2m_t$. The latter is one of the main drivers beyond Chapter 3, where a full phenomenological study is presented showing the impact of these models in four-top production at the LHC (assuming $M < 2m_t$).

The idea along with this section is to briefly expose the type of effective Lagrangian corresponding to each type of leptophilic signature, making no assumptions in the underlying model. It is not our scope to develop the UV completion of the aforementioned NP scenarios. However, it can be argued that having a new resonance with couplings to SM particles dominated by the top quark is feasible, for instance in two-sector models [33] or Composite Higgs Models (CHM) [34]. In these models the SM is accompanied by a heavier strongly interacting sector; the details and phenomenology of this kind of NP can be found elsewhere [33]. In CHM models, to avoid experimental constraints and to explain the fermion mass hierarchy, it is customary to implement partial compositeness, where the degree of compositeness of each physical fermion depends on its mass [35]. Given Electroweak Precision Tests on $SU(2)_L$ it is convenient to set in the model the right-chiral top quark (t_R) with large compositeness [33]. Then, depending on the particular realization of each model, one can obtain for different cases some new light resonances that couple predominantly to t_R. For the case of a spin-0 field, however, the Lorentz structure requires a left-chiral top quark (t_L) as well. Vertices of this kind are found in Ref.[36], and Ref. [37] discusses a UV complete model with additional scalars that present this kind of phenomenology.

In the following, α_s is the strong coupling constant ($\alpha_s = 0.1176$ [10]), α is the fine-structure constant (we take $\alpha = 1/128$ at $Q^2 = m^2(W)$ [10], to be closer to the energy scale of the NP resonances considered) and m_t is the top quark mass (we simply assume $m_t = 173$ GeV). Details on decay widths are described in Appendix A.

2.3.1 Scalar NP: ϕ

The simplest example of a spin-0 model is to have a scalar new particle (ϕ). Assuming that it only couples to top quarks, we have the following simplified Lagrangian

$$\mathcal{L}_{\phi}^{\text{tree}} = g_{\phi t}\, \bar{t}_L \phi t_R + h.c. \tag{2.1}$$

A one-loop effective coupling to gluons (ϕgg) and to photons ($\phi\gamma\gamma$) must be added to the Lagrangian through a top-quark loop [38, 39]

$$\mathscr{L}^{\text{eff}}_{\phi gg} = \frac{\alpha_s}{12\pi}\frac{g_{\phi t}}{m_t}F(z_t)G^a_{\mu\nu}G^{\mu\nu}_a\phi \tag{2.2}$$

$$\mathscr{L}^{\text{eff}}_{\phi\gamma\gamma} = \frac{2\alpha}{9\pi}\frac{g_{\phi t}}{m_t}F_{\mu\nu}F^{\mu\nu}\phi \tag{2.3}$$

with loop function for gluons defined as

$$F(z_t) = \frac{3}{2}z_t\left[1+(1-z_t)\arcsin^2\left(\sqrt{1/z_t}\right)\right] \tag{2.4}$$

and

$$z_t = (2m_t/M_\phi)^2 \tag{2.5}$$

The NP effective interaction Lagrangian therefore reads

$$\mathscr{L}_\phi = \mathscr{L}^{\text{tree}}_\phi + \mathscr{L}^{\text{eff}}_{\phi gg} + \mathscr{L}^{\text{eff}}_{\phi\gamma\gamma} \tag{2.6}$$

2.3.2 Pseudo-scalar NP: A

The pseudo-scalar case (A), also an example of a spin-0 new particle, has the following Lagrangian

$$\mathscr{L}^{\text{tree}}_A = g_{At}\,\bar{t}_L A i\gamma^5 t_R + h.c. \tag{2.7}$$

Including the following one-loop effective Lagrangian describing Agg and $A\gamma\gamma$ interactions [38, 39]

$$\mathscr{L}^{\text{eff}}_{Agg} = \frac{\alpha_s}{4\pi}\frac{g_{At}}{m_t}H(z_t)G^a_{\mu\nu}\tilde{G}^{\mu\nu}_a A \tag{2.8}$$

$$\mathscr{L}^{\text{eff}}_{A\gamma\gamma} = \frac{\alpha}{3\pi}\frac{g_{At}}{m_t}F_{\mu\nu}\tilde{F}^{\mu\nu}A \tag{2.9}$$

with

$$H(z_t) \; = \; z_t \arcsin^2\left(\sqrt{1/z_t}\right) \tag{2.10}$$

and

$$z_t \; = \; (2m_t/M_A)^2 \tag{2.11}$$

the full pseudo-scalar Lagrangian reads

$$\mathscr{L}_A = \mathscr{L}_A^{\text{tree}} + \mathscr{L}_{Agg}^{\text{eff}} + \mathscr{L}_{A\gamma\gamma}^{\text{eff}} \tag{2.12}$$

2.3.3 Vector NP: Z'

We show the case of a vector spin-1, color singlet, and electrically-neutral Z' which couples exclusively to t. To keep the vector coupling to the top quark as a free parameter independently of the SM electroweak gauge group, we keep only couplings to right-handed tops. This also helps to avoid conflicts with LEP precision measurements. Then, this type of interaction reads as

$$\mathscr{L}_{Z'} = g_{Z't}\, Z'_\mu \bar{t}_R \gamma^\mu t_R \tag{2.13}$$

Since Z' is a spin-1 particle, it cannot couple at any order to a $\gamma\gamma$ final state due to the Landau–Yang theorem [40–42]. However, recent works claim that a spin-1 particle can couple to a gg state since gluons are colored [43–46]. This possibility can be ignored in the case where we expect that limits coming from resonance searches in di-jet (jj) production and $t\bar{t}$+jets production (tjj or $t\bar{t}jj$) do not have sufficient sensitivity to probe the relevant parameter space for the models considered (indeed, this is the case in Chapter 3)

2.3.4 Graviton NP: G

We consider an effective Lagrangian for a spin-2 graviton with field $\hat{G}_{\mu\nu}$. The tree-level interaction Lagrangian reads [47]

$$\mathscr{L}_G^{\text{tree}} = -\frac{i}{2\Lambda}\hat{G}^{\mu\nu}\left[g_{Gt}\left(\bar{t}_R\gamma_\mu \overleftrightarrow{D}_\nu t_R - \eta_{\mu\nu}\bar{t}_R\gamma^\rho \overleftrightarrow{D}_\rho t_R\right)\right] \tag{2.14}$$

where

$$\bar{f}\gamma_\mu \overleftrightarrow{D}_\nu f = \bar{f}\gamma_\mu D_\nu f - D_\nu \bar{f}\gamma_\mu f \tag{2.15}$$

Contrary to the previous NP models, the spin-2 Lagrangian needs dimensional couplings, hence the dimensional constant Λ in the denominator. The constant Λ can be understood as the energy scale up to which the theory as described here is valid. Throughout Chapter 3, we set $\Lambda = 3$ TeV.

In this scenario, we also have to take into account the one-loop effective Lagrangians due to gluons and photons [47, 48]

$$\mathcal{L}^{\rm eff}_{Ggg} = -\frac{\alpha_s}{12\pi\Lambda} g_{Gt} A_G(z_t,\mu_0)\hat{G}_{\mu\nu}\left(\frac{\eta^{\mu\nu}}{4} G^{\rho\sigma}_a G^a_{\rho\sigma} - G^{\mu\rho}_a G^{a\nu}_\rho\right) \tag{2.16}$$

$$\mathcal{L}^{\rm eff}_{G\gamma\gamma} = -\frac{2\alpha}{9\pi\Lambda} g_{Gt} A_G(z_t,\mu_0)\hat{G}_{\mu\nu}\left(\frac{\eta^{\mu\nu}}{4} F^{\rho\sigma} F_{\rho\sigma} - F^{\mu\rho} F^\nu_\rho\right) \tag{2.17}$$

where the loop function in this case is used for both loops and is define as

$$\begin{aligned} A_G(z_t,\mu_0) = & -\frac{1}{12}\Bigg\{\frac{9}{4} z_t (z_t+2)\left[2\tan^{-1}\left(\sqrt{z_t-1}\right)-\pi\right]^2 \\ & -3(5z_t+4)\sqrt{z_t-1}\left[2\tan^{-1}\left(\sqrt{z_t-1}\right)-\pi\right] - 39z_t - 35 - 12\ln\frac{\mu_0^2}{m_t^2}\Bigg\} \end{aligned} \tag{2.18}$$

with

$$z_t = (2m_t/M_G)^2 \tag{2.19}$$

Here μ_0 is the renormalization scale which we set it to $\mu_0 = M_G$ [47] in Chapter 3. Therefore, the full spin-2 Lagrangian reads

$$\mathcal{L}_G = \mathcal{L}^{\rm tree}_G + \mathcal{L}^{\rm eff}_{Ggg} + \mathcal{L}^{\rm eff}_{G\gamma\gamma} \tag{2.20}$$

2.4 The importance of *Z'* as a presumed guilty of New Physics

One of the aims of the physics program at the LHC is to search for new phenomena that become visible in high-energy proton-proton collisions. A possible signature of such phenomena would be the production of a heavy resonance with its subsequent decay into a final state consisting of a pair of fermions or vector bosons. A massive, color singlet, electrically neutral spin-1 particle, also known as Z' (because of the similarity in quantum numbers to the SM Z boson) is predicted in a variety of models that attempt to extend the SM and has been the object of extensive phenomenological studies [49, 50].

Typical models predicting the existence of a heavy neutral Z' extended the gauge group of the SM with an extra $U'(1)$ gauge group. In particular, one (or more) additional $U'(1)$ gauge group provides one of the simplest extensions of the SM. In other cases, Z' bosons may also arise from larger gauge groups. The new symmetries, or a linear combination of them, can be broken near the TeV scale, giving rise to new massives Z-like bosons denoted as Z'. In most cases, a $SU_c(3) \otimes SU_L(2) \otimes U_Y(1) \otimes U'(1)$ can be assumed as the underlying effective gauge group at low energies, mainly motivated by the hope that there is an extra neutral gauge boson that is light enough to give the first signal in upcoming experiments.

Representatively, and very far from being exhaustive, between the many BSM proposals with an additional Z' boson we can mention Grand Unified Theories (GUT) based on the E_6 gauge group [51, 52], left-right models [53–56], composite models [33, 57, 58], Superstring Theories [59, 60], and $B-L$ models, where the name refers to the baryon number minus lepton number (this type of models are further introduced in Section 2.6, we a $B-L$ model example is explained in detail).

2.5 The usual witnesses: Z' with couplings to all SM fermions

Beyond the model that motivates the appearance of a new boson Z', if it provides couplings with the quarks and leptons of the Standard Model, it can always be reduced to an effective model with a Lagrangian where the phenomenology is subject to the mass of Z' and two effective coupling constants per fermion. Thus, the most general expression for the interaction term of a Z' coupling to all SM fermions can be expressed as

$$\mathscr{L} \supset Z'_\mu \sum_f \left(g_{f_L} \bar{f}_L \gamma^\mu f_L + g_{f_R} \bar{f}_R \gamma^\mu f_R \right) \tag{2.21}$$

where $g_{f_{L/R}}$ is the effective coupling between Z' and a given left/right-handed fermion (f_L/f_R). The couplings to quarks and leptons are real dimensionless parameters, and are not necessarily generation-dependent (in that case, (2.21) may be written with generation indices $i, j \in \{1,2,3\}$ labeling the quark and lepton fields, and the number of free parameters is reduced).

The aforementioned couplings describing Z' interaction with fermions are subject to some theoretical constraints. BSM proposals including a heavy spin-1 boson are well behaved at high energies only if the Z' is a gauge boson associated with spontaneous symmetry breaking, and to preserve the gauge symmetry, couplings must satisfy anomaly cancellation conditions. Also, fermions must get masses from gauge-invariant interaction with boson-Higgs-like fields, and that constraint their charges under the new gauge symmetry [10].

In the presence of the interactions shown in (2.21), a Z' resonance would be produced in s-channel at hadron colliders such as the LHC through quark-antiquark annihilation. Therefore its production cross-section would depend on its coupling to valence and sea quarks (u, d, c, s, b), which depend on the signal point in the NP parameter space. After production, the Z' boson would decay into pair of fermions. The decay width into a pair of lepton is defined as [10]

$$\Gamma(Z' \to \ell^- \ell^+) \simeq \frac{M_{Z'}}{24\pi}\left[\left(g_{\ell_L}\right)^2 + \left(g_{\ell_L}\right)^2\right] \tag{2.22}$$

where QED corrections are not included. The decay widths into a pair of light quarks without including QCD corrections is similar, but with an additional color factor of 3 [10]

$$\Gamma(Z' \to q\bar{q}) \simeq \frac{3M_{Z'}}{24\pi}\left[\left(g_{q_L}\right)^2 + \left(g_{q_R}\right)^2\right] \tag{2.23}$$

For the decay width into a top-quark pair, we can include the correction coming from the heavy quark mass

$$\Gamma(Z' \to t\bar{t}) \simeq \frac{3M_{Z'}}{48\pi}\sqrt{1-4\left(\frac{m_t}{M_{Z'}}\right)^2}\left\{\left(g_{t_R}-g_{t_L}\right)^2\left[1-4\left(\frac{m_t}{M_{Z'}}\right)^2\right]+\left(g_{t_R}+g_{t_L}\right)^2\left[1+2\left(\frac{m_t}{M_{Z'}}\right)^2\right]\right\} \tag{2.24}$$

Branching ratios also depend on the aforementioned couplings, but also on the Z' couplings to all other SM. Other decays channels such as W^+W^- and Zh could have large widths and must be computed in the estimation of the total width.

2.6 *Z'* model example: a *B-L* model

One way to add a minimal $U'(1)$ extension of the SM is associated with the $B-L$ number. This kind of extension is attractive because of its relatively simple theoretical structure and plays an important role in many BSM scenarios associated with the well-known see-saw mechanism [56, 61], which crucial test is the detection of a predicted Z' heavy resonance.

Considering a $SU(2)_L \times U(1)_Y \times U(1)_{B-L}$ symmetry (and ignoring the SM color symmetry $SU(3)_c$ for the sake of simplicity), the gauge sector Lagrangian is defined as [62–64]

$$\mathscr{L}_g = -\frac{1}{4}B_{\mu\nu}B^{\mu\nu} - \frac{1}{4}W^a_{\mu\nu}W^{a\mu\nu} - \frac{1}{4}Z'_{\mu\nu}Z'^{\mu\nu} \tag{2.25}$$

where $W^a_{\mu\nu}$, $B_{\mu\nu}$ and $Z'_{\mu\nu}$ are the field strength tensors for $SU(2)_L$, $U(1)_Y$ and $U(1)_{B-L}$.

In this type of models, $Z-Z'$ mixing occurs through the conventional spontaneous symmetry breaking (SSB) mechanism, because the usual Higgs doublet is not singlet under the new $U(1)_{B-L}$ [65]. The scalar sector is defined as

$$\mathscr{L}_s = (D^\mu\Phi)^\dagger(D_\mu\Phi) + (D_\mu\chi)^\dagger(D_\mu\chi) - V(\Phi,\chi) \tag{2.26}$$

with the potential defined as [64, 66]

$$V(\Phi,\chi) = m^2(\Phi^\dagger\Phi) + \mu^2|\chi|^2 + \lambda_1(\Phi^\dagger\Phi)^2 + \lambda_2|\chi|^4 + \lambda_3(\Phi^\dagger\Phi)|\chi|^2 \tag{2.27}$$

where Φ is the aforementioned scalar doublet, and χ is a complex singlet scalar field required to achieved the breaking of the new gauge group to acquire a *vev* at the TeV scale. The covariant derivatives are [62, 66]

$$D^\mu\Phi = \partial_\mu\Phi + i\left[\frac{g}{2}T^a W^a_\mu + g_1 Y B_\mu + g_1' Y' B_\mu'\right]\Phi \tag{2.28}$$

$$D^\mu\chi = \partial_\mu\chi + i g_1' Y' B_\mu'\chi \tag{2.29}$$

where g_1' is the coupling from $U(1)_{B-L}$, and g and g_1 are the couplings coming from de SM electroweak interactions and can be defined as usual from Eq. (1.25)

$$g = \frac{Q_e}{\sin(\theta_W)} \tag{2.30}$$

$$g_1 = \frac{Q_e}{\cos(\theta_W)} \tag{2.31}$$

After SSB, the scalar fields can be written as

$$\Phi = \begin{pmatrix} 0 \\ \frac{v+\phi^0}{\sqrt{2}} \end{pmatrix}, \qquad \chi = \frac{v' + \phi'^0}{\sqrt{2}} \tag{2.32}$$

where the two *vev*'s, v and v', are real and positive. From the minimization of Eq. (2.27) one obtains the mass matrix for ϕ^0 and ϕ'^0, and after its diagonalization the mass eigenstates h and H are obtained

$$\begin{pmatrix} h \\ H \end{pmatrix} = \begin{pmatrix} \cos(\alpha) & -\sin(\alpha) \\ \sin(\alpha) & \cos(\alpha) \end{pmatrix} \begin{pmatrix} \phi^0 \\ \phi'^0 \end{pmatrix} \tag{2.33}$$

Here α is the mixing angle and h is the SM-like Higgs boson.

To determine the gauge boson spectrum, we have to diagonalize the scalar kinetic terms in (2.26) as for the SM. We must expect within the gauge eigenstates a massless boson, the photon, and four other massive bosons. According to (2.28), the charged electroweak bosons $W^{\pm}$ will have masses given by their SM expressions, being only related to the $SU(2)_L$ factor. The other gauge boson masses are not that simple to identify, because of mixing. For the first term in (2.26) we have

$$\begin{aligned}(D^{\mu}\Phi)^{\dagger}(D_{\mu}\Phi) &= \frac{1}{2}[\partial_{\mu}(v+\phi^0)]^2 + \frac{1}{2}\frac{g^2}{4}(v+\phi^0)^2(W^{1\mu}W^1_{\mu} + W^{2\mu}W^2_{\mu}) + \frac{1}{2}(v+\phi^0)^2 \\ &\times \left[\begin{pmatrix} B^{\mu} & W^{3\mu} & B'^{\mu} \end{pmatrix} \begin{pmatrix} g_1 Y^2 & -\frac{g g_1 Y}{2} & g g_1' Y Y' \\ -\frac{g g_1 Y}{2} & \frac{g^2}{4} & -\frac{g g_1' Y'}{2} \\ g g_1' Y Y' & -\frac{g g_1' Y'}{2} & g_1' Y'^2 \end{pmatrix} \begin{pmatrix} B_{\mu} \\ W^3_{\mu} \\ B'_{\mu} \end{pmatrix} \right]\end{aligned} \tag{2.34}$$

while for the second term we have

$$(D_{\mu}\chi)^{\dagger}(D_{\mu}\chi) = \frac{1}{2}[(\partial_{\mu}(v'+\phi'^0)]^2 + \frac{1}{2}(v'+\phi'^0)^2 g_1'^2 Y_{\chi}^2 B'^{\mu}B'_{\mu} \tag{2.35}$$

Replacing the values of the couplings with the expressions in (2.30) and (2.31), and taking $Y = Y' = 1/2$ and $Y_{\chi} = 2$ to guarantee gauge invariance, the explicit expression for the mass matrix turns out

$$M^2 = \frac{1}{2}\frac{1}{4}v^2(g^2+g_1^2) \begin{pmatrix} \sin^2(\theta_W) & -\sin(\theta_W)\cos(\theta_W) & \frac{g_1'\sin(\theta_W)}{\sqrt{g^2+g_1^2}} \\ -\sin(\theta_W)\cos(\theta_W) & \cos^2(\theta_W) & \frac{-2g_1'\cos(\theta_W)}{\sqrt{g^2+g_1^2}} \\ \frac{g_1'\sin(\theta_W)}{\sqrt{g^2+g_1^2}} & \frac{-2g_1'\cos(\theta_W)}{\sqrt{g^2+g_1^2}} & \frac{g_1'(1+16r^2)}{g^2+g_1^2} \end{pmatrix} \tag{2.36}$$

with $r = v'/v$. After diagonalization of (2.36), in analogy with the SM, the mass eigenstates will be linear combinations of W^3_{μ}, B_{μ}, and B'_{μ} [63]

$$\begin{pmatrix} B_{\mu} \\ W^3_{\mu} \\ B'_{\mu} \end{pmatrix} = \begin{pmatrix} \cos(\theta_W) & -\sin(\theta_W)\cos(\theta_{B-L}) & \sin(\theta_W)\sin(\theta_{B-L}) \\ \sin(\theta_W) & \cos(\theta_W)\cos(\theta_{B-L}) & -\cos(\theta_W)\sin(\theta_{B-L}) \\ 0 & \sin(\theta_{B-L}) & \cos(\theta_{B-L}) \end{pmatrix} \begin{pmatrix} A_{\mu} \\ Z_{\mu} \\ Z'_{\mu} \end{pmatrix} \tag{2.37}$$

where θ_{B-L} is the Z-Z' mixing angle, defined as

$$\tan(2\theta_{B-L}) = \frac{2g_1'\sqrt{g^2+g_1^2}}{\left[g_1'^2(1+16r^2)-g^2-g_1^2\right]} \tag{2.38}$$

The Z-Z' mixing angle is bounded by LEP searches, and the current bound on this parameter is $|\theta_{B-L}| \leq 10^{-3}$ [67]. Electro-Weak Precision Tests from LEP-II also place limits in the model, and set the 99% CL allowed region [68]

$$\frac{M_{Z'}}{g_1} \geq 7.1 \text{ TeV} \tag{2.39}$$

For the masses we obtain

$$M_A^2 = 0 \tag{2.40}$$

$$M_Z^2 = \frac{1}{4}v^2(g^2+g_1^2)\left[\cos^2(\theta_{B-L}) - \frac{2g_1'\cos(\theta_{B-L})\sin(\theta_{B-L})}{\sqrt{g^2+g_1^2}} + \frac{g_1'^2(1+16r^2)\sin^2(\theta_{B-L})}{g^2+g_1^2}\right] \tag{2.41}$$

$$M_{Z'}^2 = \frac{1}{4}v^2(g^2+g_1^2)\left[\sin^2(\theta_{B-L}) + +g_1'\cos(\theta_{B-L})\left(\frac{g_1'(1+16r^2)\cos(\theta_{B-L})}{g^2+g_1^2} + \frac{2\sin(\theta_{B-L})}{\sqrt{g^2+g_1^2}}\right)\right] \tag{2.42}$$

In the limit where $g_1' = 0$ and $\theta = 0$, we recover the usual expression for the Z boson mass within the SM

$$M_Z = \frac{1}{2}v\sqrt{g^2+g_1^2} \tag{2.43}$$

The interactions vertices between the neutral gauge bosons Z, Z' and a pair of SM fermions are given by [62]

$$\mathscr{L}_{\text{NC}} = -\frac{ig}{\cos(\theta_W)}\sum_f \bar{f}\gamma^\mu \frac{1}{2}(g_v^f - g_a^f\gamma^5)fZ_\mu - \frac{ig}{\cos(\theta_W)}\sum_f \bar{f}\gamma^\mu \frac{1}{2}(g_v^{\prime f} - g_a^{\prime f}\gamma^5)fZ_\mu' \tag{2.44}$$

where the new couplings are

$$
\begin{aligned}
g_v^f &= T_3^f \cos(\theta_{B-L}) - 2Q_f \sin^2(\theta_W)\cos(\theta_{B-L}) + 2Y'\frac{g_1'}{g}\cos(\theta_W)\sin(\theta_{B-L}) \\
g_a^f &= T_3^f \cos(\theta_{B-L}) \qquad (2.45) \\
g_v^{\prime f} &= -T_3^f \sin(\theta_{B-L}) + 2Q_f \sin^2(\theta_W)\sin(\theta_{B-L}) + 2Y'\frac{g_1'}{g}\cos(\theta_W)\cos(\theta_{B-L}) \\
g_a^{\prime f} &= -T_3^f \sin(\theta_{B-L}) \qquad (2.46)
\end{aligned}
$$

The charges are the usual SM and $B-L$ ones (that is, $Y' = 1/3$ for quarks and $Y' = -1$ for leptons with no distinction between generations, ensuring universality). In the limit where $g_1' = 0$ and $\theta_{B-L} = 0$, the couplings of the Z boson to all SM fermions are recovered

$$
\begin{aligned}
g_v^f &= T_3^f - 2Q_f \sin^2(\theta_W) \\
g_a^f &= T_3^f \qquad (2.47)
\end{aligned}
$$

The decay widths of the new Z' boson includes the decay to a fermion pair, but also to W^+W^- [50, 69] and to Zh[69, 70]

$$
\begin{aligned}
\Gamma(Z' \to W^+W^-) &= \frac{g^2}{192\pi}\cos^2(\theta_W)\sin(\theta_{B-L})M_{Z'}\left(\frac{M_{Z'}}{M_Z}\right)^4\left(1-4\frac{M_W^2}{M_{Z'}^2}\right)^{3/2} \\
&\times \left[1+20\frac{M_W^2}{M_{Z'}^2}+12\frac{M_W^4}{M_{Z'}^4}\right] \qquad (2.48)
\end{aligned}
$$

$$
\begin{aligned}
\Gamma(Z' \to Zh) &= \frac{g^2 M_Z^2}{192\pi M_W^2}M_{Z'}\sqrt{\lambda}\left(\lambda+12\frac{M_Z^2}{M_{Z'}^2}\right) \\
&\times \left[\left(\frac{4M_Z^2}{v^2}-g_1'^2\right)\sin(2\theta_{B-L})+\left(\frac{4M_Z g_1'}{v}\right)\cos(2\theta_{B-L})\right] \qquad (2.49)
\end{aligned}
$$

where λ is a function defined as

$$\lambda\left(1,\frac{M_Z^2}{M_{Z'}^2},\frac{M_h^2}{M_{Z'}^2}\right)=1+\left(\frac{M_Z^2}{M_{Z'}^2}\right)^2+\left(\frac{M_h^2}{M_{Z'}^2}\right)^2-2\left(\frac{M_Z^2}{M_{Z'}^2}\right)-2\left(\frac{M_h^2}{M_{Z'}^2}\right)-2\left(\frac{M_Z^2}{M_{Z'}^2}\right)\left(\frac{M_h^2}{M_{Z'}^2}\right) \tag{2.50}$$

2.7 An invisible accomplice: *Z'* with coupling to Dirac Dark Matter

Attempts at finding NP usually center around the production of hypothetical particles, which subsequently decay to observable SM particles. This is the main idea behind most available exotic searches performed in experiments such as the LHC, like Z' searches. However, some scenarios are hidden from such searches, because the BSM particles do not necessarily decay into detectable species. Scenarios with new particles that are not directly observable in collider detectors are motivated by many BSM theories.

One of the strongest motivations comes from the idea of particle dark matter (DM). Over the last decades, cosmological evidence for the existence of DM has been uninterruptedly accumulating [71], yet with very few hints as to its nature or detailed properties. The abundance of DM in the universe, as well as many of the observed phenomena commonly attached to DM, can be explained just by attributing to DM particles the right masses and couplings. One theoretically attractive model is that of a thermally produced weakly interacting massive particle (WIMP) [72], one of the leading non-baryonic cold-dark-matter candidates.

Given that so little is known about the properties of DM the most informative framework for studying DM properties in a simplified framework is as model-independent as possible [73]. Within the scenarios considering WIMPs, there is a simplified model of fermionic DM production via bosonic mediators with spin one [74, 75]. In a framework as comprehensive as possible, this model should be considered when compiling possible search channels for a Z' boson.

In this model, a SM singlet Dirac fermion (χ) is produced for s-channel spin-1 axial-vector or vector mediator (Z'_A or Z'_V). This fermion is the DM candidate, rendered stable by a discrete $\mathbf{Z}_2$ symmetry, as customary in DM models. The most simplified version of this model requires to set the Z' and DM masses ($M_{Z'}$ and m_χ), the coupling of Z' to all quarks (g_{q_V}/g_{q_A}, equal for the three generations of quarks) and the coupling of Z' to DM (g_{χ_V}/g_{χ_A}).

$$\mathscr{L} \supset -Z'_{V\mu}\left(\sum_q g_{q_V}\bar{q}\gamma^\mu q - g_{\chi_V}\bar{\chi}\gamma^\mu\chi\right) \tag{2.51}$$

$$\mathscr{L} \supset -Z'_{A\mu}\left(\sum_q g_{q_A}\bar{q}\gamma^\mu\gamma^5 q - g_{\chi_A}\bar{\chi}\gamma^\mu\gamma^5\chi\right) \tag{2.52}$$

The total width of the mediator ($\Gamma_{Z'}$), from the four free parameters in the simplified model, assuming that no additional visible or invisible decays contribute to $\Gamma_{Z'}$, is defined in each case as [74, 75]

$$\begin{aligned}\Gamma_{Z'_V} &= \frac{g^2_{\chi_V} M_{Z'_V}}{12\pi}\left(1+\frac{2m^2_\chi}{M^2_{Z'_V}}\right)\beta_\chi \Theta(M_{Z'_V}-2m_\chi) \\ &+ \sum_q \frac{3g^2_{q_V} M_{Z'_V}}{12\pi}\left(1+\frac{2m^2_q}{M^2_{Z'_V}}\right)\beta_q \Theta(M_{Z'_V}-2m_q)\end{aligned} \tag{2.53}$$

$$\begin{aligned}\Gamma_{Z'_A} &= \frac{g^2_{\chi_A} M_{Z'_A}}{12\pi}\beta^3_\chi \Theta(M_{Z'_A}-2m_\chi) \\ &+ \sum_q \frac{3g^2_{q_A} M_{Z'_A}}{12\pi}\beta^3_q \Theta(M_{Z'_A}-2m_q)\end{aligned} \tag{2.54}$$

where $\Theta(x)$ is the Heaviside step function and β_f is the velocity of the fermion f in the mediator rest frame, defined as

$$\beta_f = \sqrt{1-\frac{4m^2_f}{M^2_{Z'}}} \tag{2.55}$$

It is worth mention that in a more general approach g_{q_V}/g_{q_A} could be different for each quark, and also should be considered couplings between Z' and leptons, usually not considered in the context of DM. In that case, the first term in (2.51) and (2.52) should include all SM fermions instead of only quarks, and becomes equivalent (unless a global constant) to expression in (2.21), since

$$\mathscr{L} \supset Z'_\mu \left[\sum_f \left(g_{f_L}\bar{f}_L\gamma^\mu f_L + g_{f_R}\bar{f}_R\gamma^\mu f_R\right) + g_{\chi_L}\bar{\chi}_L\gamma^\mu\chi_L + g_{\chi_R}\bar{\chi}_R\gamma^\mu\chi_R\right] \tag{2.56}$$

where the index f runs over all the SM fermions, and the transformed couplings are defined as

$$\begin{aligned}g^V_f &= \frac{1}{2}(g_{f_R}+g_{f_L}) \\ g^A_f &= \frac{1}{2}(g_{f_R}-g_{f_L})\end{aligned} \tag{2.57}$$

While it has been shown that the different couplings in Eq. (2.56) must obey non-trivial constraints among them if unitarity and gauge invariance are imposed [76, 77], this framework could be considered a minimal parametrization of richer models, that could feature more than one mediator and/or new dark states beyond Z' and χ.

For the direct search of such signals in hadron colliders such as the LHC, since the final-state particles are not detectable, a visible detector signature must be able to identify and record such events. Energetic hadronic jets accompanying the DM pair are typically used to trigger signal candidates, but also the presence of other SM particles (like γ, Z or W) is used to this task. Therefore the experimental signature comprises one or more energetic jets and a large missing transverse momentum. While the latter is the intrinsic result of the BSM particle and antiparticle escaping the detector without leaving any trace, hadronic jets are produced either as a result of initial-state gluon radiation or due to the hadronic decays of energetic heavy SM vector bosons (denoted in the search as V) produced in association with the fermionic DM.

Chapter 3

Light top-philic New Physics in four-top production at LHC

En este capítulo estudiamos el estado final de cuatro tops en el LHC como prueba de la existencia de partículas de NF que se acoplan predominantemente al quark top y cuyas masas están por debajo del umbral de producción de pares de tops. Nos centramos en modelos simplificados con una partícula hipotética de espín 0, espín 1 o espín 2, y encontramos puntos de referencia compatibles con los resultados experimentales. Exploramos las diferencias cinemáticas entre estos modelos y el ME a nivel partónico y a nivel reconstruido. En este último caso, restringimos el análisis al canal de dos leptones del mismo signo. Investigamos cómo las diferentes estructuras de Lorentz de la NF ligera afectan la dureza cinemática, la polarización, las correlaciones de espín y las distribuciones angulares de las partículas a nivel partónico y/o a nivel estado final. Los resultados proporcionan nuevas perspectivas para sondear NF liviana top-fílica y para identificar y distinguir cada firma considerada, enmarcado dentro del programa experimental en curso de búsquedas de producción de cuatro tops, dentro de la segunda puesta en funcionamiento del LHC y las venideras.

Within this chapter we study the four-top final state at the LHC as a probe for NP particles that couple predominantly to top quarks and whose masses are below the top-pair production threshold. We focus on simplified models with a spin-0, spin-1, or spin-2 hypothetical particle, and find benchmark points compatible with experimental results. We explore kinematic differences between these models and the SM at the parton level and the reconstructed level. In the latter, we restrict the analysis to the two same-sign leptons (2LSS) channel. We investigate how the different Lorentz structures of the light NP affect the kinematic hardness, polarization, spin correlations, and the angular distributions of the parton-level and/or final state particles. The results provide new handles to probe for light top-philic NP and to identify and distinguish each considered signature, as part of the ongoing experimental program of searches for four-top production at the LHC Run 2 and beyond.

3.1 Introduction

Over the next years, while the LHC Run 3 completes, the HEP community will be devoted to the scrutiny of all available LHC data, as well as to the proposal of new promising experimental directions, in search of new hints for possible SM extensions. Among these upcoming results, few processes are beginning to be tested experimentally using the full Run 2 dataset, and whose measurement is directly sensitive to NP contributions. Of particular interest are Higgs-boson-pair (hh) production [78–80], the associated production of a Higgs boson with a top-pair ($t\bar{t}h$) [81–83], and four-top ($t\bar{t}t\bar{t}$) production [84–86]. The first two processes, hh and $t\bar{t}h$, will deliver crucial direct information on the Higgs potential and the top-quark Yukawa coupling, respectively. The latter, $t\bar{t}t\bar{t}$, can also be used to probe the top quark Yukawa coupling, the Higgs boson width [87, 88], and anomalous off-shell Higgs behavior [89]. Moreover, it has a unique sensitivity to light top-philic NP, and thus represents an exciting opportunity for discovering new particles at the LHC. This is the main motivation behind the scope of this chapter.

Many BSM scenarios usually predict an enhanced rate of events containing four top quarks in the final state, compared to the SM production via the strong interaction. In the bibliography can be found theory and phenomenology proposals considering $t\bar{t}t\bar{t}$ as a sensitive final state for top-philic NP [28, 36, 39, 90–97]. Most of these articles consider heavy NP particles, above the $t\bar{t}$ production threshold ($M > 2m_t$). For that reason, the goal of this chapter is to study phenomenology in four-top production at the LHC caused by hypothetical light particles.

The direct observation of events leading to a measurement of the $t\bar{t}t\bar{t}$ cross-section is unlikely, because of the large $t\bar{t}$ background. The SM four-top production cross-section is approximately five orders of magnitude smaller than that for top-pair production, and the production of four top quarks from proton-proton interactions has not yet been observed. Experimental searches for SM four-top production have been performed by the ATLAS and CMS Collaborations at 8 TeV [84, 85, 98, 99] and 13 TeV [86, 100–105]. Both experiments at the LHC may be just approaching sensitivity to this final state. In the process, each top quark primarily decays to a bottom quark and a W boson, and each W boson decays to either leptons or quarks, so top quark branching ratios are determined by the W branching ratios. The four-top-quark production events can give rise to different final states depending on the hadronic or semileptonic decay mode of each of the top quarks. Therefore, the aforementioned searches have focused on either the single-lepton (1L) and opposite-sign dilepton (2LOS) channels, or the same-sign dileptons (2LSS) and multilepton (ML) channels. In all cases the final states signatures are remarkable, featuring in addition to the leptons, a high multiplicity of jets, four of which originate from the hadronization of b-quarks (b-jets).

Although the four-top decay branching ratio is larger in the 1L and 2LOS channels, these searches are extremely challenging due to the overwhelming background from $t\bar{t}$ production in association with heavy-flavor jets, which suffers from large uncertainties in its theoretical modeling. In contrast, searches in the 2LSS and ML channels have lower signal yield, but also much more manageable backgrounds. The main backgrounds primarily originate from $t\bar{t}W$, $t\bar{t}(Z/\gamma^*)$, and $t\bar{t}H$ production, as well as from $t\bar{t}$ production with additional leptons from heavy-flavour hadron decays, misidentified jets, or photon conversions, and other processes where the electron charge is incorrectly assigned.

The most sensitive search for SM four-top production to date has been performed by the CMS Collaboration considering the 2LSS and ML channels, and using the full Run 2 dataset, corresponding to 137 fb^{-1} of integrated luminosity at $\sqrt{s} = 13$ TeV [86]. The observed (expected) significance for the SM four-top signal is 2.6 (2.7) standard deviations (s.d.), and the measured value of the SM four-top cross-section is $\sigma^{\text{meas}}_{t\bar{t}t\bar{t}} = 12.6^{+5.8}_{-5.2}$ fb, in agreement with the SM prediction of $\sigma^{\text{SM}}_{t\bar{t}t\bar{t}} = 12.0^{+2.2}_{-2.5}$ fb [106], which includes NLO QCD and electroweak effects. The resulting ratio between the measured and predicted cross-sections is $\mu_{t\bar{t}t\bar{t}} = \sigma^{\text{meas}}_{t\bar{t}t\bar{t}}/\sigma^{\text{SM}}_{t\bar{t}t\bar{t}} = 1.05^{+0.52}_{-0.48}$. Therefore, an enhancement in the four-top production cross-section due to NP contributions of up to a factor of 1.5 (2.0) is still compatible with the measurements at about 1 s.d. (2 s.d.) level.

The four-top signal at the LHC is a relatively new subject, and from this overview, the proposal within this chapter is to analyze the impact that the presence of light top-philic NP would have on this final state. In order to define the extent of our study, in Section 3.2 we revise a set of effective NP models, already defined in Chapter 2, containing new particles with either spin 0, spin 1, or spin 2, which couple predominantly to the top quark and whose masses are below the $t\bar{t}$ production threshold. We study existing constraints in these NP models arising from searches for di-photon ($\gamma\gamma$) resonances and four-top production in 3.2.1, and we define suitable benchmark points in the parameter space of each model compatible with experimental results in 3.2.2. The analysis of the phenomenology on some of these benchmark points in the four-top production can be found in Section 3.3, where we concern both in parton level observables as well as in detector level effects.

3.2 NP models

Along with this chapter, the aim is to study how simple NP models would affect $t\bar{t}t\bar{t}$ phenomenology at the LHC, and how could they be recognized and distinguished. We consider models whose effects are expected to be more important in four-top production rather than in other processes. This is the case of new particles whose couplings are predominantly to the top quark and whose mass M is below the $t\bar{t}$ threshold ($M < 2m_t$) to avoid resonance effects in $t\bar{t}$ production. Moreover, we restrict to those that are color neutral to avoid interactions with gluons that would yield a large QCD-mediated production cross-section. For this purpose we focus on the four top-philic simplified models described in Chapter 2, in Section 2.3:

a. Scalar ϕ

b. Pseudo-scalar A

c. Vector Z'

d. Graviton G

Some representative Feynman diagrams for the $pp \to t\bar{t}t\bar{t}$ process are presented in Fig. 3.1. The lowest-order Feynman diagrams illustrating typical contributions to SM four-top production via gluon fusion are shown Figs. 3.1(a), 3.1(b) and 3.1(d). These diagrams are higher-order diagrams in quantum chromodynamics (QCD) when compared with the LO diagrams for top-pair production, and explain the extremely small SM predicted cross-section (of $\sigma^{\rm SM}_{t\bar{t}t\bar{t}} = 12.0^{+2.2}_{-2.5}$ fb [106]). The NP diagrams in Fig. 3.1 are essentially the same for all the simplified models, except for the case of the Graviton model, which provides extra Feynman diagrams like the one in Fig. 3.1(c). In this model, in addition to the coupling between the resonance and the top-quark pair, SM gauge invariance introduces 4-point interactions that include the resonance, the top-quark pair, and a SM gauge boson. This represents a distinctive feature of the model, since there are Feynman diagrams in $pp \to t\bar{t}t\bar{t}$ production that are not present in the other models, and provides unique effects in the phenomenology, as will be seen along with this chapter.

In the following, there is a full description of the bounds affecting these models in 3.2.1, and in 3.2.2 we describe the signal points selection.

3.2.1 NP models' constraints

Since we restrict our study to cases where the mass of the NP resonance is below the $t\bar{t}$ production threshold ($M \lesssim 350$ GeV), the constraints on the models considered in Section 3.2 would mainly come from NP loop corrections to $t\bar{t}$ near threshold, $\gamma\gamma$ resonance searches, and $t\bar{t}t\bar{t}$ at the LHC.

Loop corrections to $t\bar{t}$ production have been studied for Higgs and electroweak gauge bosons [107]. Although it is not possible to directly extract bounds on the presented NP models from the available results, adapting these computations for spin-0 and spin-1 NP contributions, as well as including spin-2 corrections and the corresponding interference with SM contributions, could provide relevant constraints on the models. This objective lies beyond our scope; however, given the precision reached in $t\bar{t}$ production and its recent application in constraining the top-quark Yukawa coupling [108], we estimate that results near the $t\bar{t}$ threshold should be interesting concerning our effective NP models.

Searches in $\gamma\gamma$ final state have no constraints for a spin-1 particle, since it cannot decay to $\gamma\gamma$ due to the Landau-Yang theorem [40, 41]. New particles with spin $\neq 1$ can be created in gluon fusion through a top-quark loop and also decay into a $\gamma\gamma$ or jj final state through a top-quark loop, as further discussed in Section 2.3 (decay widths for each model are available in Appendix A). Since parton-level calculations yield a ratio of S/B ($S/\sqrt{B}$) between $\gamma\gamma$ and jj final states of $\sim 10^5$ (~ 10), and since there are no updated jj resonance searches in the relevant region of invariant masses, we only consider $\gamma\gamma$ resonance searches. The latter represent an extensive program by both ATLAS [109–111] and CMS [112, 113] Collaborations.

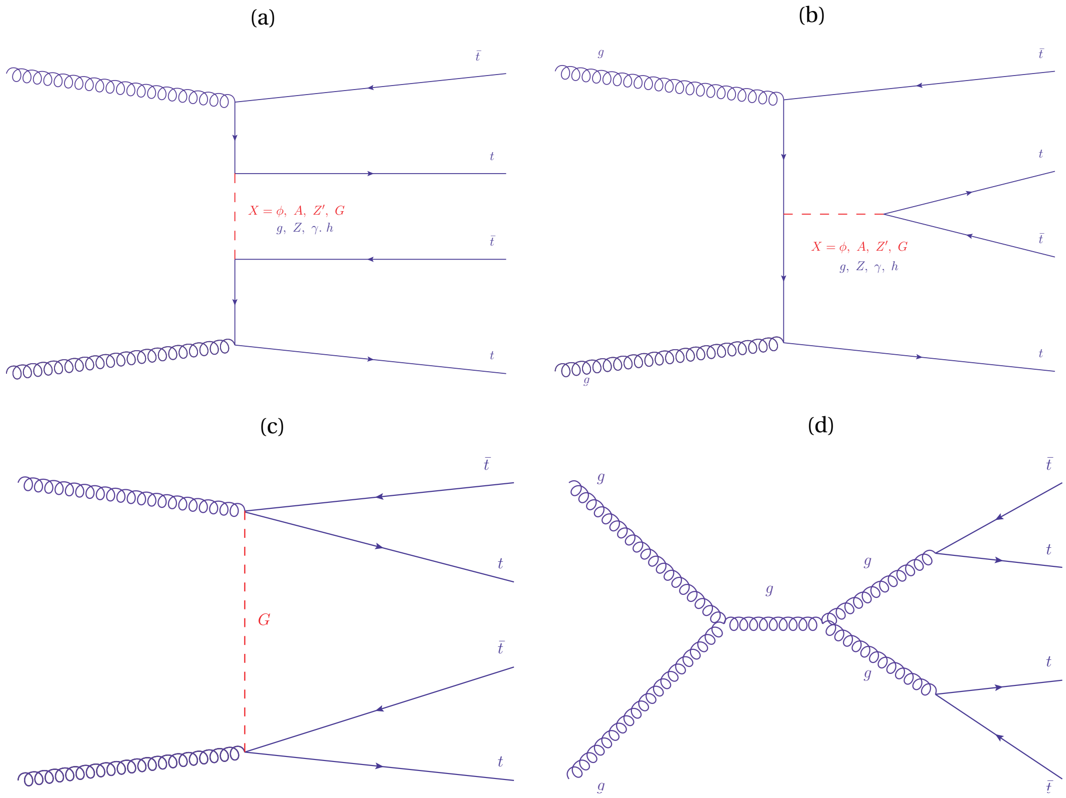

FIGURE 3.1. Representative Feynman diagrams for the $pp \to t\bar{t}t\bar{t}$ process at the LHC where, at $\sqrt{s} = 13$ TeV, approximately 90% of the production cross-section is through gluon fusion. In (a) and (b) the dashed line may correspond to any of the NP particles considered in this work (ϕ, A, Z' or G), in addition to the SM particles (g, Z, γ and Higgs). Diagram (c) is only allowed in the spin-2 NP model, where the 4-point interaction is required to ensure gauge invariance. Diagram (d) correspond to a typical QCD SM diagram. Diagrams (a) and (c) are important for not having s-channel suppression. In particular, in diagram (c) the Graviton model provides four-top production through only 2 vertices without s-channel suppression and with all four top quarks on an equal footing, which provides distinctive features (see 3.2.1 for further details)

We have scanned the parameter space of the relevant models and compared the predicted cross-sections with the available experimental bounds. The details of the simulations are described in Appendix B. These bounds are shown in Fig. 3.2. The $\gamma\gamma$ resonance searches provide important bounds for the spin-0 NP models, being more restrictive for the pseudo-scalar case. On the other hand, for the spin-2 model, the $t\bar{t}t\bar{t}$ cross-section is enhanced by the extra Feynman diagrams compared to the other NP scenarios (see Fig. 3.1(c)). Thus for regions in parameter space with the same four-top cross-section as in the spin-0 models, the $\gamma\gamma$ process has a smaller cross-section in the spin-2 model. As a result, the spin-2 model remains rather unconstrained by the available $\gamma\gamma$ resonance searches.

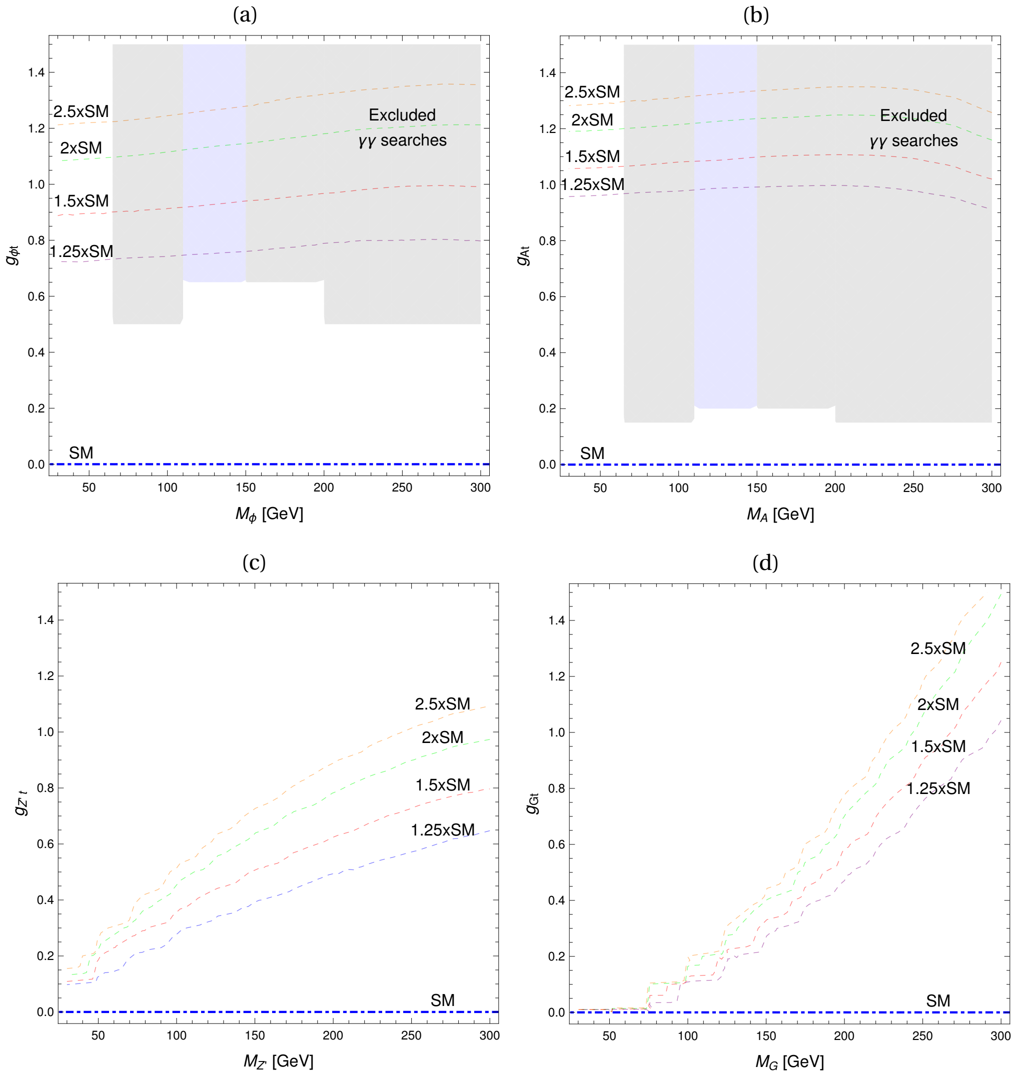

FIGURE 3.2. Four-top production cross-section contour levels (in units of the SM cross-section) in the coupling strength versus resonance mass plane for the different NP models considered; (a) Scalar, (b) Pseudo-scalar, (c) Z' and (d) Graviton. The Z' and Graviton models exhibit a larger four-top production cross-section dependence on the resonance mass since the NP is coupled to an unconserved current, as explained in the text. Values of the predicted cross-section above about 2×SM are excluded at the 95% CL by the latest four-top search at the LHC (under the assumption of SM kinematics). The gray shaded area represents the region excluded by $\gamma\gamma$ resonance searches. The light-blue shaded region corresponds to an interpolation since there are not available general $\gamma\gamma$ searches in the 110 GeV - 150 GeV range, where the $H \to \gamma\gamma$ signal is measured and no other excesses are observed. In the case of the Z' and Graviton models, such $\gamma\gamma$ resonance searches do not yield significant constraints: the Z' resonance cannot decay into $\gamma\gamma$, whereas the Graviton model considered is less sensitive to $\gamma\gamma$ searches as explained in the text.

As discussed in Sect. 3.1, the most sensitive $t\bar{t}t\bar{t}$ search to date [86] excludes at the 95% CL values of the $t\bar{t}t\bar{t}$ cross-section larger than approximately a factor of two larger the SM prediction (under the assumption of SM kinematics), thus still leaving enough room for light top-philic NP contributions. In Fig. 3.2 can be found the contour-levels of the predicted SM+NP cross-sections in units of the SM cross-section. Simulations are in equal conditions for SM and NP, which is equivalent to using the same NLO k-factor for both scenarios. Details on the simulation process are given in Appendix B.

One feature to be said about the contour levels in Fig. 3.2 for the spin-1 case, as pointed out in Ref. [36], is that having the Z' coupled to an unconserved current such as $\bar{t}_R\gamma^\mu t_R$ yields a factor $(m_t/M)^2$, due to the longitudinal polarization of the vector propagator. For small M this translates into an enhancement in the $t\bar{t}t\bar{t}$ cross-section, as can be seen in Fig. 3.2(c). We have explicitly verified that if we use the conserved fermionic current ($\bar{t}\gamma^\mu t$) instead, then this enhancement for small M disappears and the behavior is more similar to the spin-0 case, where the coupling is to a conserved current.

It is interesting to notice that, although LO electroweak corrections represent a minor correction of $\sim 5\%$ to the SM cross-section, their fractional contribution is enhanced when NP effects are included. This could be expected, since it has been shown in Ref. [106] that SM LO contributions of $\mathcal{O}(\alpha_s^3\alpha)$ and $\mathcal{O}(\alpha_s^2\alpha^2)$ are both sizable but have opposite sign, leading to a large accidental cancellation. Therefore, any NP contribution that affects the interference terms may break this cancellation at this order, thus resulting in larger contributions to the total cross-section. As stated in Ref. [106], similar behavior is also expected at NLO, where there is also a cancellation between SM contributions of different orders. In general, we find that this enhancement at LO is due to the interference of the SM particles with those NP particles with the same quantum numbers. Fig. 3.3 displays the fractional contribution of the SM+NP interference to the total $t\bar{t}t\bar{t}$ cross-section, in the parameter space for each of the NP models considered. For many of the relevant benchmarks defined below in 3.2.2, the inclusion of electroweak diagrams can account for a modification in the $t\bar{t}t\bar{t}$ cross-section of up to $\sim 30\%$, all at LO.

3.2.2 NP Benchmark Points

In order to study the NP phenomenology in four-top production, we define in each NP model a set of benchmark points (BP) for a representative sample of NP masses and couplings still allowed by the available data, according to what is stated in 3.2.1. For each assumed mass (M) in a given NP model, we define a tight (T) and a loose (L) BP for which the $t\bar{t}t\bar{t}$ cross-section equals 1.5 and 2 times the SM cross-section, respectively. These signal points are denoted as $\mathrm{BP}^{NP}_{T,L}(M)$. Since the spin-0 NP models are excluded by $\gamma\gamma$ resonance searches for masses above 65 GeV, the selection includes BPs below this mass value. For other NP models, we consider masses of 50 GeV, 150 GeV, and 300 GeV where possible. In Table 3.1 we display the values for the couplings and masses in each NP model, which define the BPs.

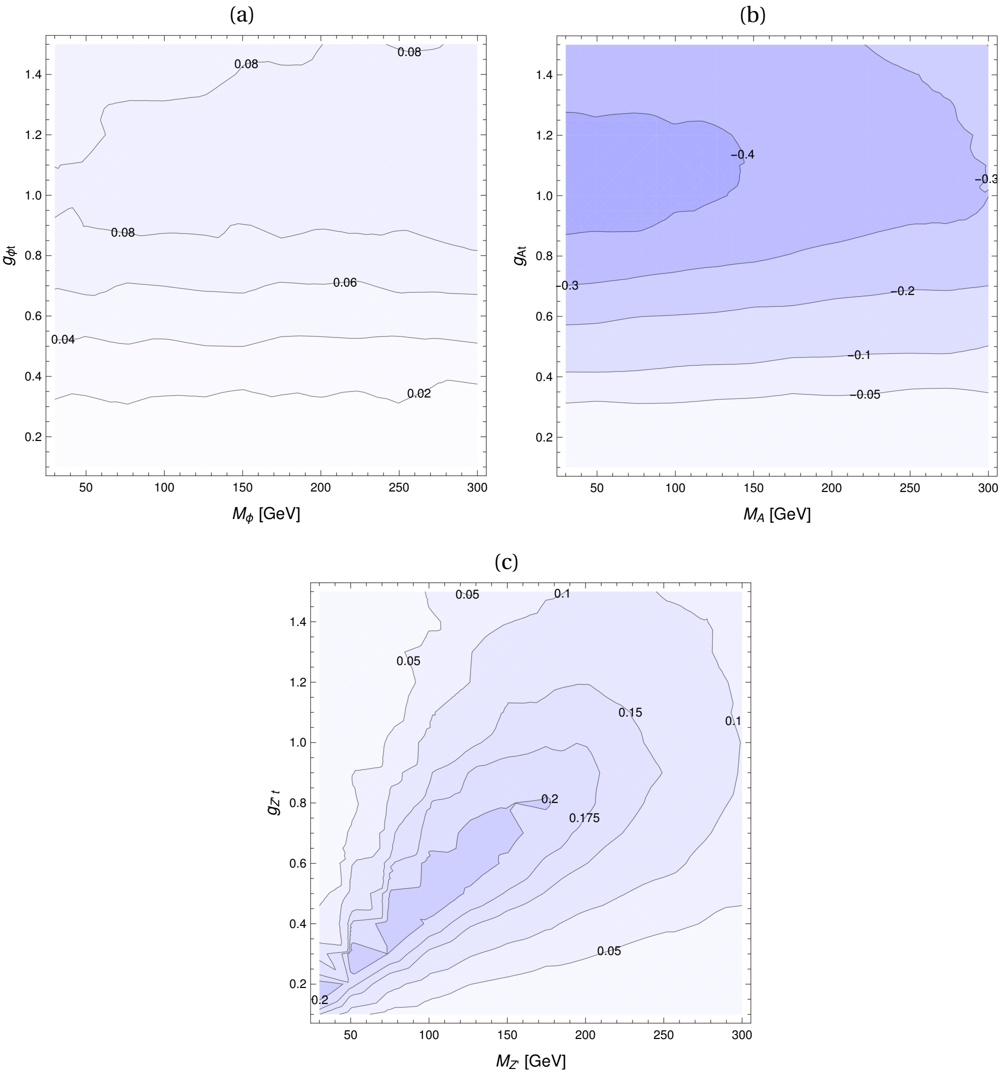

FIGURE 3.3. Fraction of the contribution to the total $pp \to t\bar{t}t\bar{t}$ cross-section due to interference between SM (QCD+QED) and NP for three of the NP models considered; (a) Scalar, (b) Pseudo-scalar and (c) Z'. It is important to stress that the interference is enhanced by including QED corrections, as discussed in text. In the Pseudo-scalar benchmark points the interference may reach up to $\sim -70\%$ of the total SM LO cross-section. The interference for the Graviton benchmark points –not shown– is negligible in the relevant region.

3.3 Phenomenology of non-resonant light NP in $t\bar{t}t\bar{t}$

As discussed in Section 3.1, after the decay of the top quarks, a four-top event features a very busy final state with at least twelve energetic partons, including eventual neutrinos. Therefore, it is extremely challenging the kinematic reconstruction of the final state. In the case of the highest sensitivity channels, 2LSS and ML, the presence of multiple neutrinos makes very difficult the kinematic

Spin-0	$g_{\phi/At}$	Spin-1	$g_{Z't}$	Spin-2	g_{Gt}
BP_T^{ϕ}(30 GeV)	0.90	$\text{BP}_T^{Z'}$ (50 GeV)	0.20	BP_T^{G} (150 GeV)	0.33
BP_L^{ϕ}(30 GeV)	1.09	$\text{BP}_L^{Z'}$ (50 GeV)	0.24	BP_L^{G} (150 GeV)	1.25
BP_T^{ϕ}(50 GeV)	0.91	$\text{BP}_T^{Z'}$ (150 GeV)	0.51	BP_T^{G} (300 GeV)	0.40
BP_L^{ϕ}(50 GeV)	1.10	$\text{BP}_L^{Z'}$ (150 GeV)	0.64	BP_L^{G} (300 GeV)	1.49
BP_T^{A}(30 GeV)	1.06	$\text{BP}_T^{Z'}$ (300 GeV)	0.80		
BP_L^{A}(30 GeV)	1.06	$\text{BP}_L^{Z'}$ (300 GeV)	0.97		
BP_T^{A}(50 GeV)	1.19				
BP_L^{A}(50 GeV)	1.20				

TABLE 3.1. Benchmark points (BP) selected to study NP effects in four-top phenomenology. Subscripts T and L stand for tight and loose, for which the four-top production cross-section is 1.5 and 2 times larger than the SM cross-section, respectively.

reconstruction of the leptonically decaying top quarks, although the hadronically decaying top quarks can potentially be reconstructed, particularly if they have a significant boost.

For definiteness, in the following, we will restrict our study to the 2LSS channel, which features two same-sign leptons, significant $E_{\text{T}}^{\text{miss}}$ because of the presence of two neutrinos, and at least eight jets, four of which are b-jets. This choice is appropriate, since the 2LSS channel is one of the most sensitive search channels, although most of our findings will also apply to the ML channel, which is dominated by events with exactly three leptons. We consider several inclusive observables, assuming that kinematic reconstruction is either not available, or too inefficient to be helpful. One of such observables is the total transverse energy H_{T}, defined as the scalar sum of the transverse momentum of all jets, leptons, and missing energy in the event. This observable is a trivial extension of the $H_{\text{T}}^{\text{jets}}$ variable, which only includes the jets in the sum, which is typically used by the ATLAS and CMS collaborations in their four-top analyses.[1] However, we find that H_{T}, including more information on the event final state objects, is slightly more sensitive. In any case, we have verified that the results are qualitatively similar when using either of the two variables. We also define and investigate tt (or $\bar{t}\bar{t}$) spin correlations using the angular separation between the same-sign leptons. We study the feasibility of using these observables to distinguish NP contributions from the SM and to discriminate among different NP scenarios.

For this study, we generate $pp \to t\bar{t}t\bar{t}$ at LO, including all SM and NP diagrams, for each of the BPs defined in Table 3.1. The generated events properly account for the helicity transmission in the decay of the two same-sign top quarks and are showered and processed through a simplified simulation of the ATLAS detector, followed by the reconstruction of detector-level physics objects. For our LO simulations, we added a k-factor of 1.26 extracted from Ref. [86, 106] (see Appendix B for details). Events preselection criteria, based in Ref. [102], includes exactly two same-sign leptons, $H_{\text{T}}^{\text{jet}} > 300$ GeV, $E_{\text{T}}^{\text{miss}} > 50$ GeV, and either ≥ 5 jets of which at least three are b-tagged, or ≥ 6 jets of

[1] Note that ATLAS and CMS use "H_{T}" to refer to what we define as $H_{\text{T}}^{\text{jets}}$.

which at least two are b-tagged.

3.3.1 Total transverse energy

The total transverse energy H_T is a variable that provides a measure of the hardness of an event, and usually, a lower cut in H_T is used in searches for very massive final states such as those from $t\bar{t}t\bar{t}$, to suppress important backgrounds, such as $t\bar{t}$. The aim of studying this variable in the context of light NP contributions in four-top production is not only to distinguish NP signatures but also to explore whether H_T cuts guided by SM four-top searches may inadvertently suppress NP contributions.

Fig. 3.4 displays the H_T distribution for each of the NP models considered. Interestingly, in the case of the spin-0 and spin-1 NP models, the H_T distribution for SM+NP is found to be slightly softer than that expected for the SM only. This kind of deviation in the H_T would typically be attributed to a background mismodeling, and thus potentially missed by current experimental searches. In contrast, the SM+NP distribution for the spin-2 NP model is distinctly harder than the SM prediction, possibly more in line with what is typically expected for ultra-heavy NP, described via an EFT, although in this case, we are considering a very light particle. This can be attributed to the presence of diagrams such as in Fig. 3.1(c), where there is a symmetry such that the available energy is on average equally distributed among the top quarks in the center-of-mass frame. Using Lagrange multipliers it can be shown that the maximization of the scalar sum of the top-quark 3-momenta, while constrained to be all on-shell, is obtained for equally distributed energies. This is an effect that increases with the mass/energy ratio of the top quarks.

3.3.2 Spin correlations in four-top events

A second observable that is interesting to study in four-top events, and that does not require reconstructing the four-top system, is the spin correlation between a pair of top quarks. It is easy to appreciate that, depending on the type of the NP particle X exchanged in Fig. 3.1(a), the ttX vertex has a different Lorentz structure, which in turn affects the spin correlation between the top and antitop quarks in the same fermionic line. This effect is also transmitted to the same-sign top quarks in different fermionic lines. In this section, we study the spin correlation between same-sign top quarks via their corresponding reconstructed leptons in the 2LSS channel.

We first investigate the spin correlation at the parton level by constructing an asymmetry between like and unlike same-sign top-quark helicities. Then, we select events in the 2LSS channel and study the azimuthal separation in the laboratory frame between the reconstructed same-sign leptons, $\Delta\phi(\ell^\pm,\ell^\pm)$. In the following paragraphs, we present results for same-sign top quarks (tt) and same-sign positive leptons ($\ell^+\ell^+$), but the same conclusions apply to same-sign antitop quarks ($\bar{t}\bar{t}$) and same-sign negative leptons ($\ell^-\ell^-$).

At the parton level one can quantify the spin correlation between the top quarks by defining an asymmetry between the cross-sections for Like (L) and Unlike (U) top-quark helicities, as given by:

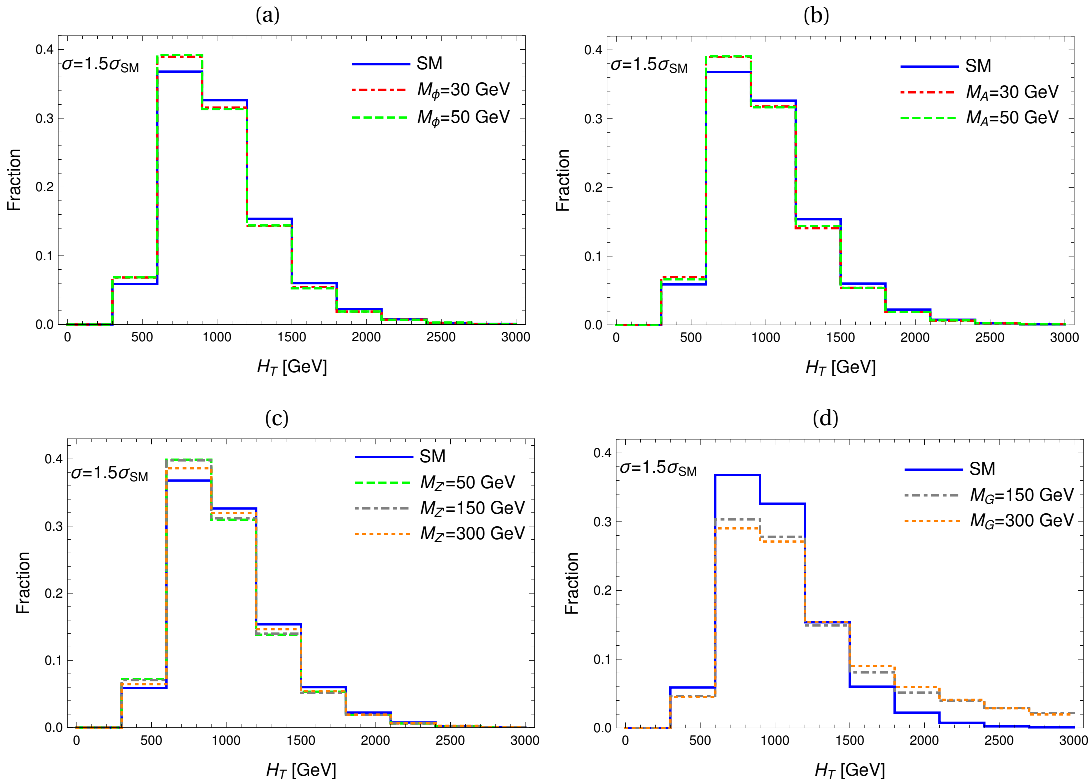

FIGURE 3.4. Distribution of the H_T variable for the 2LSS channel after preselection (see text for details), normalized to unit area. Shown are the predictions for the SM (blue) and the tight benchmark points (i.e. giving $\sigma = 1.5\sigma_{SM}$) of the NP models considered: (a) Scalar, (b) Pseudo-scalar, (c) Z', and (d) Graviton. The distinctive behavior in the Graviton is due to the symmetry in one of its main Feynman diagrams (see Fig. 3.1(c)), as explained in the text. Analogous results for the loose benchmark points (i.e. giving $\sigma = 2\sigma_{SM}$) are shown in Fig. C.1 in Appendix C.

$$A^{L/U}_{\text{tt-hel}} = \frac{\sigma(t_+t_+) + \sigma(t_-t_-) - \sigma(t_+t_-) - \sigma(t_-t_+)}{\sigma(t_+t_+) + \sigma(t_-t_-) + \sigma(t_+t_-) + \sigma(t_-t_+)} \quad (3.1)$$

where $\sigma(t_i t_j)$ denotes the cross-section for $t\bar{t}t\bar{t}$ production with the two top quarks (tt) having helicities i and j, respectively, summed over the antitop-quark helicities.

Fig. 3.5 displays the $A^{L/U}_{\text{tt-hel}}$ asymmetry as a function of the four-top invariant mass in the SM, as well as for the different NP BPs considered. We find negative contributions to $A^{L/U}_{\text{tt-hel}}$ in the Scalar case, a slightly negative contribution in the Pseudo-scalar case, a positive (negative) contribution in the Z' case with high (low) mass, and a large positive contribution in the Graviton case. The two latter results could be expected, since the Z' and Graviton contributions include only right-chiral top quarks which, at higher energy, are likely to have positive helicity.

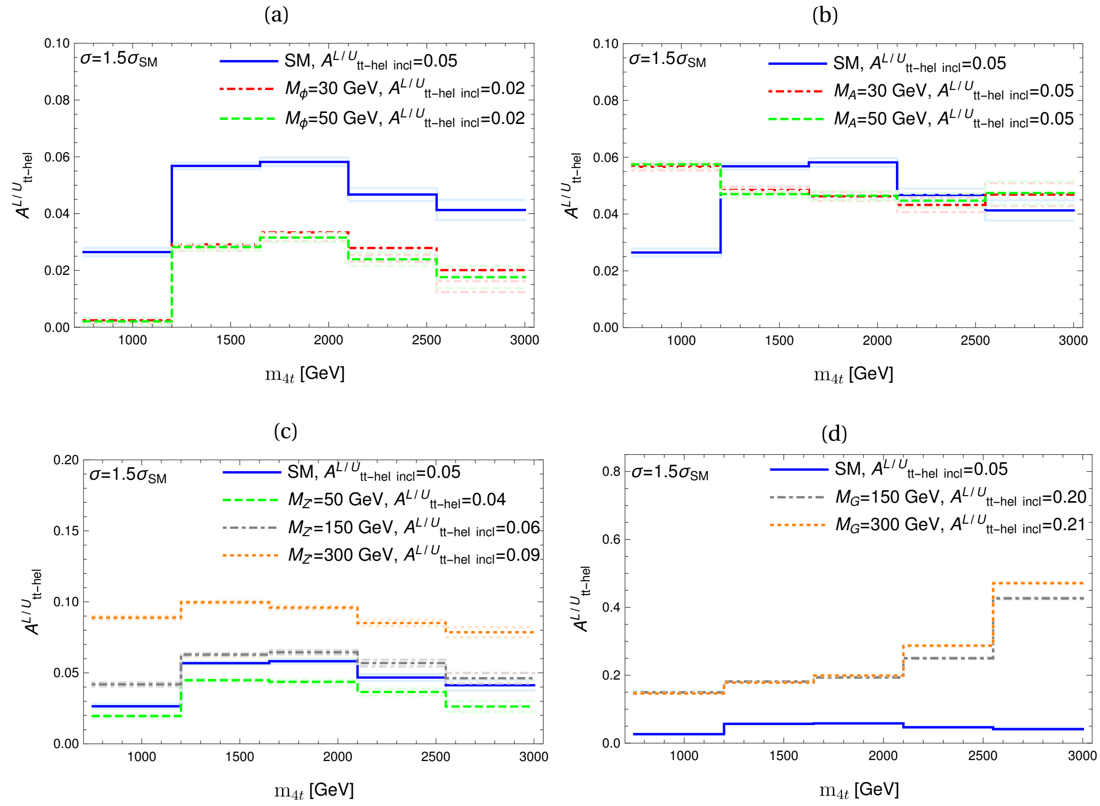

FIGURE 3.5. $A^{L/U}_{\text{tt-hel}}$ asymmetry (see Eq. (3.1)) as a function of the invariant mass of the four-top system. Shown are the predictions for the SM (blue) and the tight benchmark points (i.e. giving $\sigma = 1.5\sigma_{SM}$) of the NP models considered: (a) Scalar, (b) Pseudo-scalar, (c) Z', and (d) Graviton. Also quoted are the inclusive asymmetries, i.e. averaged over the four-top invariant mass spectrum. Analogous results for the loose benchmark points (i.e. giving $\sigma = 2\sigma_{SM}$) are shown in Fig. C.2 in Appendix C.

In contrast to $t\bar{t}$ production, since $t\bar{t}t\bar{t}$ is a four-body final state, the translation from these top-quark polarization asymmetries to the angular separation between leptons is not straightforward. The angular separation between the top quarks, which depends on the underlying dynamics, also affects the angular separation between the final-state leptons. This distribution, together with $A^{L/U}_{\text{tt-hel}}$ (see Fig. 3.5), provides some insights into what can be expected for the angular distribution of the top-quark-decay products. In Fig. 3.6 we display the azimuthal separation between the two same-sign top quarks, $\Delta\phi(t,t)$, for the dominant helicity configurations in each of the NP scenarios considered. In particular, for the Z' and Graviton modes we show the t_+t_+ configuration because this final state represents 33% and 47% of the total cross-section, respectively. A suppression (enhancement) in the back-to-back configurations for the top quarks in these helicity configurations tends to suppress (enhance) the back-to-back configuration between their corresponding same-sign leptons.

When considering spin-correlation observables in four-top events, the simplest observable is the

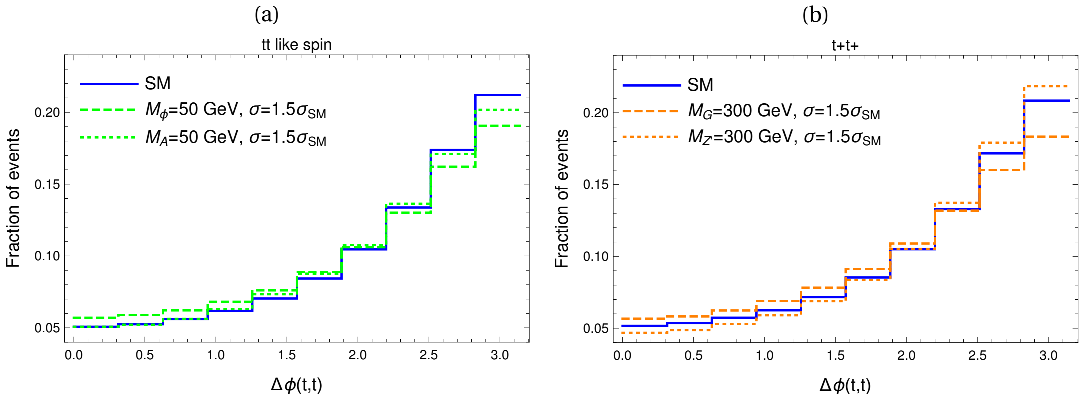

FIGURE 3.6. Distribution of the azimuthal separation between the same-sign top quarks, $\Delta\phi(t,t)$, normalized to unit area. Shown are the predictions for the SM (blue) and the tight benchmark points (i.e. giving $\sigma = 1.5\sigma_{SM}$) of the NP models considered for the dominant helicity configurations: (a) Scalar and Pseudo-scalar, (b) Z' and Graviton.

azimuthal separation between same-sign leptons, $\Delta\phi(\ell^+,\ell^+)$, in the 2LSS and ML channels. Fig. 3.7 shows a comparison of the predicted $\Delta\phi(\ell^+,\ell^+)$ distribution in the 2LSS channel after preselection, between the SM and the tight benchmark points (i.e. giving $\sigma = 1.5\sigma_{SM}$) of the NP models considered. As can be appreciated, the Scalar and Pseudo-scalar models are characterized by a depletion of back-to-back SS leptons compared to the SM. In the case of the Z' model, there is an enhancement (depletion) of back-to-back SS leptons for high (low) mass. Surprisingly, the Graviton model does not display a significant difference from the SM distribution. This appears to be (at least partly) explained by an accidental cancellation of effects in the parton-level polarizations (see Fig. 3.5) and the parton-level angular distributions (see Fig. 3.6).

3.4 Prospects from the analysis

The four-top signal at the LHC is a relatively new subject and the community is in the course of acquiring and processing knowledge on the many aspects of this final state. We have presented a set of results that raise new questions and challenges, which we discuss in the following paragraphs. We begin with a discussion concerning parton-level four-top production and then we examine the results concerning final state particles and detector-level results.

In our analysis, we have simulated four-top production at LO, and we have applied a k-factor to estimate NLO corrections to the total cross-section. However, we have found that for the studied BPs at LO, the interference between SM QCD+QED and NP amplitudes can account for a large fraction of the total cross-section, $\sim 30\%$. This suggests that a simulation of four-top production at NLO, including NP contributions, is required for a more precise interpretation of experimental results in terms of the parameter space of the NP models considered. This conclusion had been envisaged in previous NLO studies of SM four-top production [106, 114].

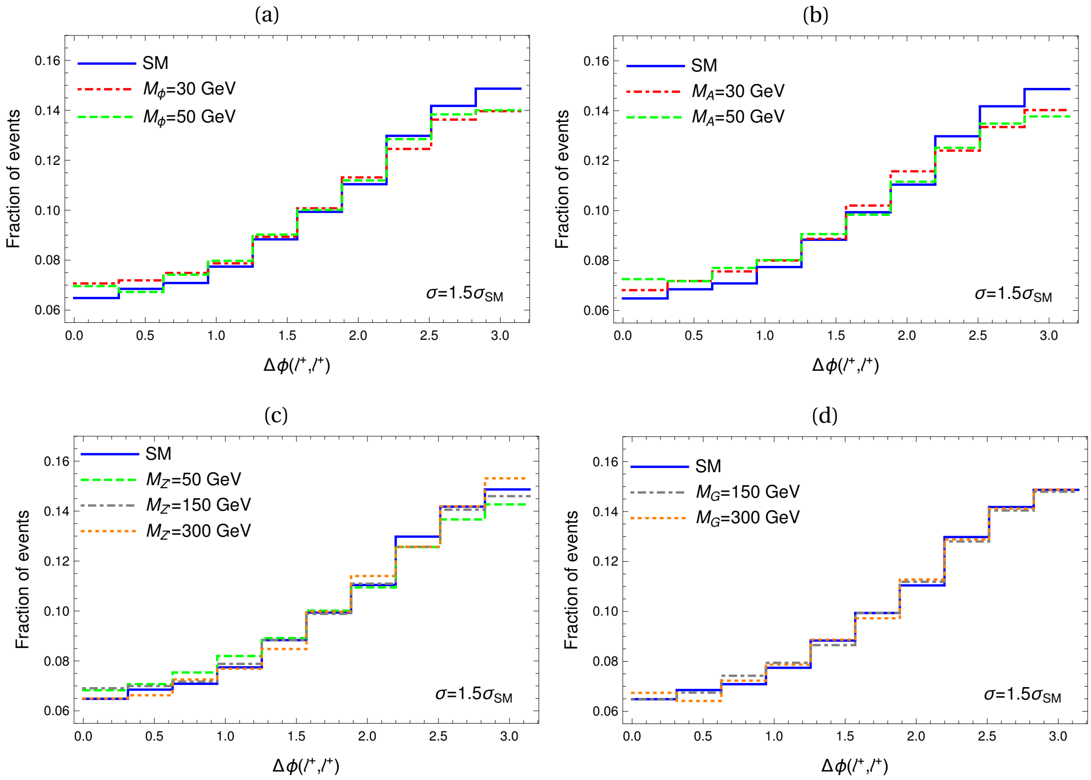

FIGURE 3.7. Distribution of the azimuthal separation between the same-sign leptons, $\Delta\phi(\ell^+,\ell^+)$, for the 2LSS channel after preselection (see text for details), normalized to unit area. Shown are the predictions for the SM (blue) and the tight benchmark points (i.e. giving $\sigma = 1.5\sigma_{SM}$) of the NP models considered: (a) Scalar, (b) Pseudo-scalar, (c) Z', and (d) Graviton. Analogous results for the loose benchmark points (i.e. giving $\sigma = 2\sigma_{SM}$) are shown in Fig. C.3 in Appendix C. These same results in two bins of H_T are shown in Figs. C.4–C.7 in Appendix C.

Since the reconstruction of the four-top final state is very challenging, one of the interesting observables after event selection is the distribution of the total transverse energy, H_T. The presented NP scenarios with light resonances that cannot be produced on-shell, tend to produce an H_T spectrum softer than the SM in the cases of spin-0 and spin-1 NP, whereas the spectrum is harder in the case of spin-2 NP. Interestingly, the latter is analogous to the effect from a heavy off-shell resonance [91]. The spin-2 NP model differs from the other models in the presence of extra Feynman diagrams that involve four-point interactions (see Fig. 3.1c). A softer H_T spectrum for spin-0 and spin-1 NP could lead to a bias in the measured four-top cross-section [86] since SM kinematics is usually assumed to estimate the acceptance and shape of the final discriminating variable. Further work in this direction would be interesting. Nevertheless, our results suggest that H_T is a useful observable to discriminate possible NP contributions, even in the case of new light particles.

The combined study of the parton-level polarization asymmetries and angular distributions, e.g. $\Delta\phi(\ell^+,\ell^+)$ in the 2LSS channel, is suggestive of a rich and exciting program yet to be developed related to the use of this kind of observables. Whereas the $\Delta\phi(\ell^+\ell^+)$ distribution can be used to probe spin-0 NP scenarios, the Graviton and Z' models would be better probed by studying the angular separation between two reconstructed top quarks. This means that new opportunities arise if one could reconstruct the top quarks. This could be achieved with large statistics in the 2LSS channel, using some of the sophisticated reconstruction algorithms already in use by the experimental collaborations. Alternatively, in the ML channel, useful information could also be extracted from the angular separation between one lepton and the reconstructed top quark. In general, the study of polarization effects in four-top production is an attractive field that requires further investigation.

Our study has focused on the spin correlation between same-sign top quarks in the 2LSS channel. We have shown that this observable is sensitive to NP, even though these same-sign top quarks do not share a common vertex in the Feynman diagrams. We consider that a similar analysis, but in the opposite-sign dilepton channel (i.e. with leptons coming from opposite-sign top quarks), could be potentially interesting. This has the advantage that opposite-sign top quarks can share a vertex in the Feynman diagrams, and therefore their relative spin would be sensitive to the Lorentz structure of the underlying physics. On the other hand, the 2LOS channel has a significantly lower signal-to-background ratio than the 2LSS and ML channels, plus in half of the cases the opposite-sign top quarks would not share a common vertex in the Feynman diagrams, thus potentially affecting the sensitivity.

The observables studied in this work could be helpful towards establishing an eventual deviation in four-top production. The level of model discrimination of these observables indicates that they could be exploited by the experimental analyses using LHC Run 3 data and beyond. In any case, the smoking gun for a light new particle with spin-0 (H or A) or spin-2 (G) could come from $pp \to H/A/G \to \gamma\gamma$ resonant production searches. Even more promising could be the study of the di-photon invariant mass spectrum in $pp \to t\bar{t}H/A/G(\to \gamma\gamma)$ production, owing to the more favorable signal-to-background ratio. We note that the $t\bar{t}\gamma\gamma$ final state has been studied so far only for a resonance in the SM Higgs mass region, and thus the extension of this search to a broader mass range would be extremely interesting. In the case of a light resonance with spin-1 (e.g. a Z'), potentially interesting processes would be $pp \to Z'j$ and $pp \to t\bar{t}Z'$, with $Z' \to \gamma\gamma^* \to \gamma\ell^+\ell^-$. Observe that the one-loop Feynman diagrams $gg \to Z'g$ and $Z' \to ggg$ with tops running in the internal lines, whose features can be found in Ref. [115], are key ingredients to study the previous processes. Further studies in these directions would be interesting as well.

CHAPTER 4

Z'-EXPLORER SOFTWARE: TESTING *Z'* AGAINST VISIBLE LHC DATA

Dado que explorar la fenomenología de una señal de NF requiere una gran cantidad de comprobaciones cruzadas con los datos experimentales disponibles, este capítulo tiene como objetivo presentar Z'-explorer, un software rápido y fácil de usar para probar modelos de Z' contra datos del LHC a $\sqrt{s} = 13$ TeV. Esta herramienta escrita en C++ solo requiere del usuario la masa del Z', los acoplamientos y los anchos parciales de decaimiento (o la sección eficaz de producción y las fracciones de decaimineto del Z' en su versión alternativa, Z'-explorer-BR), y estima la *fuerza* de todos los posibles canales visibles en el LHC, lo que permite determinar el canal más sensible para la detección/exclusión de un Z' determinado. Probamos Z'-explorer en el Modelo Estándar Secuencial, para recuperar sus cotas superiores actuales, y también lo probamos en el modelo $B-L$ presentado en el Capítulo 2, para explorar más a fondo el alcance del software y su enriquecedor resultado.

Since exploring the phenomenology of a NP signature requires a large number of cross-checks against available experimental data, this chapter aims to present Z'-explorer, a fast and easy-to-use software to test Z' models against LHC data at $\sqrt{s} = 13$ TeV. This C++ tool only requires from the user the Z' mass, couplings, and partial widths (or the Z' production cross-section and branching ratios in its alternative version, Z'-explorer-BR), and estimates the *strength* of all possible visible channels at the LHC, allowing to determine the most sensitive channel for a given Z' detection/exclusion. We test Z'-explorer on the Sequential Standard Model, to recast its current upper limits, and we also probe it on the $B-L$ model introduced in Chapter 2, to further explore the software scope and its enriching outcome.

4.1 Introduction

As previously shown in Chapter 2, the search of a Z' at the LHC, as for any other NP particle, is implemented in different decay channels. Taking into account only Z' visible decay modes, the possible final states explored at the LHC and their latest searches (to the date of our software release) are jj [116–118], $b\bar{b}$ [119], $t\bar{t}$ [120, 121], e^+e^- [122, 124], $\mu^+\mu^-$ [122, 124], $\tau^+\tau^-$ [125, 126], W^+W^- [127, 128], Zh [128]. These searches have been performed both by the CMS and the ATLAS Collaborations, and have superseded the results coming from other colliders such as Tevatron in most of the TeV scale [67]. Since testing all these channels while studying an specific NP model predicting a Z' particle is cumbersome, we present a new tool which would facilitate this enterprise.

Although the fraction of times a Z' decays to a given channel depends merely on its corresponding branching ratio, in experimental terms the acceptance and efficiency of the detector, the techniques to reconstruct particles, and the SM backgrounds affecting this final state are crucial to determining its exclusion/discovery sensitivity. These features also have an important dependence on the scale of energies considered, which depends on the sought Z' resonance mass. For instance, for the search of a Z' with $M_{Z'} \lesssim 1$ TeV at the LHC, we expect the dijet channel to have large QCD background, which dominates at low p_T. Whereas in the dilepton channel, the background is smaller in comparison, and thus the signal is likely cleaner and the channel more sensitive even though its branching ratio could be smaller. Moreover, since $\mu^+\mu^-$ channel has slightly more efficiency than e^+e^-, for equal branching ratios we can expect more sensitivity in $\mu^+\mu^-$. Considering also the W^+W^- decay mode, for the same above reasons the fully hadronic decay is hidden in QCD background, whereas the leptonic decays, although cleaner, are difficult to reconstruct due to missing energy. This scenario changes for larger masses, $M_{Z'} \gtrsim 2$ TeV. In such a case there is a more subtle interplay between the features discussed above. Not only because all backgrounds are highly reduced, but also because the techniques for detecting and reconstructing particles are also modified. In particular, in this high p_T regime, boosted massive particles, such as W boson or t quark, can decay in configurations where all particles are collimated in a single fat jet in the lab frame. This, in conjunction with a reduced QCD background, yields a favorable enhancement for channels such as hadronic W and top.

From this overview, we see that there are a variety of non-trivial ingredients which affect which is the best channel to exclude (or find) a given Z'. However, although all these features for each final state are individually complex, and still more when combined, their results are summarized in the exclusion plots reported in each experimental search.

It is of particular interest for developing our software to find a magnitude that condenses all the relevant information and estimates reasonably whether a signal point in Z' parameter space is excluded or not, and which is the most sensitive channel. From the phenomenological point of view, the information available on previous experimental searches in the different channels at given energy and luminosity can be incorporated into the determination of the most sensitive decay channel, through the extraction of the predicted experimental limits. All these features can be condensed in the *strength* ($\mathbb{S}$), defined as [129]

$$\mathcal{S} = \frac{\sigma_{\text{pred}}}{\sigma_{\text{lim}}} \tag{4.1}$$

where σ_{pred} is the Z' predicted cross-section times branching ratio times acceptance, and σ_{lim} is the corresponding expected experimental upper limit at the 95% CL. The difference in using expected instead of observed limits consists in considering the experimental techniques instead of eventual fluctuations in the data. In case the measured limit departs significantly from the predicted value, it would correspond to a discovery or a wrong prediction which in both cases should be addressed from another point of view.

On this basis, along with this chapter we present the software Z'-explorer which can make the mentioned computation automatically in a very simple manner and for a huge amount of points in NP parameter space. We make a full description of the software in Sections 4.2 and 4.3. Z'-explorer is a very simple tool that could be learned and used rapidly to scan parameter space while constructing Z' models or exploring pure Z' phenomenology. The only input required to test a Z' model from this phenomenological point of view would be its couplings and/or branching ratios to the allowed decaying channels.

There is available software that also aims to test NP models against available experimental data simply with connection to our proposal [131–136, 150]. Many of them are for specific NP models (such as supersymmetry), and others for specific processes (such as Dark Matter portal). Between those re-interpretation codes, micrOMEGAs [134] and ZPEED [136] are designed for general purpose Z' models. In micrOMEGAs, even though is a very complete software analyzing a variety of NP signatures, the Z' module only addresses the dilepton and dijet channels. On the other hand, ZPEED also includes interesting finite width and interference effects, however, its current analysis also is restricted to dijet and dilepton final states. Although our mechanism is more simplified than others in some aspects, it is reasonably solid and we analyze simultaneously all possible Z' decay channels while providing the quantitative strength for each one of them. Along Sections 4.4 and 4.5 we show some application examples to validate Z'-explorer output and illustrate its mains goals.

4.2 *Z'*-explorer: Frontend

4.2.1 Installation

Since Z'-explorer is built-in `C++`, the only installation prerequisite is to have a `C++` compiler in our system. We first download the main directory of the software (`/Z'-explorer/`) from [137]. Once in it, considering a Linux environment as an example, we open a terminal shell, and from the command line we set on `/lib/` folder and write the instruction to building the executable:

```
> cd lib
> make
```

The latter creates the executable file `program.out`, that allows to run Z'-explorer . No additional steps are required, except if changes in source code are done (in this case repeat the above before running). The same procedure must be repeated when using the alternative version of the software (but downloading `/Z'-explorer-BR/` instead).

4.2.2 Running

Before running, information about the Z' model must be provided through an incard text file, that must be stored as `/incard/card_1.dat`. One row corresponds to one benchmark point within the model to be explored, and its corresponding NP parameters should be specified in the following order (with each column separated by spaces):

$$M_{Z'}\; g_{u_L}\; g_{u_R}\; g_{d_L}\; g_{d_R}\; g_{c_L}\; g_{c_R}\; g_{s_L}\; g_{s_R}\; g_{b_L}\; g_{b_R}\; g_{t_L}\; g_{t_R}\; g_{e_L}\; g_{e_R}\; g_{\mu_L}\; g_{\mu_R}\; g_{\tau_L}\; g_{\tau_R}\; \Gamma_{inv}\; \Gamma_{WW}\; \Gamma_{Zh}\; \Gamma_{xx}$$

where $M_{Z'}$ is the Z' mass (in TeV), g_{f_L} and g_{f_R} are the Z' couplings to a given left and right-handed SM-fermion (except for neutrinos, which information is required through Γ_{inv}), and Γ_{WW} and Γ_{Zh} are the partial widths to W^+W^- and Zh. We require this latter information as partial widths since there is not a unique Lorentz structure in their couplings. The total width to non SM particles can be added as Γ_{xx} (if not, we leave Γ_{xx} as 0). To obtain the right form of the $g_{f_{L/R}}$ couplings from a given NP model, we strongly recommend to write interactions between Z' and SM fermions in the form of Eq. (2.21).

For those users that prefer to work with the Z' production cross-section ($\sigma(Z')$) and its branching ratios to all considered channels, the version Z'-explorer-BR of the program would provide the same output as Z'-explorer , but requiring the following per-line information for `/incard/card_1.dat`:

$$M_{Z'} \quad \sigma(Z') \quad \mathrm{BR}(jj) \quad \mathrm{BR}(bb) \quad \mathrm{BR}(tt) \quad \mathrm{BR}(ee) \quad \mathrm{BR}(\mu\mu) \quad \mathrm{BR}(\tau\tau) \quad \mathrm{BR}(inv) \quad \mathrm{BR}(WW) \quad \mathrm{BR}(Zh) \quad \mathrm{BR}(xx)$$

In this case, the program cannot compute the Z' width, therefore the user should run it while being cautiously to satisfy the narrow-width approximation ($\Gamma_{Z'} \ll M_{Z'}$). Usually a width of less than 5% of $M_{Z'}$ is enough.

Once again in the main directory, we run the program by typing in the command line

```
>./program.out
```

A summary of the tasks performed by Z'-explorer will be displayed on the screen. Since there is no limit in the number of points that can be explored in parameter space, there is no limit in the number of rows of `/incard/card_1.dat`. The running time depends of course on the latter, but one of the main goals of Z'-explorer is that it runs very fast and using negligible CPU resources (since there are no Montecarlo simulations during the performance). Typically, for $\mathcal{O}(10^3)$ points the performance lasts no more than two seconds on an ordinary laptop.

The generated output file is saved as `/output/1.dat`. It contains the incard information for each benchmark point (to ease the subsequent processing and analysis of the outcome), followed by

$$\mathcal{S}_{jj} \quad \mathcal{S}_{bb} \quad \mathcal{S}_{tt} \quad \mathcal{S}_{ee} \quad \mathcal{S}_{\mu\mu} \quad \mathcal{S}_{\tau\tau} \quad \mathcal{S}_{inv} \quad \mathcal{S}_{WW} \quad \mathcal{S}_{Zh} \quad \mathcal{S}_{xx} \quad \Gamma_{Z'} \quad \text{WARNING}: \Gamma_{Z'} > 5$$

where $\mathcal{S}$ is the calculated strength in each channel, $\Gamma_{Z'}$ is the total Z' total width, and the last column is a warning for when the input parameters invalidate the narrow width approximation (displays 1 if $\Gamma_{Z'} > 5\%$ and 0 otherwise). $\mathcal{S}_{xx}$ can be considered as a dummy variable to eventually add new possible Z' channels. Since each row in the input file is a different point in the parameter space for Z'-explorer , the output file has the same length as `/incard/card_1.dat`.

Additionally, in the `/extra/` folder and in different files generated after running, are available the estimated decay widths, branching ratios, the estimated σ_{pred} and the extracted σ_{lim} for each benchmark point in the incard. Details on these auxiliary files can be found in the `README` file inside the main directory.

4.3 *Z'*-explorer: Backend

For each signal point, and extracting the couplings provided in the input file, Z'-explorer computes the decay widths to all SM-fermions using the analytic formulas in (2.22), (2.23) and (2.24). Extracting also the partial widths for diboson final states and neutrinos, Z'-explorer calculates the branching ratios to all channels included in this first release of the software, which are jj, $b\bar{b}$, $t\bar{t}$, e^+e^-, $\mu^+\mu^-$, $\tau^+\tau^-$, $\nu\bar{\nu}$ (in here, dubbed invisible), W^+W^- and Zh. The total production cross-section for each $M_{Z'}$ is obtained from previously generated and recorded production cross sections with `MadGraph5_aMC@NLO`[138], which are stored in the repository as simulation cards (`sim_cards`). The details of their building, structure, and processing can be found in 4.3.1. The previous steps are skipped by Z'-explorer-BR, since branching ratios and production cross section are directly taken from the incard.

The next task performed by Z'-explorer (and Z'-explorer-BR) is the product between the branching ratios and the total production cross-section to have the total cross-section corresponding to each channel (σ_{pred}), within the NWA. Once this is obtained, the predictions for each possible final state are compared to the corresponding 95% CL upper limit on the product of the cross-section times branching fraction (σ_{lim}), coming from the most sensitive searches performed both by the ATLAS and CMS Collaborations. The comparison is made through the calculus of the aforementioned strength ($\mathcal{S}$), explained in Section 4.1. The experimental data is available in the so-called experimental cards (`exp_cards`). In 4.3.2 we discuss the extraction, use, and other details about the experimental data.

4.3.1 Simulations Cards

Simulation cards are one of the key ingredients to estimate the production cross-section for a given Z', without performing Montecarlo simulations during Z'-explorer execution. It is straightforward that for the alternative version, Z'-explorer-BR, simulation cards are not available since the production cross-section is directly extracted from incard. As mentioned before, Z'-explorer uses previously generated and recorded production cross sections with `MadGraph5_aMC@NLO` with a tailored Z' model which couples with unity to only one quark in the proton each time. In other words, considering valence and sea quarks in the proton, we generated five different processes

$$q\bar{q} \to Z'$$

for $q = u, d, s, c, b$, with the corresponding $g_{q_L} = g_{q_R} = 1$ (and all the other coupling set to 0). Since LHC protons are unpolarized we set the same couplings for left and right chiralities at this level. The UFO-model was generated with `FeynRules` package [139], is public available in [137] (download `/extra-Zprime/` directory), and ready to be implemented. For generation, taking for example $q = u$, the on-line command used in the `MadGraph5_aMC@NLO` shell is:

```
MG5_aMC> generate u u~ > Zp
```

After matrix level generation, we launched 10K events for each process and for a set of $M_{Z'}$ values between 0.4 and 8.1 TeV, with a step of 0.01 TeV, and at $\sqrt{s}$ = 13 TeV, to get the cross-section of each production process for each $M_{Z'}$. We perform this calculation at LO using the default tunning in `MadGraph5_aMC@NLO`, namely the `nn23lo1` PDF set, and the factorization and renormalization scales set to the Z' mass (i.e., using the default `run_card.dat`). If the user requires an analysis which includes uncertainties coming from the proton PDF, the mentioned scales and/or other collider and run settings, in Appendix D is explained how to get new simulation cards changing these elections, for accordingly exploring possible systematics uncertainties from this sources.

These calculus are stored as the default simulation cards for Z'-explorer in the local `/cards/` directory, one for each q in the proton (see Table 4.1 for references). Simulation cards are text files (with two colums, the first with the $M_{Z'}$ [TeV] and the second one with the corresponding cross section [pb]) and are used during program execution: the predicted production cross section for a specific benchmark point set by user is the sum of the five contributions of quarks (u, d, c, s and b), each of them adjusted by the sum of the corresponding squared chiral couplings, that are extracted from the incard. That is

$$\sigma(Z') = \sigma(pp \to Z') = \sum_q \sigma_{q\bar{q}->Z'}^{g_{q_L}=g_{q_R}=1} \left[(g_{q_L})^2 + (g_{q_R})^2 \right] \tag{4.2}$$

where g_{q_L} and g_{q_R} are the couplings of Z' to q_L and q_R respectively and $\sigma(Z')$ is the total production cross section. The software selects inside the simulations the record with the mass $M_{Z'}$ that is closest to the one in the input file at the corresponding working point (the resolution is 0.01 TeV). The total production cross-section is then used in each possible decay channel to compute the σ_{pred} as explained before.

#	Process
1	$u\bar{u} \to Z'$
2	$d\bar{d} \to Z'$
3	$c\bar{c} \to Z'$
4	$s\bar{s} \to Z'$
5	$b\bar{b} \to Z'$

TABLE 4.1. Numbering scheme of simulation cards. Saved in the main directory as `/cards/sim_card_#.dat`

4.3.2 Experimental Cards

The experimental limits used by Z'-explorer , corresponding to the value of σ_{lim} required in Eq. (4.1), are stored as experimental cards in the `/cards/` local directory. The searches included, performed by the ATLAS and CMS Collaborations and considering the latest and most sensitive results to the release date of the software, include all posible visible channels at $\sqrt{s} = 13$ TeV: jj [116], $b\bar{b}$ [119], $t\bar{t}$ [120], e^+e^- [122], $\mu^+\mu^-$ [122], $\tau^+\tau^-$ [125], W^+W^- [127], Zh [128]. Unfortunately, not all these searches are at the same luminosity, most of them are at 36 fb^{-1}, but for jj, e^+e^-, $\mu^+\mu^-$ we could included the limits at 139 fb^{-1} since these searches were already published. Another point to take into account is that the range of the limits in the $M_{Z'}$ axis vary from one search to another, and of course this is reflected in the results Z'-explorer produces. For example, while the jj final state[116] constraints $M_{Z'}$ between 1.1-7 TeV, the e^+e^- or $\mu^+\mu^-$ search [122] bounds $M_{Z'}$ between 0.2-5 TeV.

We extracted the expected 95% CL upper limits on the product of the cross-section and the branching fraction versus $M_{Z'}$ from the tables available in `HEPData`[140]. If for a given final state this was not possible (because data was not available), we used `EasyNData`[141] for the digitization of the numerical values of the expected limits from the corresponding published plots. `EasyNData` is a simple and very useful tool to extract data from plots, where calibration and extraction are done with the cursor. In both cases, since Z'-explorer selects inside the experimental card the record with the mass $M_{Z'}$ that is closest to the one in the input file at a given signal point, we performed an interpolation of the extracted data with `Mathematica`[142], to add more points to the ones that we already had and get the experimental limits with a resolution in the $M_{Z'}$ axis of at least $\mathcal{O}(10^{-2})$ (just like simulation cards describe in 4.3.1).

We saved all this information in the experimental cards, which are also text files (with two columns, the first with the $M_{Z'}$ [TeV] and the second one with the corresponding limit [pb]). There is one for each possible decay channel (see Table 4.2 for references). It is worth noticing that since searches are constantly updated, the user can modify the experimental limits for a given channel just by modifying the corresponding experimental card, expressing magnitudes in the corresponding units, and being cautiously about the step between the masses of each point in the card (to avoid resolution problems at the moment of extracting limits).

#	Decay channel
1	jj
2	$b\bar{b}$
3	$t\bar{t}$
4	e^+e^-
5	$\mu^+\mu^-$
6	$\tau^+\tau^-$
7	W^+W^-
8	Zh

TABLE 4.2. Numbering scheme of experimental cards. Saved in the main directory as `/cards/exp_card_#.dat`

4.4 Application example #1: testing Z'-explorer on the SSM

As a first example to test the power of Z'-explorer software, we present an analysis for the Sequential Standard Model (SSM) [143], conceived as one of the simplest scenarios since the Z' boson is considered a copy of the SM Z boson. Within the SSM, the couplings of the Z' boson to all SM fermions are equal to those of the Z boson, but the trilinear coupling $Z'WW$ is absent. The SSM is a reference model in experimental searches for its simplicity, and we use it as validation for our software.

In Fig. 4.1 we present the strength $\mathcal{S}$ to all the fermion decay channels included in Z'-explorer in terms of $M_{Z'_{\rm SSM}}$. The comparison of the sensitivities between the different experimental analyses is straightforward. Since couplings are not suppressed for light fermions, as it can be expected the dimuon and dielectron channels are the most sensitive (for a given $M_{Z'_{\rm SSM}}$, they have always the higher values of $\mathcal{S}$). Comparing these two lepton channels, since experimental efficiency is slightly better for muon than electrons, there is more sensitivity in the dimuon decay channel as expected. In particular, these results match those obtained by CMS [122]. While the CMS Collaboration obtains a 95% CL expected lower limit on the mass of $Z'_{\rm SSM}$ of 4.72 TeV for the e^+e^- channel and 4.90 TeV for the $\mu^+\mu^-$ channel (assuming a width of 3% of the resonance mass), we obtain 4.89 and 5.05 TeV respectively (applying narrow-width approximation), so differences in the limits are less of 3.5%, which are perfectly acceptable considering our procedure.

Another general feature that can be seen directly from Fig. 4.1(a) is the different range in the $M_{Z'}$ axis that constraints each experimental search, as previously mentioned in 4.3.2. From Fig. 4.1(b)

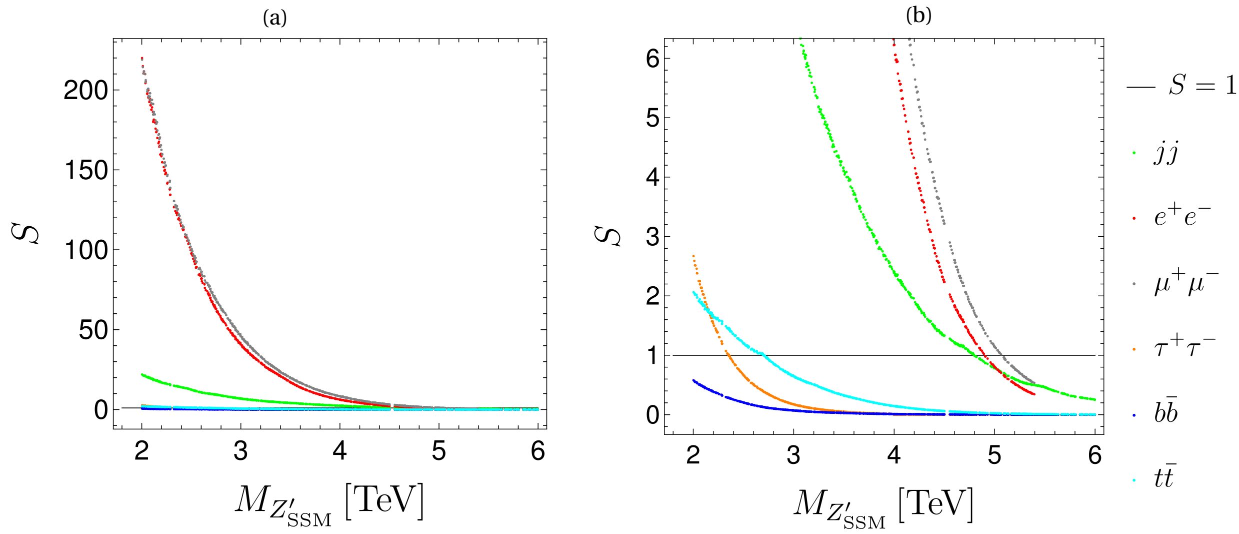

FIGURE 4.1. Strength ($\mathcal{S}$) for each fermionic decay channel included in Z'-explorer for a Z' within the SSM ($Z'_{\rm SSM}$). Full range (a) and zoom (b). Experimental limits used by the program are the aforementioned in 4.3.2. The line corresponding to $\mathcal{S} = 1$ delimits the excluded region. $M_{Z'_{\rm SSM}} \lesssim 5$ TeV are experimentally excluded.

it is interesting to notice how the $t\bar{t}$ channel passes in strength the $\tau^+\tau^-$ channel $M_{Z'_{\rm SSM}} \gtrsim 2$ TeV. The reason behind this is the well-known developed experimental techniques for boosted top tagging [123]. Another interesting feature to be observed is how the dijet channel strength falls slower than dilepton channels for larger Z' masses, even surpassing the dielectron channel above 5 TeV. This could be associated with the background: the dijet background is mostly related to the gluon PDF in the proton, whereas the dilepton background is to the quark content in the proton PDF, and is well known that valence quarks are more likely than gluons at large x. These kinds of features show some aspects of all the information condensed in the strength $\mathcal{S}$.

Additionally, we also carried out Z'-explorer validation using alternatively the ATLAS results using an integrated luminosity of 139 fb^{-1} for the dilepton search [124], where the information for both the e^+e^- and $\mu^+\mu^-$ is combined in the same channel. Once again, we reobtained the corresponding limit for the SSM ($M_{Z'_{\rm SSM}} \lesssim 5$ TeV are also excluded in this search).

4.5 Application example #2: exploring a *B-L* model

Along this section, we implement Z'-explorer for the sensitivity analysis of the search at the LHC of a Z' coming the minimal $U'(1)$ extension of the SM, associated to the $B-L$ number, presented in Section 2.6. The main goal with this concrete simplified example is to illustrate the software functioning and scope, showing the power of the tool to explore parameter space and to set constraints.

From Section 2.6 we know that $M_{Z'}$ and g_1' can be used as the free parameters of the model.

These parameters uniquely define the $Z - Z'$ mixing angle (θ_{B-L}), as can be seen from from Eq. (2.38) and (2.42). Using Eq. (2.46) for Z' couplings to all SM fermions and Eq. (2.48) and (2.49) for Z' partial widths to SM bosons, we provided an incard for Z'-explorer for a set of signal points corresponding to $(M_{Z'}, g_1^{'})$ pairs that do not violate LEP bounds in (2.39).

After Z'-explorer computation of the strength for all channels as a function of $M_{Z'}$ and g_1', we obtained the limits in Fig. 4.2. Signal points in black are experimentally excluded (i.e., $\mathcal{S} > 1$) by the limits of the corresponding search in each possible final state. From Fig. 4.2 we can conclude that the diboson channels and the ones related to the third generation of quarks are not sensible for Z' exclusion within our model. On the other hand, the e^+e^- and $\mu^+\mu^-$ channels exclude $M_{Z'}$ in most of the range where their searches set bounds on the product of the corresponding cross-section times branching ratio [122], unlike the dijet [116] and the $\tau^+\tau^-$ [125] final states.

Analyzing the θ_{B-L} contour levels in Fig. 4.2, we observed that the upper limit in the $|\theta_{B-L}|$ can be decreased since $\theta_{B-L} \gtrsim 5 \times 10^{-4}$ are experimentally excluded by dielectron and dimuon channels. It is interesting to notice that for lower $Z - Z'$ mixing angle, experimental searches set less stringent bounds in the parameter space as expected. This situation could be easily explained considering that small θ_{B-L} implies small g_1', and therefore the couplings of the Z' to SM fermions in Eq. (**??**) also become small.

However, setting model bounds is not the only goal of Z'-explorer . The strength reported in its output allows making a direct comparison of the sensitivity of each possible final state. For that reason, in Fig. 4.3 we present the most sensitive channel for each region of the parameter space. There is an area excluded mainly by dimuon searches for 2 TeV$\lesssim M_{Z'} \lesssim$5 TeV and 0.2$\lesssim g_1' \lesssim$0.7. It is interesting to observe that the dielectron channel is the most sensitive channel for Z' exclusion with $M_{Z'} \lesssim 2$ TeV. This is intimately related to the results in Ref. [122], which is likely to be related to experimental details in the geometry and the detector's efficiencies. In any case, the strength for dielectron and dimuon channels is very close in that region.

About the area in Fig. 4.3 where is still possible a Z' detection, for small g_1' and $M_{Z'} \lesssim 5$ TeV there is a not excluded region where dimuon is the most sensitive channel over all the other possible channels. For large masses, where there are no experimental limits for leptonic final states, the dijet channel becomes the most sensitive channel for Z' search, over the $t\bar{t}$ channel, the only channel besides jj that set bounds for $M_{Z'} > 5$ TeV [120]. This result highlights the performance of our software, which easily allows testing a given Z' model against all the available experimental searches.

4.6 Outlook: Present & Future

Along with this chapter we have presented a tool for performing simplified testings of NP Z' models against LHC experimental results for visible final states. We discuss in this section the limitations and potential improvements of this software, also comparing both released versions of the software.

A direct limitation of Z'-explorer is that for the sake of being general, its predictions are at LO

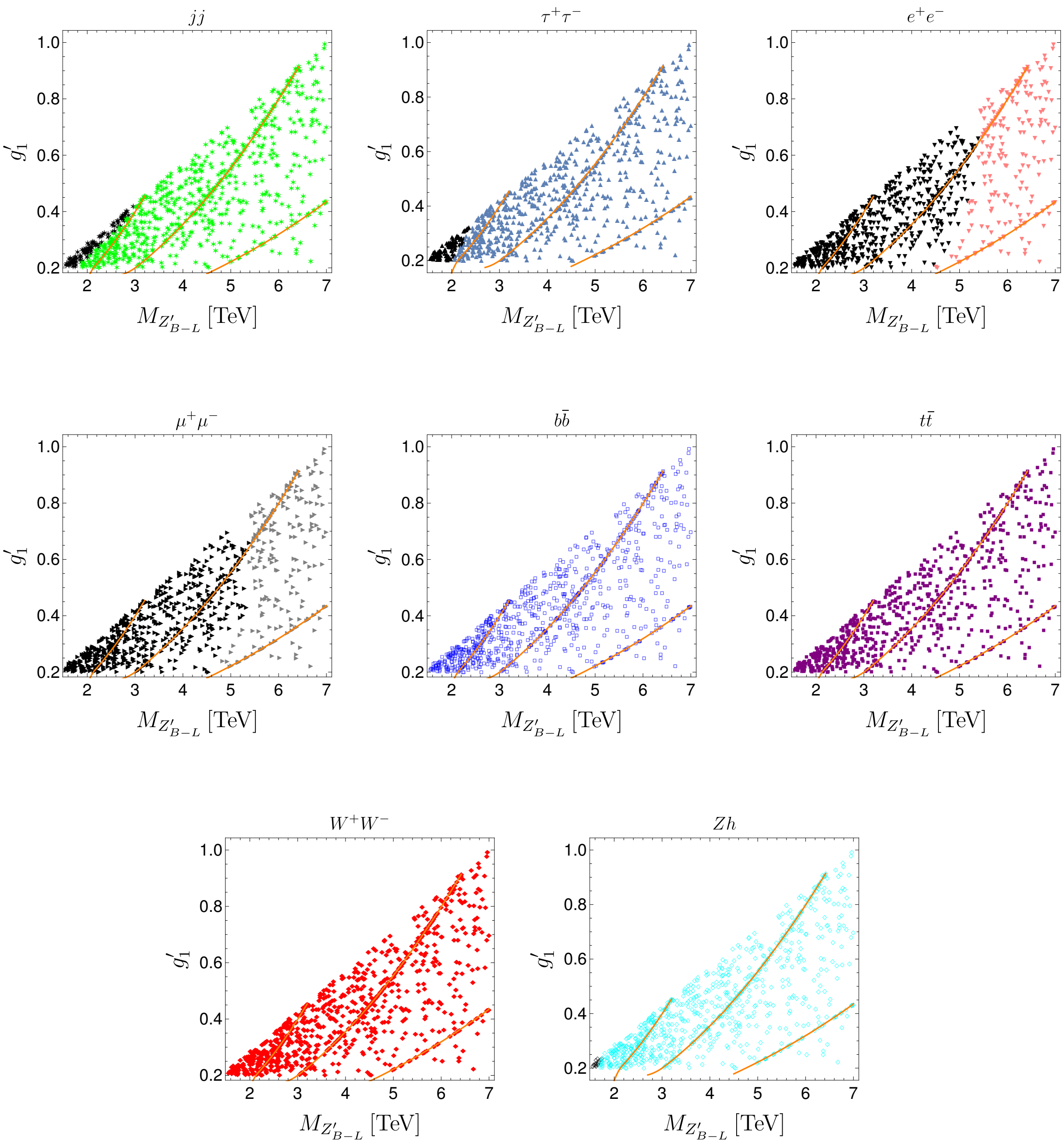

FIGURE 4.2. Bounds in each possible decay channel in the $(M_{Z'}, g_1^{'})$ parameter space, for the search of the Z' within the $B-L$ model described in Section 2.6, estimated with Z'-explorer . The points in black are experimentally excluded by the corresponding search. Experimental limits used by the software are the aforementioned in 4.3.2. The orange lines correspond from left to right to the contour levels $\theta_{B-L} = \{5\times10^{-4}, 2.5\times10^{-4}, 10^{-4}\}$, respectively.

(tree-level). NLO effect through loop-level corrections is model-dependent since it depends on the full particle content in the model. It should be noted that if users would like to include NLO effects

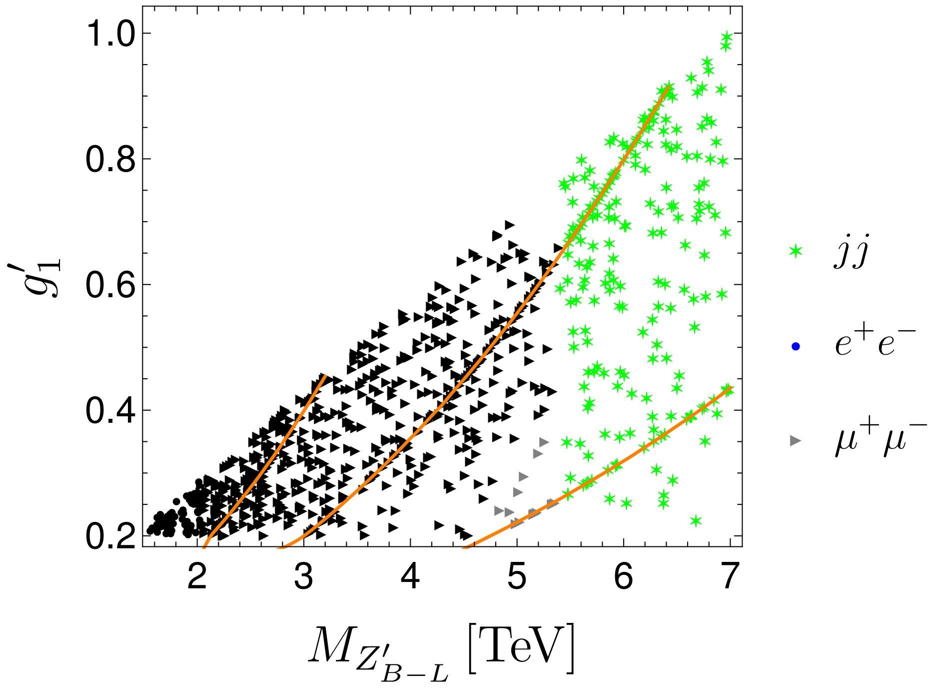

FIGURE 4.3. Most sensitive channel in each region of the $(M_{Z'}, g_1')$ parameter space for the search of the Z' within the $B-L$ model described in Section 2.6, estimated with Z'-explorer . The points in black are experimentally excluded. Both for allowed/excluded points, the most sensitive channel is determine by the shape in legends. The orange lines correspond from left to right to the contour levels $\theta_{B-L} = \{5\times10^{-4}, 2.5\times10^{-4}, 10^{-4}\}$, respectively.

while running Z'-explorer , they should provide couplings in the input file re-scaled accordingly, and analogously the partial widths. Also, they should modify the analytic formulas (2.22), (2.23) and (2.24) in source code to adapt the decay widths and branching ratios computation, as well as they should build new simulation cards (adapting instructions and files used in Appendix D for including NLO). Therefore, including NLO effects while running Z'-explorer is a cumbersome task. However, with Z'-explorer-BR alternative version, if users need to include NLO effects none of these is necessary, since they only need to compute NLO branching ratios and production cross-section for the input file. This is probably the main goal of the alternative version of Z'-explorer , beyond that its input type may be more to the liking and convenience of certain users.

On the other hand, there are interesting add-ons that would enhance Z'-explorer utility. One possibility is to schematically include low energy observables as bounds on the Z' models. Although this is a vast enterprise, it would be very appealing to have all these limits collected in easy-to-run software such as Z'-explorer . Another compelling possibility is to include dark matter searches with Z' mediators or Z' as DM candidate. The former is the main goal behind the most recent development of Z'-explorer 2.0, described in Chapter 5.

Additionally, an important add-on for Z'-explorer would be to include cross-correlations in the analysis, since it could be the case that, because of small cross-sections, a BSM signal is recognized by slight excesses in different specific channels. This proposal would also require to cross-correlate the backgrounds since in many cases different channels have the same background. We consider that this is a very attractive add-on for a Z' finder software, and it would have to be done to fully explore the available experimental data in contrast to Z' NP models.

CHAPTER 5

Z'-EXPLORER 2.0: INCLUDING DARK MATTER & TESTING Z' AGAINST INVISIBLE LHC DATA

En este capítulo presentamos la versión 2.0 de Z'-explorer, la última actualización del software, cuya principal novedad es la inclusión de búsquedas con energía faltante, siendo que la primera versión del software descrita en el Capítulo 4 únicamente incluye estados finales dentro del MS. Por lo tanto, Z'-explorer 2.0 puede probar modelos de materia oscura donde el bosón Z' actúa como un mediador de canal s entre el MS y el sector oscuro, un modelo empleado y popularizado por las colaboraciones ATLAS y CMS. Con este fin, realizamos la primera reinterpretación pública de la búsqueda más reciente de ATLAS en el canal de *mono-jet* con 139 fb $^{-1}$, detallando también las particularidades de la reobtención de límites de exclusión bidimensionales. Ilustramos el poder de nuestro código volviendo a obtener límites públicos y también mostrando resultados novedosos, donde el canal invisible agregado juega un papel importante y no puede ser ignorado. En particular, estudiamos los casos donde Z' se acopla fuertemente a los quarks top (top-fílico) y donde la materia oscura se acopla con una mezcla de acoplamientos vectoriales y axiales, destacando la utilidad de nuestro código para explorar modelos de NF con estructura de acoplamientos genérica.

In this chapter we introduce version 2.0 of Z'-explorer, the latest update of the software, which main novelty is the inclusion of missing energy searches, as the first version described in Chapter 4 only includes SM final states. Hence Z'-explorer 2.0 can test dark matter (DM) models where the Z' acts as an s-channel mediator between the SM and the dark sector, a widespread benchmark employed by the ATLAS and CMS Collaborations. To this end, we perform the first public reinterpretation of the most recent ATLAS mono-jet search with 139 fb^{-1}, also detailing the particularities of recasting two-dimensional exclusion bounds. We illustrate the power of our code by re-obtaining public plots and also showing novel results where the added invisible channel plays an important role and can not be dismissed. In particular, we study the cases where the Z' couples strongly to top quarks (top-philic) and where DM couples with a mixture of vector and axial-vector couplings, highlighting the usefulness of our code to explore NP models with generic coupling structure.

5.1 Introduction

Modern model-building requires confronting the parameter space (masses, couplings) of a NP model against a large and ever-growing variety of experimental constraints. The reinterpretation of LHC searches can then range from trivial to highly-involved to (almost) impossible. The difficulty of the task can depend on several factors, including the implicit and explicit assumptions of a given study, the degree of model independence, and the public availability of the necessary information to reproduce the reported bounds outside of the specific collaboration (e.g. experimental efficiencies). Fruitful dialogue between the phenomenological and experimental communities is already ongoing [144] which has considerably helped the public reinterpretation effort.

We can classify the re-interpretation codes into two broad categories. First and foremost, the "general" codes provide a framework where any LHC study can be implemented, and those results applied to arbitrary models, e.g. CheckMATE [132, 133], MadAnalysis5 [145, 146] and GAMBIT [147]. This flexibility on the model independence comes with the price of requiring the generation of a large number MonteCarlo events to confront a single point in parameter space with the experimental data. The second category, "dedicated" codes, narrows the applicability by focusing on a specific model framework (e.g. HiggsBounds [148] and HiggsSignals [149] for extended scalar sectors, or SModelS [150] for simplified models), which allows bypassing the CPU-time consuming event generation and thus allow a fast exploration of the parameter space. In the latter category belongs the software presented in Chapter 4, Z'-explorer, which focuses on models where the SM is augmented with a new $U'(1)$ gauge boson, dubbed Z'.

Of our particular interest is a Z' boson acting as an s-channel mediator to the dark sector, a scenario already discussed in Section 2.7. The existence of the mono-X process $pp \to Z'X \to \chi\chi X$, where $X = j, \gamma, Z, W, \ldots$ is a SM particle that must be present for the event to be triggered, requires that the Z' couples to both the SM and the DM candidate χ. This provides a robust foundation to the existing mediator search program at the LHC, encompassing both visible (i.e. SM) and invisible (dark sector) final states. Having a fast and flexible tool for the simultaneous reinterpretation of the broad palette of experimental searches is a desirable addition to the model builder's toolkit, and this is the motivation for extending the capabilities of Z' explorer to further include searches with missing energy.

To that effect, we perform the first public reinterpretation and validation of the ATLAS mono-jet study with 139 fb^{-1} of total integrated luminosity [151], which can be found in Section 5.2, which provides the most stringent constraints from the whole set of mono-X searches when X comes from initial state radiation (ISR) [152]. Our code goes beyond the public results presented by ATLAS in two directions. First and foremost, we allow for arbitrary couplings to every SM fermion. The oversimplifying assumption of having one single common quark coupling g_q and/or a single lepton coupling g_l can be dropped, revealing an interesting interplay between the visible and invisible sectors. We note that in this case, since Z'-explorer does yet not include constraints from flavor physics (which can nonetheless be easily obtained from e.g. `flavio` [153]), the user must take them separately into account. Second, we consider a general coupling structure for the $Z' - \chi - \chi$ vertex, going beyond the two benchmark setups commonly used by the experimental collaboration: the vector and axial-vector scenarios. Our results are implemented in Z'-explorer 2.0, which is publicly available on GitHub [154]. Technical details regarding the software implementation can be found in Sections 5.3 and 5.4, and in Section 5.5 are shown a series of examples showing the impact of the addition of the new channel.

5.2 ATLAS mono-jet search for Z' mediators to the dark sector

There is a large number of mono-X searches conducted by the ATLAS [151, 155–158] and CMS collaborations [159–162]. In our Z' setup, with only one mediator (Z') and one DM particle (χ), the X particle comes exclusively from ISR and it has been shown that in that case the mono-jet search trumps over all the others [152]. We focus then on the latest ATLAS mono-jet analysis at a center-of-mass energy of 13 TeV and an integrated luminosity of 139 fb^{-1} [151].[1] Nonetheless, for successful validation of this channel, we also consider an older version of the study, using 36.1 fb^{-1} [163] of total integrated luminosity since each search presents different benchmark points. Nonetheless, due to the modular nature of Z'-explorer, and the goal to keep it as flexible as possible for future updates, we plan to implement the neglected mono-X studies in a future release including more general DM sectors. In that case, final state radiation (FSR) also plays an important role, and hence there is no prior predominance of the mono-jet channel.

For signal events simulation, the Lagrangian in (2.56) coincides with that adopted by the ATLAS Collaborations, when all the leptonic couplings are set to zero, and when the Z' has either vector ($g_{f_L} = g_{f_R}$) or axial-vector ($g_{f_L} = -g_{f_R}$) couplings to the SM quarks and to the DM χ. These are the cases described in (2.51) and (2.52), which coincides with the parametrizations adopted by the Dark Matter Working Group (DMWG) [75]. The model described by Eqs. (2.51) and (2.52) has been implemented in the Universal Feynman Output [164] (UFO) format in reference [165], dubbed as `DMsimp`. Along with this chapter, we employ `MadGraph5_aMC@NLO` for event generation at the parton level, `Pythia 8` [166, 167] for showering and hadronization, and `Delphes 3.4.2` [168] for detector simulation, using the default ATLAS card. We work at leading-order (LO) accuracy in the strong coupling, which is justified since next-to-leading order QCD effects are quite mild [169]. A series of

[1] While this recast was in the final stages of completion, updated monojet results by the CMS collaboration were made public [159]. Their sensitivity to the axial-vector scenario is comparable with the ATLAS result.

sanity checks have been performed with the UFO model, and we have also verified the validity of the partial widths obtained with MadWidth [170], by numerically comparing them to those estimated from expressions in (2.53) and (2.54) (also cited by ATLAS).

Event selection criteria in the ATLAS study with 139 fb^{-1} data considers a $E_{\mathrm{T}}^{\mathrm{miss}} > 200$ GeV trigger, and requires the presence of at least one energetic jet j_1 fulfiling $p_{T,j_1} > 250$ GeV and $|\eta| < 2.4$, while up to a maximum of 4 jets with $p_T > 30$ GeV and $|\eta| < 2.8$ are allowed. Additionally, is required a separation in the azimuthal angle of $\Delta\phi(j, \vec{p}_T^{miss}) > 0.4$ (0.6) between the transverse missing momentum direction and each selected jet for events with $E_T^{miss} > 250$ GeV (200 GeV$< E_T^{miss} \leq 250$ GeV). To complete the event selection, events with leptons (e, μ, τ) or photons are vetoed.

After this event selection, the analysis is performed using two sets of signal regions: an inclusive selection (IM1, IM2, ...) and an exclusive one (EM1, EM2, ...). As their names suggest, the inclusive analysis requires $E_{\mathrm{T}}^{\mathrm{miss}}$ above a certain threshold value, while the exclusive analysis requires a specific interval. The exclusive signal regions (which are those employed by Z'-explorer 2.0), with their $E_{\mathrm{T}}^{\mathrm{miss}}$ thresholds, are detailed in Table 5.1. The previous version of this study using 36.1 fb^{-1} of total integrated luminosity uses a similar cutflow (see Table 5.2 in 5.2.1), albeit with fewer signal regions, tighter cuts on $E_{\mathrm{T}}^{\mathrm{miss}}$ and looser requirements on e, μ and no τ neither photon vetoes. Since the exclusion curves are only derived for the exclusive bins, we restrict ourselves to the EMi regions. For completeness, we also present in Table 5.1 the expected (predicted) number of SM background events in each of them.

Exclusive	EM0	EM1	EM2	EM3	EM4	EM5	EM6
E_T^{miss} [GeV]	200-250	250-300	300-350	350-400	400-500	500-600	600-700
Predicted	1783000	753000	314000	140100	101600	29200	10000
Exclusive	EM7	EM8	EM9	EM10	EM11	EM12	
E_T^{miss} [GeV]	700-800	800-900	900-1000	1000-1100	1100-1200	>1200	
Predicted	3870	1640	754	359	182	218	

TABLE 5.1. Exclusive (EM0-EM12) signal regions defined in ATLAS mono-jet search at 13 TeV and 139 fb^{-1}, together with the expected number of SM background events.

For our validation, we turned to the publicly available material. The latest study uses as a benchmark point $M_{Z'} = 2000$ GeV and $m_\chi = 1$ GeV, while the previous version employs $M_{Z'} = 1000$ GeV and $m_\chi = 400$ GeV, and a universal coupling to quarks $g_q = 0.25$, while $g_\chi = 1$. These two benchmark points represent different kinematic regimes (in the former we can neglect the effect of m_χ while in the other the dark decay is close to the threshold), and hence the combination of both provide crucial information for the proper reinterpretation.

The ATLAS study only presents results for the vector mediator and axial-vector mediator cases. ATLAS provides an official cutflow for the aforementioned benchmark point (in the 139 fb^{-1} version), and the $E_{\mathrm{T}}^{\mathrm{miss}}$ distribution for the signal benchmark and the background. The previous version of this study presents in addition to the $E_{\mathrm{T}}^{\mathrm{miss}}$ distribution (for the other benchmark point) the leading jet transverse momentum $p_T(j_1)$ distribution, which provides a welcome additional cross-check of the validation procedure.

Regarding the 95 % confidence level (CL) exclusions, ATLAS presents the results for the observed and expected upper limits (UL) on the product of the signal cross-section, acceptance and efficiency using the inclusive selection, and the 95 % CL exclusion curves (Brazilian flags) using the exclusive selection. This creates an additional difficulty for the validation, as the use of different selections between the UL and the exclusion curves prevents the derivation of the Brazilian flags from the UL, and the correlations among the different bins are not reported.

We present in Fig. 5.1 the missing energy distributions obtained for the axial-vector case by ATLAS, together with the result of our simulations. In Fig. 5.1(a) we present the 36 fb^{-1} study, while in Fig. 5.1(b) we present the results for 139 fb^{-1}. To match the published distributions, we need to include a global k-factor of 0.80 ± 0.02, whereas the older version (for the alternative benchmark point and with fewer background events, hence a larger statistical error) required 0.82 ± 0.02. We can then conclude that our event generation pipeline is validated, although as mentioned additional distributions, and potentially additional benchmark points would be a desirable addition, following also the recommendations in [144]. In passing, we note that we have also investigated the impact of jet-matching/merging together with the different options for the dynamical scale choices offered by MadGraph5_aMC@NLO. The effect is at the percent level, and as such can be ignored if we take into account that ATLAS reports 10% of uncertainty in the signal modeling and 10 % of uncertainty stemming from the parton distribution functions (PDF).

It is worth to explain that the k-factor (k) was estimated as the ratio between the total number of events of ATLAS (N^{ATLAS}) and our total number of events (N):

$$k = \frac{N^{ATLAS}}{N} = \frac{\sum_i^{N_{EMi}} N_i^{ATLAS}}{\sum_i^{N_{EMi}} N_i} \tag{5.1}$$

where N_{EMi} is the total number of exclusive bins (equal to 13 for the 139 fb^{-1} study for example, according to Table 5.1), N_i^{ATLAS} is the number of events reported by ATLAS in the given EMi region, and N_i is the number of events in EMi bin predicted by our model. For the latter we have:

$$N_i = n_i^{sim} \times L \times \sigma \tag{5.2}$$

where n_i^{sim} is the number of simulated events in EMi that passed event selection criteria, L is the corresponding luminosity and σ is the MadGraph5_aMC@NLO integrated weight. The relative uncertainty of the magnitude k is simply

$$\epsilon_k = \frac{1}{\sqrt{N^{ATLAS}}} + \frac{1}{\sqrt{n^{sim}}} \tag{5.3}$$

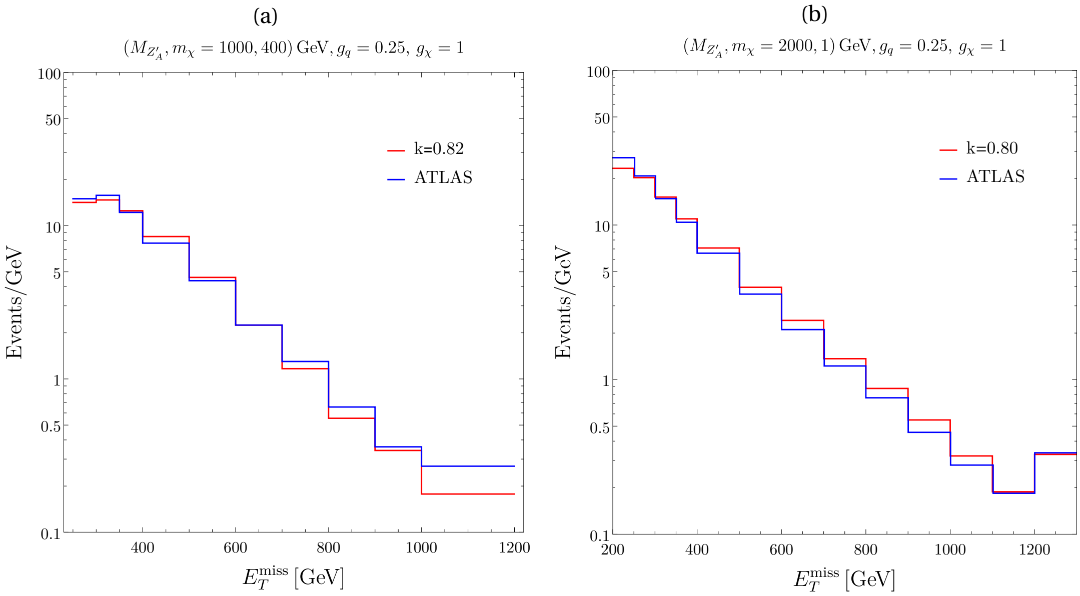

FIGURE 5.1. Missing transverse energy distributions for a signal point with $g_q = 0.25$, $g_\chi = 1$, and (a) $M_{Z'} = 1000$ GeV, $m_\chi = 400$ GeV; (b) $M_{Z'} = 2000$ GeV, $m_\chi = 1$ GeV, in the axial-vector mediator scenario. A flat k-factor of 0.82 (0.80) has been applied in the left (right) panel.

The first term of Eq. (5.3) is an upper bond at 1-sigma for the relative error coming from ATLAS events since the Collaboration does not report the uncertainty of this magnitude. We decided to use this upper limit as the total uncertainty for this magnitude, also considering that we are extracting data directly from plots with `EasyNData` (because there is no table available in `HEPData`). On the other hand, the second term is the error of our Montecarlo sample (considering negligible the uncertainty of σ).

We then proceed to derive the 95 % C.L exclusion contours for the axial mediator model, which we present in Fig. 5.2(a). We have considered here 366 points in the 2D mass plane. We display the contours where the significance (z), defined as

$$z = \frac{s_i}{\sqrt{b_i}} \tag{5.4}$$

is 2,4,6 and 8, together with the ATLAS 95 % C.L expected exclusion (dashed black line). Considering that the latter is derived from a different event selection than the former, the agreement is striking. The selection of the exclusion significance is explained in 5.2.1. We additionally provide in Fig. 5.2(b) the most sensitive EM signal region for all of our scanned points. This is an interesting plot for two reasons. First and foremost, it provides important insight on the impact of each signal region and can help to better understand the limits and suggest improvements to the search. Second, this is a relatively simple piece of information to provide, and that would be helpful as now the published table with the 95 % UL on the signal rates could be directly employed. For completeness we present the analogous of Fig. 5.2(a) for the vector mediator case, in Fig. 5.3(a). We see that the situation is completely analogous, except that the excluded regions do not fully due to the difference in cross-sections for each case.

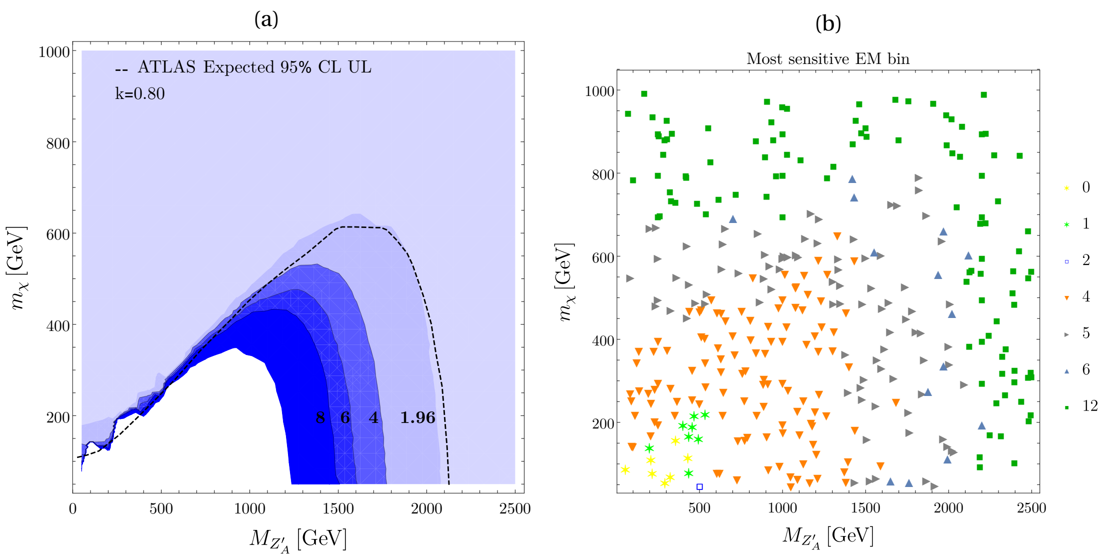

FIGURE 5.2. (a) 95 % C.L exclusion contours for the significance $z = 2, 4, 6, 8$ and the exclusive selection in Table 5.1, for an axial-vector mediator, with $g_\chi = 1$ and $g_q = 0.25$. (b) Most sensitive exclusive bin for all the reference points considered in the $M_{Z'} - m_\chi$ plane, for an axial-vector mediator with $g_\chi = 1$ and $g_q = 0.25$. In both cases the sensitivity is estimated in the Gaussian limit.

From these two figures, we then conclude that the ATLAS mono-jet search, despite lacking some detailed validation material, has been reproduced with an exceptionally good agreement, and hence we consider the implementation of this study within Z'-explorer 2.0 as validated.

5.2.1 Selection of the exclusion significance formula for the reinterpretation of the ATLAS mono-jet search

In the previous paragraphs, our main goal is the recovery of the exclusion limits reported by ATLAS in its mono-jet study with an integrated luminosity of 139 fb^{-1}, both for the vector and the axial-vector mediator cases within the exposed simplified model. Those bounds are set in the $M_{Z'} - m_\chi$ plane, with $g_q = 0.25$ and $g_\chi = 1$. In the following we explain the selection of the formula in (5.4) for the exclusion significance, focusing and providing details on the 36.1 fb^{-1} study, whose reinterpretation is used as validation of the considered channel (also it was the only search available in early stages of our analysis).

As a first approach, we tried to reobtain the 95% CL UL presented in [163], using the well known formula for the statistical significance of a counting experiment, in the limit of large number of events

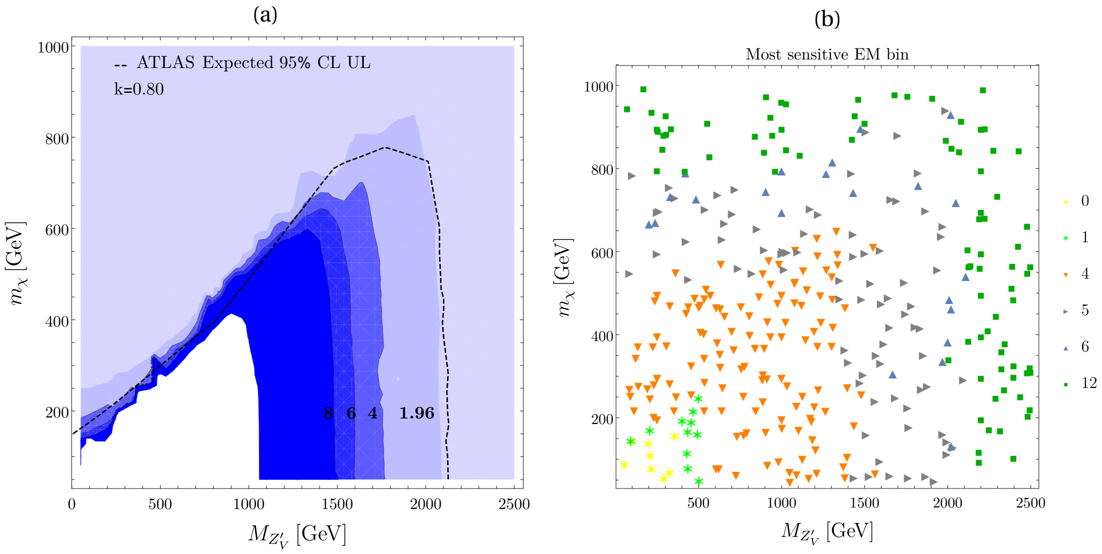

FIGURE 5.3. Same as figure 5.2, for the vector mediator case.

(normal distributed) and neglecting systematic errors

$$z_{\text{exc}} = \frac{s_i}{\sqrt{b_i}} \tag{5.5}$$

where s_i and b_i are the signal and the background respectively in the most sensitive region of E_T^{miss}. Note that significance is estimated as the number of signal events divided by the statistical uncertainty of the background. Eq. (5.5) is commonly used to determine discovery significance (background only hypothesis), but the assumption that $\sqrt{b} >> 1$ allows its use to set exclusion limits in the signal (background plus signal hypothesis) [180].

The number of background events in each exclusive bin was extracted from the ATLAS analysis (see Table 5.2). Simulations were done for 366 random benchmark points in the $M_{Z'} - m_\chi$ parameter space, with $M_{Z'} \in [50, 2500]$ TeV and $m_\chi \in [50, 1000]$ GeV. Selection cuts were applied to the 1M events obtained at simulation level, and the selected events were adjusted by the corresponding cross-section times luminosity times the k-factor equal to 0.82 ± 0.02 (explained in Section 5.2).

Results can be found in Fig. 5.4, for the vector mediator (5.4(a)) and the axial-vector mediator case (5.4(b)). We obtained a very good agreement with the expected upper limit reported by ATLAS, despite statistical and interpolation fluctuations.

On the other hand, we decided to use the exclusion significance formula in [181], which does not rely on Gaussian approximations but considers a Poisson counting experiment with negligible uncertainty

Exclusive	EM1	EM2	EM3	EM4	EM5	EM6
E_T^{miss} [GeV]	250-300	300-350	350-400	400-500	500-600	600-700
Predicted	111100	67100	33820	27640	8360	2825
Exclusive	EM7	EM8	EM9	EM10		
E_T^{miss} [GeV]	700-800	800-900	900-1000	>1000		
Predicted	1094	463	213	226		

TABLE 5.2. Exclusive (EM1-EM10) signal regions defined in ATLAS mono-jet search at 13 TeV and 36.1 fb^{-1}, together with the expected number of SM background events.

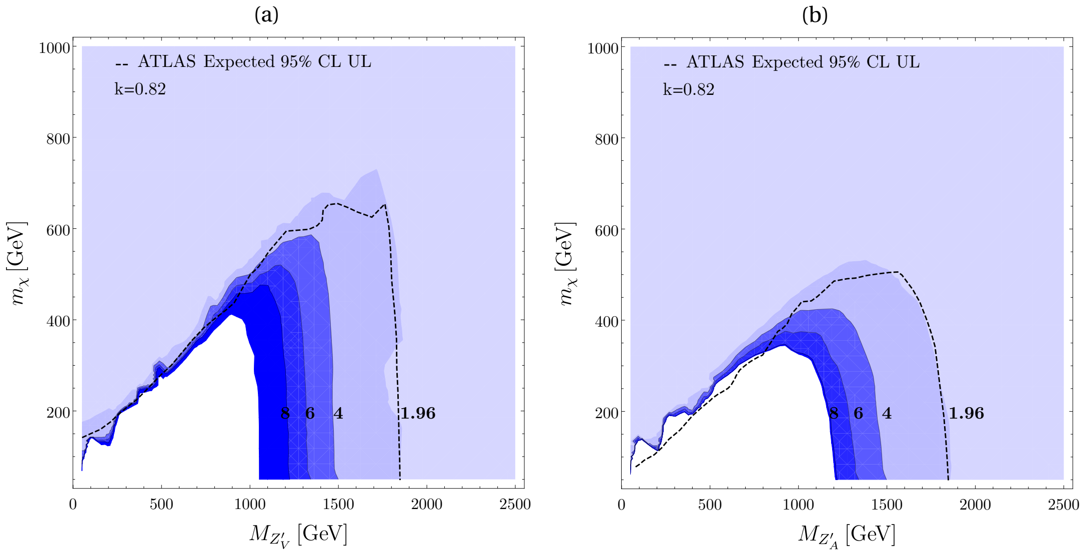

FIGURE 5.4. Exclusion contour levels using Eq. (5.5) for the significance and the exclusive selection in Table 5.2, for a vector (*a*) and an axial-vector (*b*) mediator, with $g_\chi = 1$ and $g_q = 0.25$.

$$z_{\text{exc}} = \sqrt{2\left[b_i \ln\left(\frac{b_i}{b_i + s_i}\right) + s_i\right]} \tag{5.6}$$

Expanding the logarithm in s_i/b_i one finds that the full expression reduces to the widely used Eq. (5.5), in the limit where $s_i << b_i$. Although Eq. (5.5) has been widely used in cases where $s_i + b_i$ is large, the approximation is strictly valid in the limit where $s_i << b_i$.

The contour levels obtained both for the vector and axial-vector cases are shown in Fig. 5.5. In this figure, the match of the ATLAS results is quite similar to the one obtained using Eq. (5.5) for significance, and this shows that effectively we are working in the limit where $s_i << b_i$.

The previous analysis performed for the exclusion contour lines both with Eq. (5.5) and Eq. (5.6) also probes that is not necessary to use a significance formula including systematic uncertainties. We can infer that they are negligible for the exclusion selection, even though we are not able to calculate

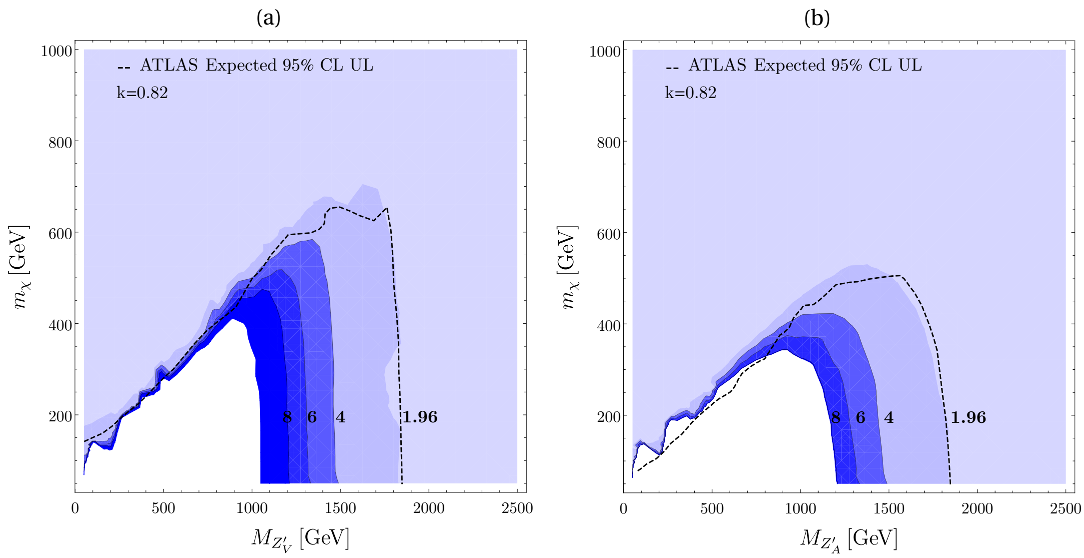

FIGURE 5.5. Exclusion contour levels using Eq. (5.6) for the significance and the exclusive selection in Table 5.2, for a vector (a) and an axial-vector(b) mediator, with $g_\chi = 1$ and $g_q = 0.25$.

them (since ATLAS only reports the numbers of signal events expected in the 95% CL UL for the inclusive selection in the model-independent approach).

For a deeper understanding of the exclusive bins, it can be found schematically in Fig. 5.6 the most sensitive exclusive bin (according to Eq. (5.6)), for all the points considered in the $M_{Z'} - m_\chi$ plane. In most of the excluded regions, the EM10 region turns out to be the most sensitive, which is the one with $E_T^{miss} > 1000$ GeV and one of the less populated bins for signal points.

To analyze why the EM10 becomes the most sensitive bin in the aforementioned area, we additionally studied the E_T^{miss} distributions for different m_χ masses, fixing $M_{Z'} = 1000$ GeV, to get a better insight of the on-shell and the off-shell behaviors of the process. In the distributions, we include all the selections cuts, except for the one in E_T^{miss} (this cut only excludes events with $E_T^{miss} < 250$ GeV). The distributions can be found in Fig. 5.7. Both for the vector and the axial-vector cases, when the Z' decay becomes off-shell ($M_{Z'} < 2m_\chi$), the E_T^{miss} distribution turns out to be harder for higher m_χ. This enhances the signal in EM10 (which includes all the events with $E_T^{miss} > 1000$ GeV), but it is insufficient to explain why it becomes the most sensitive bin over the other signal regions.

In Fig. 5.8 it can be seen instead the signal events per 100 GeV bin in E_T^{miss}, except for the last bin, that contains all the selected events with $E_T^{miss} > 1000$ GeV (the same than EM10). By including the corresponding cross-section at a given reference point (i.e., a fixed row in Figs. 5.8(a) and 5.8(b) with a given value of m_χ), signal events are suppressed for a higher value of m_χ, which is expected when the process becomes more off-shell. And even though the maximum number of events is not in the EM10 region in the off-shell case (as it can be seen in Figs. 5.7(b) and 5.7(d) for the vector and axial-vector cases respectively), this bin becomes the most sensitive. This can be explained since

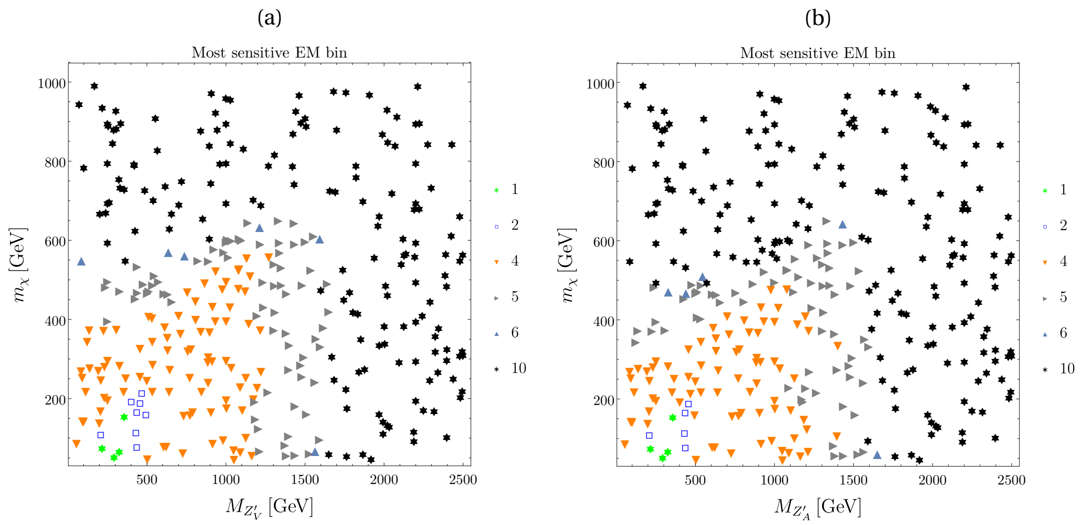

FIGURE 5.6. Most sensitive exclusive bin for all the reference points considered in the $(M_{Z'}, m_\chi)$ plane, for a vector (a) and an axial-vector (b) mediator with $g_\chi = 1$ and $g_q = 0.25$, using Eq. (5.6) for significance and the exclusive selection in Table 5.2.

there are a few events in all signal regions (as it can be seen in Fig. 5.8), and this enhances bins with a lower absolute number of background events, which is precisely the case of the EM10 region.

It is worth mention that same analysis than in Fig. 5.7 and 5.8 was performed fixing $M_{Z'} = 250$ GeV, and the conclusions are the same than those for $M_{Z'} = 1000$ GeV, as expected.

In order to understand the behavior for high values of $M_{Z'}$, we also compared the E_T^{miss} distributions for different m_χ masses, fixing $M_{Z'} = 2200$ GeV. In this area, the process is quite different, since there is no off-shell decay of the mediator in the region of the parameter space considered. Distributions can be found in Fig. 5.9. On the contrary to the previous case, E_T^{miss} distribution does not become harder at higher values of m_χ, so there is no enhancement for the signal in bins at higher energies. Once again, most of the signal events are in the EM4 region.

To explain however why EM10 becomes the most sensitive bin over the other signal regions, we have to analyze the number of events per 100 GeV bin in E_T^{miss} for this case (Fig. 5.10). Once again, even though the maximum number of events is not in the EM10 region, the few events in all signal regions favored the one with less number of background events. Another point is the fact that the maximum in the total events is an order smaller than the maximum in Fig. 5.8, which is expected as cross-sections decrease for higher values of $M_{Z'}$. Additionally, the decrease of signal events for higher m_χ is less pronounced than for low mediator masses, since the process remains in the on-shell regime.

The same contour level analysis can be performed considering the discovery significance instead of the exclusion one. There is an analogous formula to the one in Eq. (5.6), considering the Poisson counting experiment under the only-background hypothesis [182]

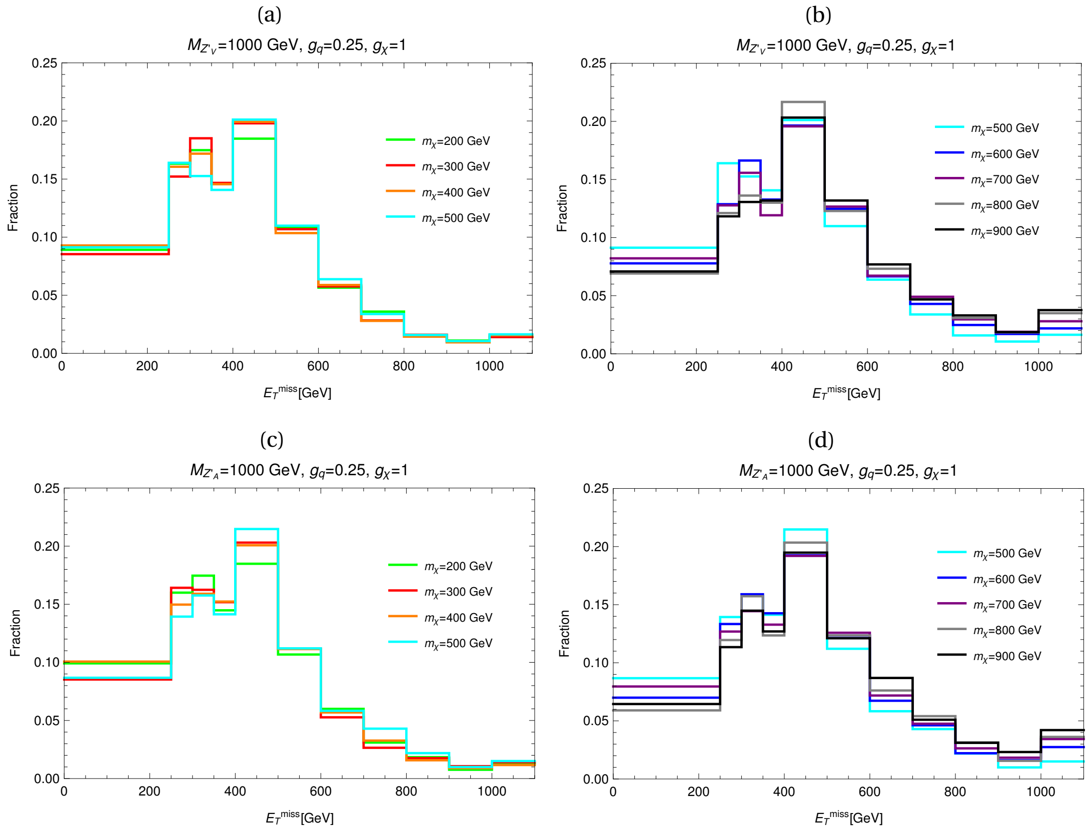

FIGURE 5.7. Missing transverse energy (E_T^{miss}) distributions for a vector on-shell (a), a vector off-shell (b), an axial-vector on-shell (c) and an axial-vector off-shell (d) mediator, with $M_{Z'} = 1000$ GeV, $g_\chi = 1$ and $g_q = 0.25$. For $E_T^{miss} > 250$ GeV, the bins correspond to the exclusive selection in Table 5.2.

$$z_{\text{dis}} = \sqrt{2\left[(b_i + s_i)\ln\left(\frac{s_i + b_i}{b_i}\right) - s_i\right]} \tag{5.7}$$

The discovery contour levels for the vector and the axial-vector mediator case using both formulas can be found in Fig. 5.11. As expected, the behavior Eq. (5.7) is equal to the one obtained with Eq. (5.6), since we are in the $s_i << b_i$ limit as demonstrated, and both formulas can be replaced by Eq. (5.5).

For a better insight of the interchange between the different significance formulas in the limit where $s_i << b_i$ within our framework, in Fig. 5.12 can be found for each selected benchmark point the error associated to use $s/\sqrt{b}$ for significance (Eq. (5.5)) instead of Eq. (5.7) for discovery (5.12(a)) or instead of Eq. (5.6) for exclusion (5.12(b)). All plots are for the axial-vector mediator case (the vector case presents identical behavior). In both cases, data is compared with the order 2 correction coming from the power expansion of the replaced formula in terms of s/b. Taking Fig. 5.12(a) as an example, the maximum difference for using the Gaussian limit instead of the Poisson formula

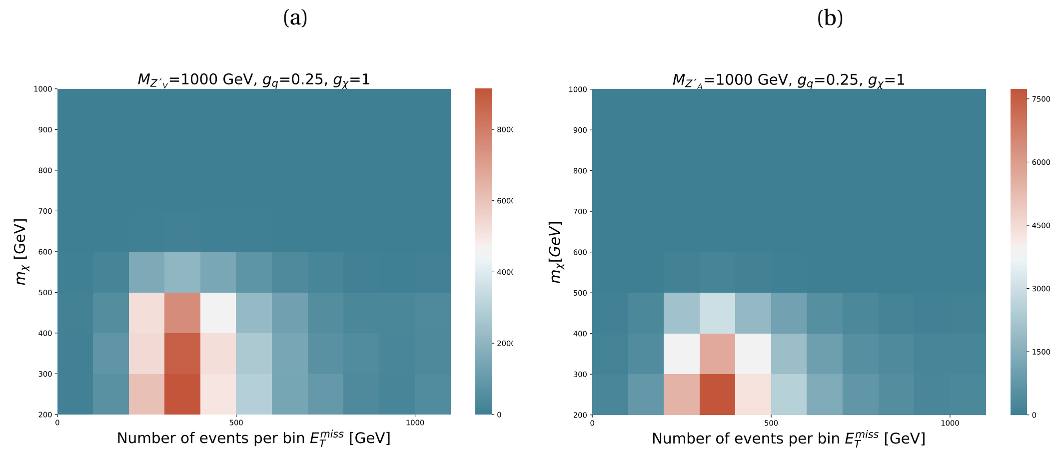

FIGURE 5.8. Signal events per 100 GeV bin in E_T^{miss}, after selection criteria (except for E_T^{miss} cut), for a vector (*a*) and an axial-vector (*b*) mediator, with $M_{Z'}$ = 1000 GeV, g_χ = 1 and g_q = 0.25. Last bin contains the same selected events than the EM10 region.

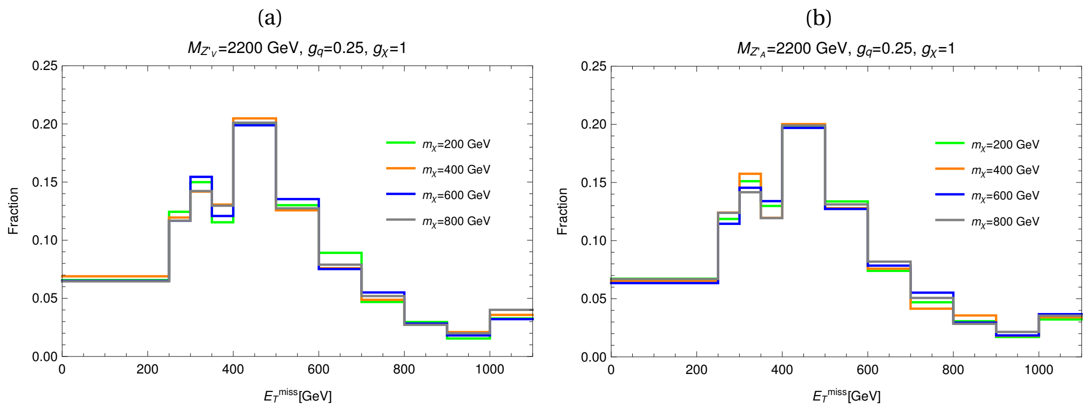

FIGURE 5.9. Missing transverse energy (E_T^{miss}) distributions for a vector (*a*) and an axial-vector (*b*) mediator, with $M_{Z'}$ = 2200 GeV, g_χ = 1 and g_q = 0.25. For E_T^{miss} > 250 GeV, the bins correspond to the exclusive selection in Table 5.2.

is less than 7%. But actually, very few points show differences with the interchange in the process considered because 95% of the points show a difference of less than 3% between the two formulas. Additionally, in Fig. 5.12(c) can be found the comparison between Eq. (5.6) and Eq. (5.7), to analyze in more detail the interchange between the discovery and the exclusion significance for the Poisson counting experiment (neglecting systematic uncertainties). The difference in using one formula from another is less than 7% in the few points where both significances are not practically equal (95% of the points show a difference of less than 3%). In all cases, the differences between formulas grow for higher values of s/b, and that explains why very few points show differences with the interchanges in the process considered.

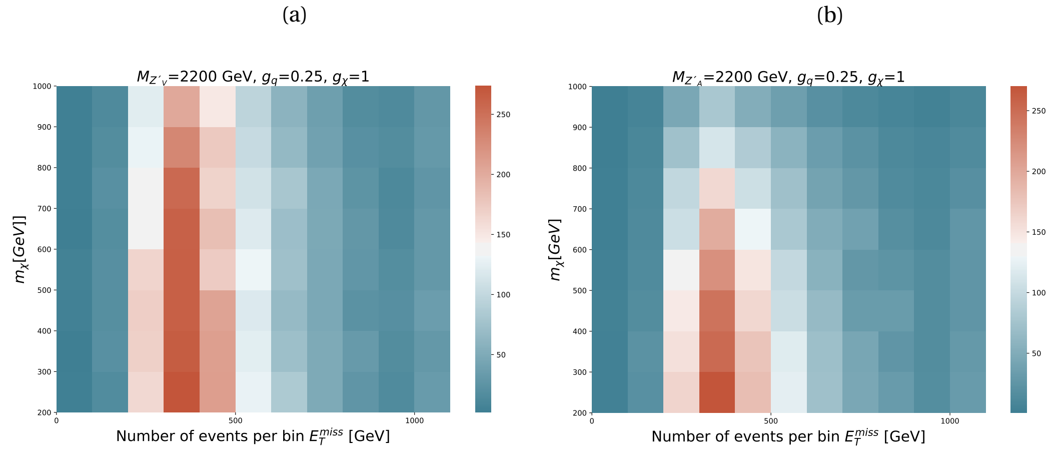

FIGURE 5.10. Signal events per 100 GeV bin in E_T^{miss}, after selection criteria (except for E_T^{miss} cut), for a vector (a) and an axial-vector (b) mediator, with $M_{Z'} = 2200$ GeV, $g_\chi = 1$ and $g_q = 0.25$. Last bin contains the same selected events than the EM10 region.

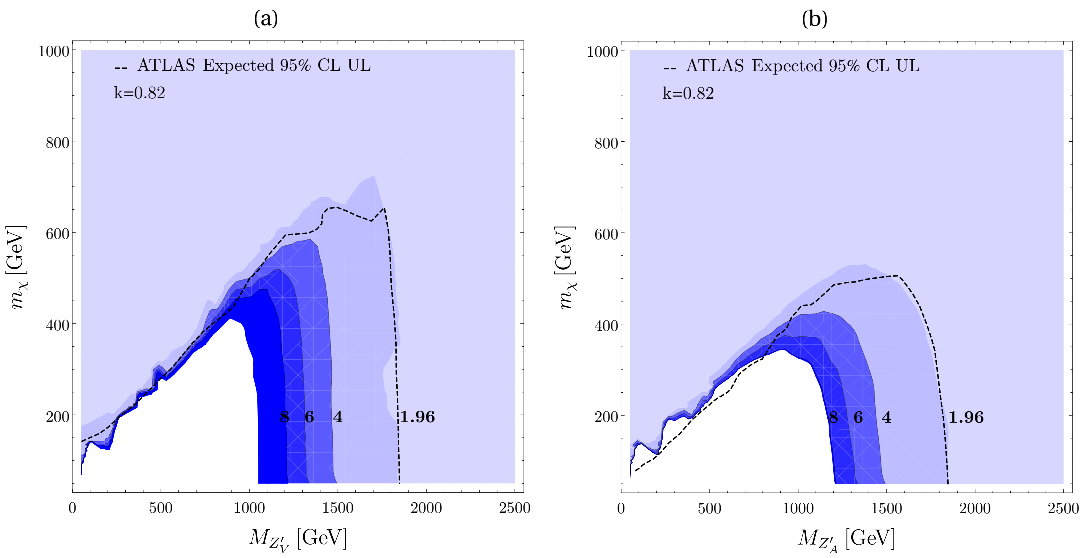

FIGURE 5.11. Discovery contour levels using Eq. (5.7) for the significance and the exclusive selection in Table 5.2, for a vector (a) and an axial-vector(b) mediator, with $g_\chi = 1$ and $g_q = 0.25$.

5.3 *Z'*-explorer 2.0: Frontend

The input card (`/incard/card_1.dat`) required by in Z'-explorer 2.0 is quite similar to the one described in Section 4.2. The user must provide the old requirements for the visible channels, plus the fermionic DM mass m_χ (in TeV) and its couplings to Z' for the new channel. The total width to other non-SM particles can be added in the computation in the old Γ_{xx}. The twenty-six NP

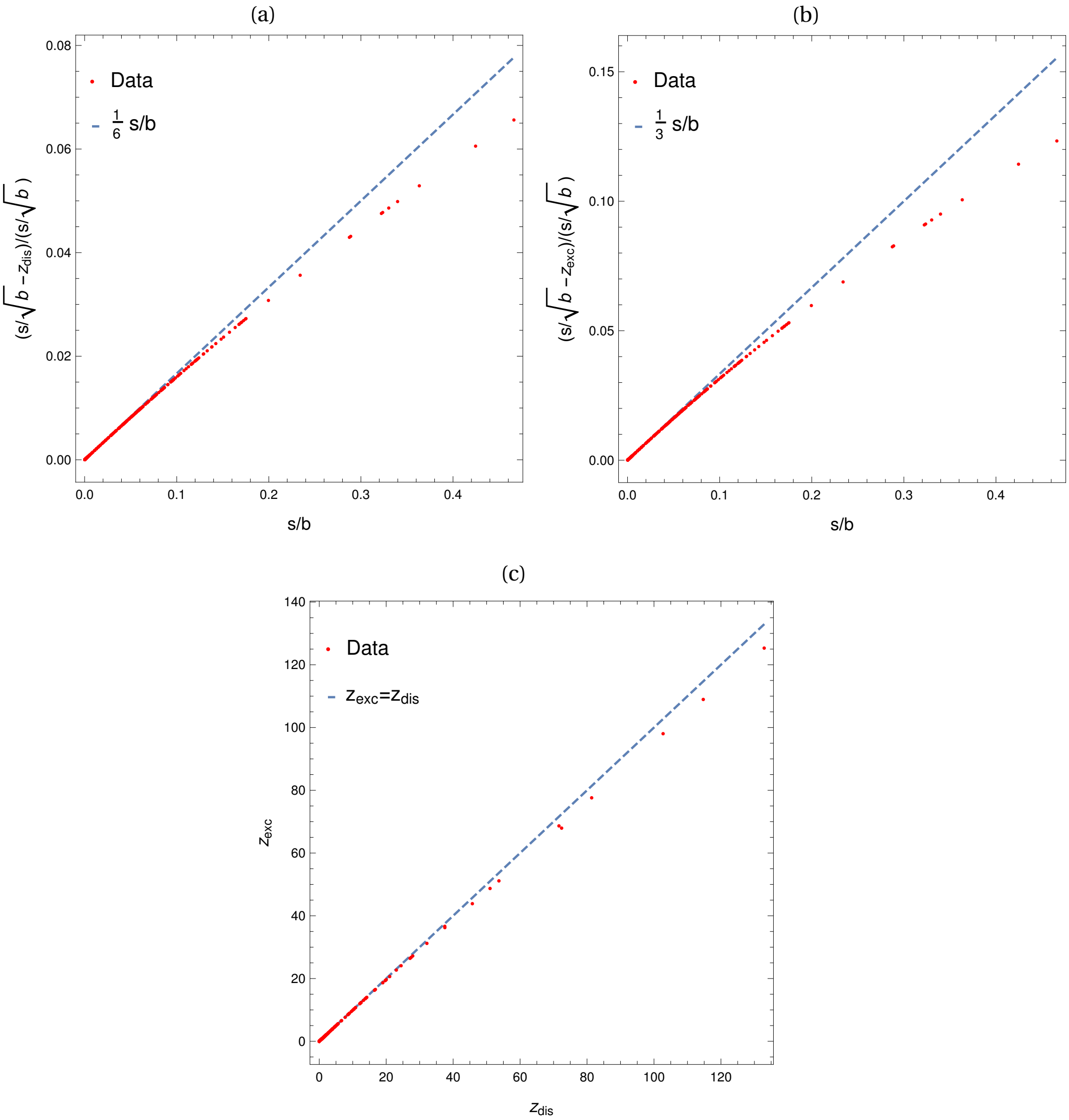

FIGURE 5.12. Difference using the different significance formulas. In (a) $z_{\rm dis}$ is the one in Eq. (5.7), in (b) $z_{\rm exc}$ is the one in Eq. (5.6), and same in (c). In (a) and (b), data is compared with the order 2 term of the power expansion of the corresponding significance in terms of s/b. The maximum value of s/b in each plot varies from one case to another, because it depends of which exclusive bin is the most sensitive one for both formulas under comparison in every point. All plots are for the exclusive selection in Table 5.2, for the axial-vector mediator case, with $g_\chi = 1$ and $g_q = 0.25$.

parameters should be specified now in the following order

$$M_{Z'}\ g_{u_L}\ g_{u_R}\ g_{d_L}\ g_{d_R}\ g_{c_L}\ g_{c_R}\ g_{s_L}\ g_{s_R}\ g_{b_L}\ g_{b_R}\ g_{t_L}\ g_{t_R}\ g_{e_L}\ g_{e_R}\ g_{\mu_L}\ g_{\mu_R}\ g_{\tau_L}\ g_{\tau_R}\ \Gamma_{vv}\ \Gamma_{WW}\ \Gamma_{Zh}\ m_\chi\ g_{\chi_L}\ g_{\chi_R}\ \Gamma_{xx}$$

Interactions between Z' and fermions must be written in the parametrization of Eq. (2.56).

The instruction for running the software remains unchanged. The addition of the new invisible channel does not significantly change the speed of the performance from the first version. The output file now returns after the incard information the following data

$$\mathcal{S}_{jj} \;\; \mathcal{S}_{bb} \;\; \mathcal{S}_{tt} \;\; \mathcal{S}_{ee} \;\; \mathcal{S}_{\mu\mu} \;\; \mathcal{S}_{\tau\tau} \;\; \mathcal{S}_{\nu\nu} \;\; \mathcal{S}_{WW} \;\; \mathcal{S}_{Zh} \;\; \mathcal{S}_{\chi\chi} \;\; \mathcal{S}_{xx} \;\; \Gamma_{Z'} \;\; \text{WARNING}:\Gamma_{Z'} > 5$$

where $\mathcal{S}_{\chi\chi}$ is the only addition from the previous version.

Also in this version, a key constituent of Z'-explorer is the narrow-width approximation (NWA), which allows to factorize the LHC processes involving Z' as a production cross section times a corresponding branching ratio in a given channel. It is then important to check if the approximation is fulfilled. In the limit where $m_{f,\chi} \lesssim M_{Z'}$ the Z' width is independent of the left- and right-handed coupling structure, reading

$$\frac{\Gamma_{Z'}}{M_{Z'}} = \frac{1}{12\pi}\left(g_\chi^2 + \sum_f N_C g_f^2\right) \tag{5.8}$$

where N_C is the number of color of each SM fermion f (3 for quarks and 1 for charged leptons). Z'-explorer does not stop the execution of the code, but prints a warning in the last column of the output if $\Gamma_{Z'}/M_{Z'} > 5\%$. For a leptophobic Z' with a single g_q coupling being equal to (4 times smaller than) g_χ, this 5 % threshold is reached for $g_q = 0.35(0.25)$, which sets a ballpark value for these couplings.

5.4 Z'-explorer 2.0: Backend

As previously described, Z'-explorer 2.0 extend the scope of the software's first version to include final states with missing transverse energy. The implementation for the SM channels remains unchanged from what is described in Section 4.3. In this version, we have modified some of the visible channels to include the most sensitive searches up to date. The updated references are: $b\bar{b}$ [116], e^+e^- [171], $\mu^+\mu^-$ [171], and W^+W^- [172]. Therefore, in this section, we focus on the implementation of the new DM final state.

Before the implementation of the new channel, we have studied several kinematical distributions (in particular the missing transverse energy, the leading jet momenta and the jet pseudorapidities) to verify that, as expected, the shape of these distributions depends only upon $M_{Z'}$ and m_χ, while being independent of all couplings. This is a crucial assumption upon which Z'-explorer relies. Some details of the verification carried out are shown in 5.4.1. The quark couplings obviously enter in the production cross section for the $pp \to Z'j$ process. We have also verified that the different quark contributions from the initial state do not interfere with each other, namely that

$$\sigma(pp \to Z'j) = \sum_{q_i} g_{q_i}^2 \left[\sigma(q_i\bar{q}_i \to Z'g) + \sigma(q_i g \to Z'q_i) + \sigma(\bar{q}_i g \to Z'\bar{q}_i)\right] \tag{5.9}$$

holds. We note that the different cross sections σ in the square brackets are not parton level matrix-elements, but they also include the corresponding convolution with the parton distribution functions (PDF). Here we assume that CP is conserved, hence the different between $q_i g$ and $\bar{q}g$ initial states is only due to the PDFs.

For the fast evaluation of these production cross-sections, we follow a procedure analogous to the one used in Z'-explorer 1.0. For the visible channels, as explained in Section 4.3, the relevant process under consideration is

$$q\bar{q} \to Z'$$

Due to the trivial scaling with the g_q couplings and the lack of interference among the different channels, it is enough to make a fine scan of $\sigma(q_i\bar{q}_i \to Z')$ in the 1-dimensional parameter space given by $M_{Z'}$. Here the task is slightly more complicated since now the different cross-sections from Eq. (5.9) must be scanned in the two-dimensional mass plane $M_{Z'} - m_\chi$. Nonetheless, this is not an obstacle, and with a fine scan of this mass plane, the cross-section of any given point can be numerically estimated with great accuracy.

To compute the production cross-section in the new decay channel, the software uses previously generated and recorded leading order (LO) cross-section of the process

$$pp \to Z'j$$

at $\sqrt{s} = 13$ TeV with `MadGraph5_aMC@NLO`, customizing the UFO-model described in Section 5.2, to set g_{q_A} (g_{q_V}) equal to 1 for only one quark in the proton each time and for $M_{Z'} \in [0.01, 2, 5]$ TeV, with a step of 0.01 TeV. We have explicitly verified that the initial states with b quarks have a negligible contribution to this process. We employ default settings of `MadGraph5_aMC@NLO`.

These cross-sections grids, stored in the repository as `/cards/AXIAL(VEC)_Zpj`, are invoked during the program execution: the predicted production cross section for a benchmark point is simply the sum of the four contributions of quarks (u, d, c and s), each of them adjusted by the sum of the corresponding squared couplings. That is

$$\sigma(pp \to Z'j) = \sum_q \left[\sigma_{pp\to Z'j}^{g_{q_A}=1}(g_{q_A})^2 + \sigma_{pp\to Z'j}^{g_{q_V}=1}(g_{q_V})^2\right] \tag{5.10}$$

Note that this expression is the analogous to the one for visible channels in (4.2). The software selects inside the simulations the record with the mass $M_{Z'}$ that is closest to the one in the input card at the corresponding benchmark point. The axial and vector couplings are directly estimated from the chiral coupling in the input card, using transformations in (2.57).

The production cross-section times branching ratio estimated for the given benchmark point are used to re-scale the experimental limits in [151] for the axial-vector mediator scenario, within the NWA.[2] Within the latter, the total cross-section can be estimated as

$$\sigma(pp \to \chi\bar{\chi}j) = \sigma(pp \to Z'j)\ \ \mathrm{BR}(Z' \to \chi\bar{\chi}) \tag{5.11}$$

with

$$\mathrm{BR}(Z' \to \chi\bar{\chi}) = \frac{\Gamma(Z'_V \to \chi\bar{\chi}) + \Gamma(Z'_A \to \chi\bar{\chi})}{\Gamma_{Z'_A} + \Gamma_{Z'_V}} \tag{5.12}$$

where $\Gamma_{Z'_V}$ and $\Gamma_{Z'_A}$ are already defined in (2.53) and (2.54), respectively. If $\Gamma_{Z'}/M_{Z'} < 5\%$, we checked that the uncertainty in the total cross-section estimation is less than 3%. The number of events in each exclusive signal region (coming from our recast previously described) are stored for the set of points in the $M_{Z'} - m_\chi$ plane previously described in Section 5.2, in different text files in `/cards/DM/AXIAL` folder. The software selects the file for the $(M_{Z'}, m_\chi)$ pair that is closest to the one in the input card at the corresponding benchmark point, through the determination of the euclidean norm. This is the main difference concerning the first version: having UL and exclusion contours in 2 dimensions instead of only one. With the corresponding events selected and properly re-scaled, the software selects the most sensitive EMi signal region comparing to the background (also stored in `/cards/DM/`) and estimates the strength for the $\chi\bar{\chi}$ channel.

5.4.1 Study of the parameter dependence in the kinematic distributions of $pp \to Z'\chi\bar{\chi}$

As we previously described, the exclusion limits reported by ATLAS are set in the $M_{Z'} - m_\chi$ plane, with $g_q = 0.25$ and $g_\chi = 1$, either for a vector or for an axial-vector mediator. In the reinterpretation shown in Section 5.2, we select a formula for the significance (see 5.2.1) to recast those bounds in each selected benchmark point. It is the goal of our software to obtain from these results the significance value but for different couplings g_q and g_χ, which are provided by the user in the input card of Z'-explorer 2.0. But before carrying out our proposal, we have made some validations to get a deeper understanding of the cinematic of the whole process, and to demonstrate the dependence of the kinematic distributions only on the $M_{Z'}$ and m_χ.

In first place, in Fig. 5.13, we show the E_T^{miss} and all jets p_T distributions (with no cuts) for two axial-mediator reference points, for different values of g_q (and all the other parameters fixed). We intended to validate that even though g_q affects directly the production cross-section of the Z' (and of course this changes the final number of events), it does not affect the cinematic of the parton

[2]The case for the vector mediator can be trivially derived from the axial one, with the procedure described in here.

level process, so the shape of the E_T^{miss} and all jets p_T distributions is not supposed to vary. As can be seen in Fig. 5.13, the distributions for the signal point with $M_{Z'_A}$ = 1000 GeV, m_χ = 400 GeV and g_χ = 1, except for negligible statistical fluctuations are the same for the three values of g_q considered (0.05, 0.25 and 0.5), as expected. Same result is obtained for the reference point with $M_{Z'_A}$ = 2000 GeV, m_χ = 800 GeV, and g_χ = 1. Distributions for the vector-mediator case are also the same except for negligible statistical differences.

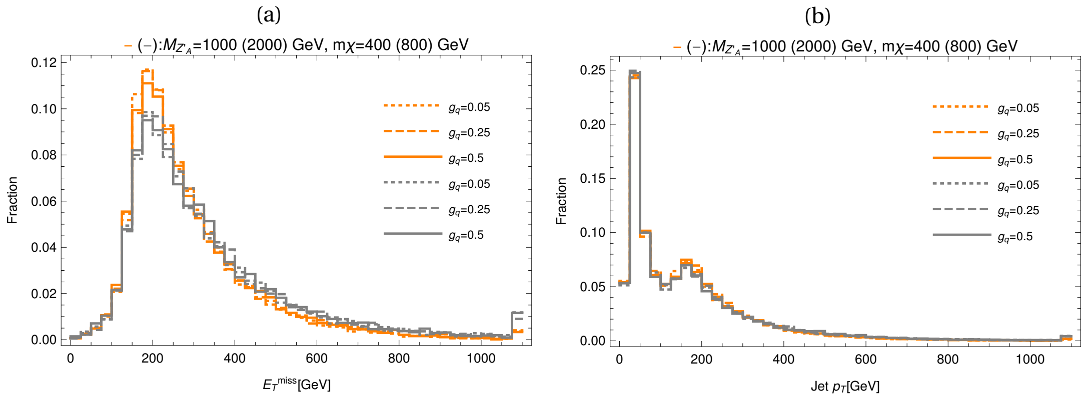

FIGURE 5.13. Missing transverse momentum (E_T^{miss}) distribution (a) and all jets p_T distribution (b) for two axial-mediator reference points with $M_{Z'_A}$ = 1000(2000) GeV, m_χ = 400(800) GeV, and g_χ = 1. Events only are required to have a maximum of 4 jets and and no leptons (e or μ). No other cuts are applied to see the full spectrum.

The same analysis can be performed varying the other parameters of the model. Focusing in the rest of the parameters, in Fig. 5.14, it can be found how the E_T^{miss} distribution of a reference point with $M_{Z'_A}$ = 1000 GeV, m_χ = 400 GeV, g_q = 0.25 and g_χ = 1 changes when modifying the type of mediator (vector) and/or the value of $M_{Z'_{A/V}}$ (a), and/or g_χ (b). For higher values of $M_{Z'_A}$, the distribution becomes harder, since the product decays of the mediator are more boosted. On the other hand, the vector and the axial-vector mediator cases present the same cinematic behavior for identical parameters, as their E_T^{miss} distributions are the same. Reducing the value of g_χ neither imprints changes in the cinematic of the process, as expected.

To finally conclude that only masses changes the cinematic of the process as expected, we also have studied the shape of E_T^{miss} in the same reference point ($M_{Z'_A}$ = 1000 GeV, m_χ = 400 GeV), but including the possibility of having both components (vector and axial-vector) simultaneously for g_q (Fig. 5.15 (a)) or for g_χ (Fig. 5.15 (b)), possibilities not considered in the ATLAS results. We also have studied the case of having only axial coupling g_q to quark/s up or/and down (and g_q = 0 for the rest of the quarks), which are expected to be the quarks more involved in the Z' production (since they are the valence quarks in proton). In none of the three cases, differences were found in the E_T^{miss} distributions beyond statistical fluctuations coming from simulations, and this is especially important since Z'-explorer 2.0 extends the ATLAS results for generic couplings g_q (not necessarily the same for

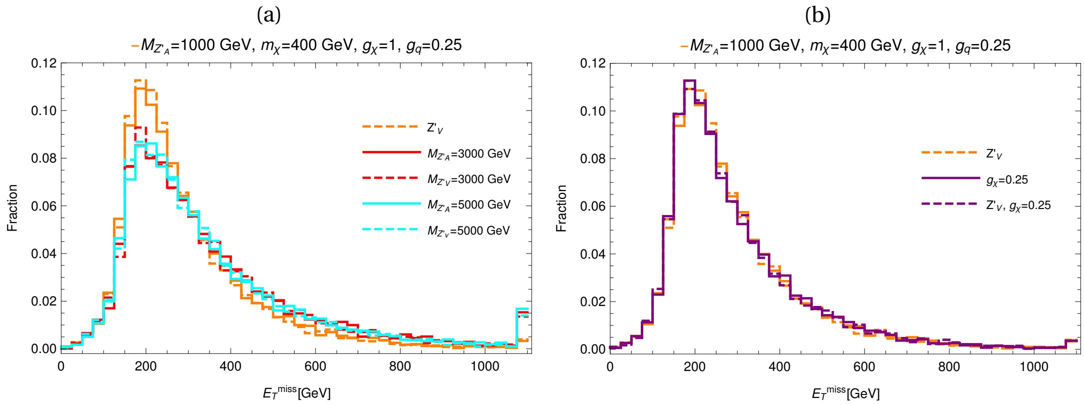

FIGURE 5.14. Missing transverse momentum (E_T^{miss}) distribution for an axial-vector mediator reference point with $M_{Z'_A} = 1000$ GeV, $m_\chi = 400$ GeV, $g_q = 0.25$ and $g_\chi = 1$, compared with the one for different type of mediator (vector) and/or value of $M_{Z'_{A/V}}$ (a), or with the one for different type of mediator (vector) and/or g_χ (b). Events only are required to have a maximum of 4 jets and and no leptons (e or μ). No other cuts are applied to see the full spectrum.

all quarks) and g_χ, allowing to have simultaneously vector and axial components according to the user requires. It is worth mention that we also checked that the fraction of events remaining after cuts does not depend on the couplings, another requirement for making the proposed re-scaling of bounds using Eq. (5.11).

5.5 Application example: Generalized DM Simplified Model

In the following, we present several plots obtained with Z'-explorer 2.0, which serve as an illustration of its capabilities. For each example, we will present the exclusions in the two-dimensional $M_{Z'} - m_\chi$ plane, where the most sensitive channel in a given point in the mass plane is indicated by its shape. If a given point is still allowed by currently expected limits then the shape is shown in a color other than black, while excluded points have a shape in black.

We focus on the simplified model described by equation (2.56), where each coupling is considered a free parameter. Within this framework, we will restrict ourselves to a few slices of the parameter space, stressing the non-trivial interplay among the different search channels, in a more generalized approach than the one adopted by ATLAS.

We start first by examining the benchmark couplings of $g_q = 0.25, g_\chi = 1, g_l = 0$ used by the ATLAS mono-jet study, and for comparison, we also include a slightly altered version with $g_\chi = 1.5$. These two leptophobic cases are shown in Fig. 5.16.

From Fig. 5.16 one sees the impact of the mono-jet search. When the DM channel is kinematically closed, the situation is relatively simple: depending on the specific mass, a hadronic channel (either jj, $b\bar{b}$ or $t\bar{t}$) provide the strongest constraints. The excluded masses range then from 0.5 to 4.5 TeV

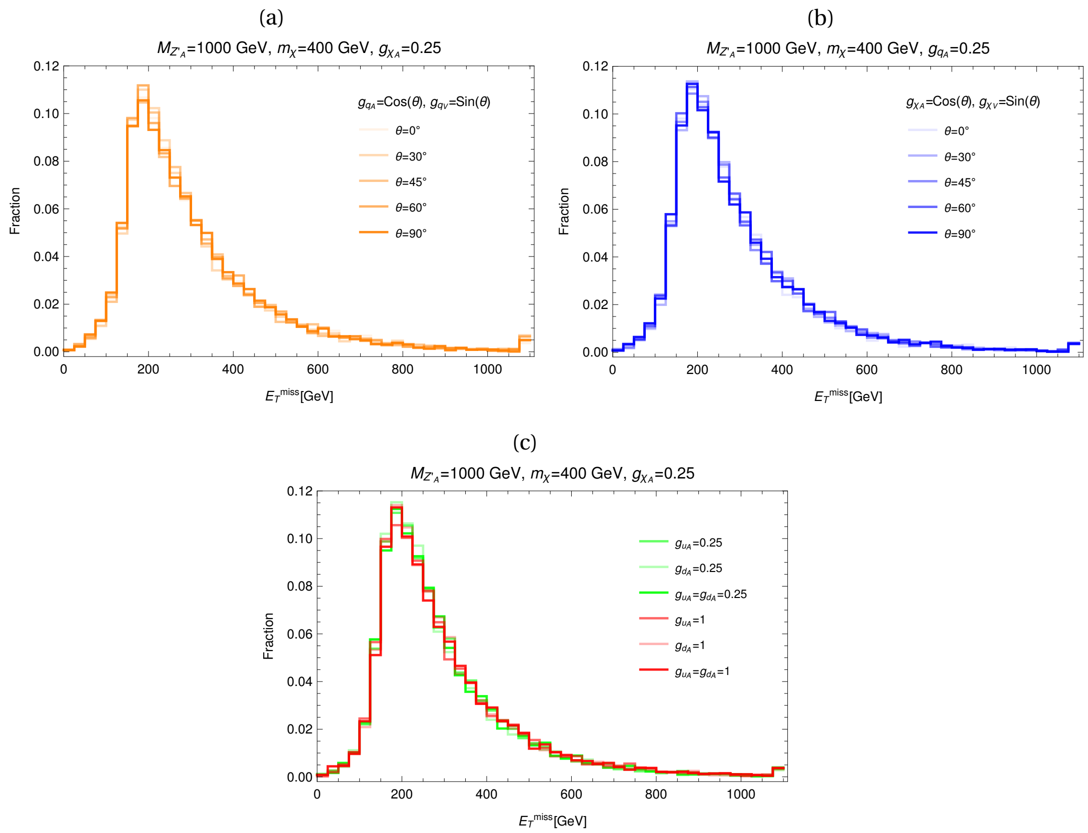

FIGURE 5.15. Missing transverse momentum (E_T^{miss}) distributions for mediator with $M_{Z'} = 1000$ GeV, $m_\chi = 400$ GeV and: (a) $g_\chi = 1$ (axial), for different values of g_q (both components, vector and axial-mediator); (b) $g_q = 1$ (axial), for different values of g_χ (both components); (c) $g_\chi = 1$ (axial), and different values of g_q (axial) for up or/and down quark/s (and $g_q = 0$ for other quarks). Events only are required to have a maximum of 4 jets and and no leptons (e or μ). No other cuts are applied to see the full spectrum.

approximately, with the upper value being due to a reduction of the production cross-section, while the lower value is because Z'-explorer only included information on the visible channels from 400 GeV. This limitation is because for lower masses, the inclusive H_T trigger is less efficient due to the overwhelming QCD multi-jet background [3]. The mono-jet channel is only relevant for the on-shell region, but as soon as it is open it dominates the exclusion, up to a value of $M_{Z'}$ of about 1 (1.5) TeV in Fig. 5.16(a) (5.16(b)). Comparing the shape of the mono-jet exclusion among both cases, we see that it is relevant for the case where g_χ dominates over g_q.

In second place we consider the case where the Z' decays almost exclusively to the top quark (top-philic Z') while still being leptophobic ($g_l = 0$). Note that a non zero g_q for u, c, d, s needs to be added in order to produce the Z' at the LHC. For simplicity and to avoid having to consider FCNC

[3] Nonetheless, there are efforts to reduce this threshold and extend the analysis into lower masses, see e.g. [173–175].

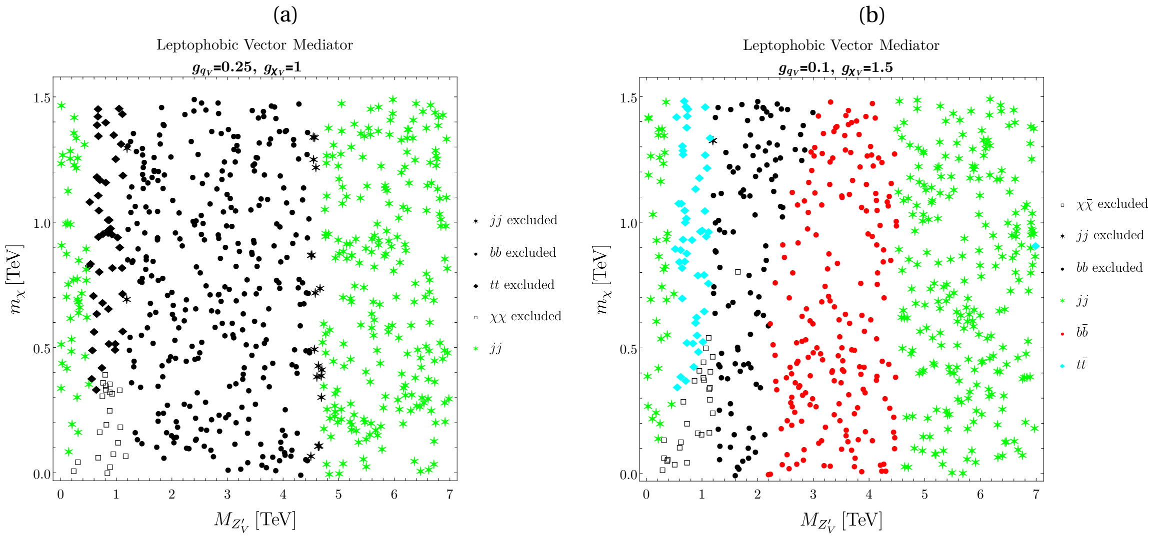

FIGURE 5.16. Excluded parameter space and most sensitive channel for the case where the DM couples with vector couplings, for two leptophobic $g_l = 0$ scenarios, fixing $g_q = 0.25$ and (a) $g_\chi = 1$; (b) $g_\chi = 1.5$. The shape of each point shows the most sensitive channel, while a black (colored) point indicates if it is excluded (allowed).

bounds, we set consider all fermions coupling vectorially, and set $g_u = 0.1$, and set $g_\chi = 1$. We present in Fig. 5.17(a) (5.17(b)) the different exclusions for a medium (small) g_t couplings: 0.25 (0.1). As

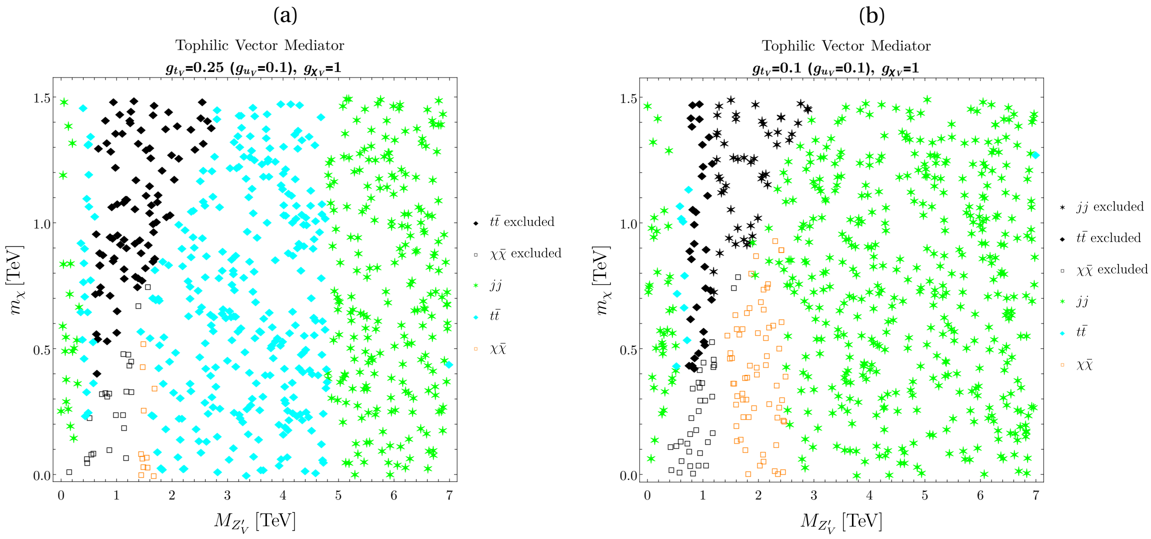

FIGURE 5.17. Excluded parameter space and most sensitive channel for the case where the DM couples with vector couplings, for two top-philic scenarios (and also leptophobic), fixing $g_u = 0.25$ and $g_\chi = 1$, and (a) $g_t = 0.25$; (b) $g_t = 0.1$.

expected, Fig. 5.17 illustrates that when the Z' couples more strongly to tops, the sensitive channels in light di-jet resonance become ineffective, and the mono-jet channel can be the most sensitive one in a large fraction of parameter space. We note that in particular, the mono-jet channel can be the most sensitive up to masses of about 2.5 TeV (obviously having the $Z' \to \chi\chi$ channel open).

For the next example, we drop the assumption of the Z' being leptophobic, and hence consider both vector and axial vector scenarios, with $g_q = 0.1$, $g_\chi = 1$ and $g_l = 0.01(0.1)$ for the vector (axial-vector) case. The results plots are shown in Fig. 5.18(a) (5.18(b)).

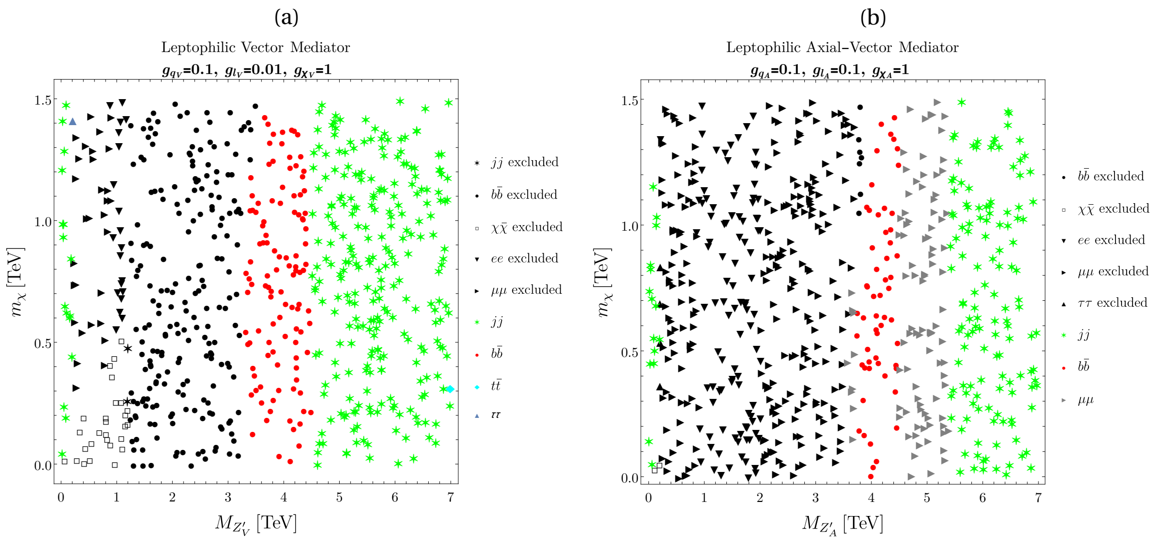

FIGURE 5.18. Same as figure 5.16 and 5.17, yet allowing for a non-zero coupling to leptons. We set $g_q = 0.1$ and $g_\chi = 1$, and show the results for (a) $g_l = 0.01$, for the vector case; (b) $g_l = 0.1$, for the axial-vector case.

From these figures, we see that the lepton channels are very sensitive, and if they are open they can dominate the exclusions. For large enough couplings the mono-jet search is much less sensitive than the di-lepton channels, except for the case where $g_l = 0.01$, where more points have mono-jet as the most sensitive probe.

Next, we examine dropping the assumption that the Z' must be either a vector or an axial-vector. We then consider a generic mixing angle among both possibilities, first for the quarks, and then for the DM χ, both in Fig. 5.19. In each figure we fix the absolute value of $g_\chi = 1$ and $g_q = 0.1$. We fix also one of the couplings in vector type, and for the other coupling, we consider three phases: 30°, 45° and 60° ($\theta = 0°$ corresponds to a pure axial-vector case, and $\theta = 90°$ to a pure vector case). What see in the figures is that the exclusions are rather similar, only presenting small variations. We thus conclude that while one can in principle be sensitive to the phase, in practical terms the variation with the angle is fairly small and can be hard to extract, from a potential signal, the θ phase.

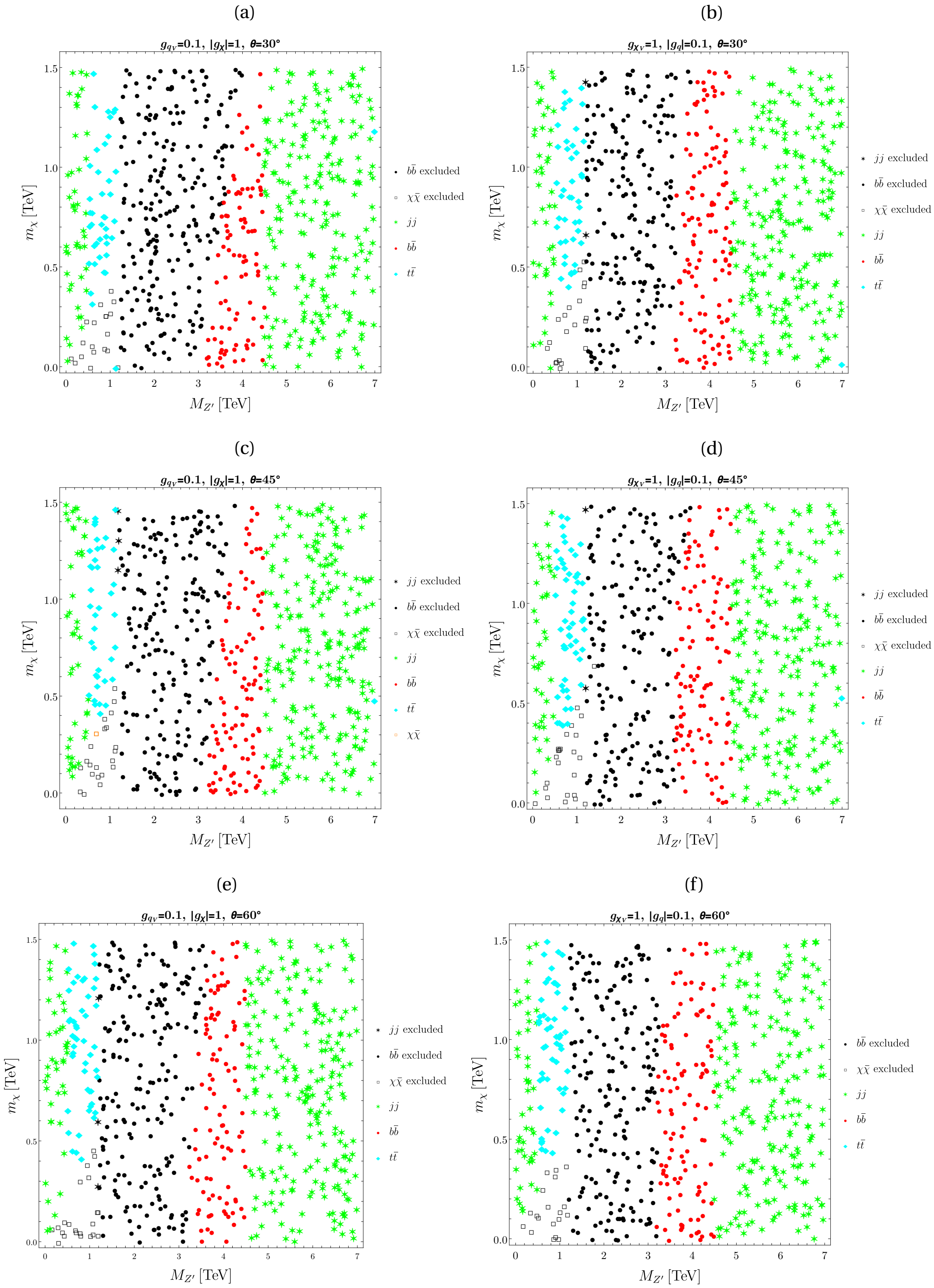

FIGURE 5.19. In the left (right), excluded parameter space and most sensitive channel for the case where the SM quarks (DM) couple (couples) with both vector and axial-vector couplings, fixing $g_{q_V} = 0.1$ and $|g_\chi| = 1$. The upper, middle and lower panels show the case where the phase θ between the vector and axial-vector case are 30°, 45° and 60°.

Capítulo 6

Conclusiones

En el marco de la búsqueda indirecta de nuevas partículas, en el Capítulo 3 hemos estudiado la fenomenología de la producción de cuatro tops en el LHC para una variedad de modelos de NF simplificados que consisten en una resonancia top-fílica, cuya masa está por debajo del umbral de la producción de $t\bar{t}$. Hemos analizado un conjunto de observables a nivel partónico y a nivel detector, y hemos estudiado cómo podrían usarse para sondear las contribuciones de NF, así como para discriminar entre ellas. Los modelos considerados, presentados en el Capítulo 2, incluyen un escalar, un pseudoescalar, un vector Z' y un gravitón. La invariancia de Lorentz en las resonancias de espín 0 requiere ambas quiralidades del quark top en la interacción, mientras que los modelos de espín 1 y espín 2 pueden configurarse para acoplarse solo a t_R, estando menos restringidos por las pruebas de precisión de $SU(2)_L$. El Lagrangiano no renormalizable del gravitón incluye un conjunto adicional de interacciones de cuatro vértices (que involucran dos quarks tops, un gravitón y un bosón de Gauge del ME), que proporciona una característica distintiva para dicho modelo.

Nuestro estudio se centra en regiones del espacio de parámetros donde la sección eficaz de producción de cuatro tops es 1.5 y 2 veces la sección eficaz esperada dentro del ME, lo que es consistente con los últimos resultados experimentales. Hemos descubierto que estas regiones son muy sensibles a las correcciones QED de orden 0 cuando se incluyen las contribuciones de NF, lo que indica que las predicciones completas al siguiente orden, incluídas las contribuciones de NF, serían un avance importante para la interpretación correcta de los resultados experimentales futuros. Hemos encontrado que las búsquedas de resonancias disponibles en $\gamma\gamma$ excluyen masas por encima de 65 GeV para los modelos de espín 0, mientras que el modelo de espín 2 permanece en gran parte sin restricciones. En el espacio de parámetros restante permitido, hemos definido algunos puntos de referencia para afrontar nuestro estudio fenomenológico.

Centrándonos en el canal de 2 leptones del mismo signo, que es una de los estados finales más sensibles de los que se miden experimentalmente, hemos estudiado la distribución de la suma escalar de los momentos transversales p_T de todas las partículas, denominada H_T, que es ampliamente utilizada en las búsquedas experimentales en el LHC. Hemos encontrado que, en comparación con el ME, los modelos de espín 0 y espín 1 predicen un espectro más suave, mientras que el modelo de espín 2 predice uno más pesado. Concluimos que tal corrimiento hacia regiones más livianas del espectro para las partículas de espín 0 y espín 1, podría pasar desapercibida por traducirse usualmente en una estimación incorrecta de la sección eficaz de la producción de cuatro tops medida. Por otro lado, el espectro más pesado de H_T en el modelo del gravitón sería una característica para discriminar este modelo.

Dadas las diferentes estructuras de Lorentz de las interacciones en cada modelo de NF, también hemos investigado la correlación de espín en la producción de cuatro tops y su impacto en las partículas del estado final. A nivel partónico, hemos estudiado la helicidad relativa de ambos quarks top definiendo una asimetría de helicidad igual/opuesta de los quarks top (ver Ec. (3.1)), comparando las predicciones del ME y de los diferentes modelos de NF considerados. Hemos encontrado contribuciones negativas a la asimetría para los modelos de espín 0 y contribuciones positivas para un Z' de gran masa y el gravitón. Para relacionar esta asimetría de helicidad con la separación azimutal entre leptones del mismo signo, $\Delta\phi(\ell^\pm,\ell^\pm)$, también hemos estudiado la separación azimutal a nivel partónico entre los quarks top del mismo signo. Hemos encontrado que la distribución $\Delta\phi(\ell^\pm,\ell^\pm)$ puede ser particularmente sensible a NF de espín 0.

Los resultados disponibles en el Capítulo 3 proporcionan en principio un conjunto de herramientas que serían útiles, no solo para detectar la presencia de NF ligera no resonante en la producción de cuatro tops, sino también para determinar la naturaleza de ésta. Encontramos que para convertir las pistas de estos observables en evidencia sólida, las búsquedas de resonancia en los canales $\gamma\gamma$ y $t\bar{t}\gamma\gamma$ serían cruciales en todos los casos, excepto para el caso de NF de espín 1. En el último caso, la corroboración podría provenir de búsquedas de resonancia que reemplacen $\gamma\gamma$ por $\gamma\gamma^* \to \gamma\ell^+\ell^-$.

En otra parte de esta tesis, centrándonos en uno de los candidatos de NF favoritos en experimentos de detección directa, en el Capítulo 4 se presenta Z'-explorer, una herramienta para probar fácilmente cualquier modelo de NF que contenga un Z' con acoplamiento a partículas del ME. La idea principal detrás de este software es extraer los límites de la sección eficaz de producción multiplicada por la fracción de decaimiento de los resultados de ATLAS y CME para cada canal de decaimiento de Z' visible, y aplicarlos sistemáticamente a un modelo de Z' dado, proporcionando una herramienta útil para el comunidad, tanto para teóricos como para experimentales.

El software solo necesita la masa del bosón Z', sus acoplamientos a los fermiones cargados del ME y los anchos de decaimiento a neutrinos, WW y Zh (o alternativamente, la sección eficaz de producción y los anchos de decaimiento para todos los canales considerados, en la versión Z'-explorer-BR), en un archivo de texto simple, donde cada fila es un punto de señal diferente dentro del modelo teórico a testear. La salida es un número positivo para cada canal, que es su *fuerza* correspondiente. Si este número es mayor que uno, el punto de señal está descartado por los límites del canal correspondiente. Además, la sensibilidad de cada posible estado final se puede comparar estudiando la fuerza: cuanto mayor es la fuerza, más sensible es el canal para descartar (u observar) el punto de señal dado en el espacio de parámetros del modelo. Dado que Z'-explorer pretende ser lo más simple posible, todos los cálculos son analíticos (dentro de la aproximación Z' con ancho de decaimiento total pequeño), sin ninguna simulación de Monte Carlo y, por lo tanto, es muy rápido: en una computadora común, puede probar $\mathcal{O}(10^3)$ puntos en unos segundos. Todo el programa es de código abierto, escrito en `C ++` y otros usuarios pueden usarlo, modificarlo y mejorarlo a través de su interfaz disponible `Github` [137].

Hemos validado Z'-explorer aplicándolo al Modelo Estándar Secuencial, reobteniendo sus límites actuales (como se observa en la Fig. 4.1). También hemos aplicado Z'-explorer al modelo $B-L$ presentado en el Capítulo 2, para mostrar explícitamente el funcionamiento y alcance del programa (ver Figs. 4.2 y 4.3), bosquejando además el trabajo requerido antes de correr el software. La discusión sobre los resultados de Z'-explorer en estos modelos de NF muestra cómo Z'-explorer condensa el lado teórico de cada modelo, junto con los aspectos experimentales para cada canal que no pueden ser ignorados al determinar sensibilidades y establecer límites, exhibiendo el poder de esta herramienta. También revisamos las ventajas, problemas y posibles mejoras de Z'-explorer, como la inclusión de la correlación entre canales, de resultados de física de bajas energías y de límites provenientes de búsquedas que involucren materia oscura. Este último es el motor principal detrás del Capítulo 5.

En el Capítulo 5 se presenta Z' explorer 2.0, la expansión del código para incluir búsquedas con energía faltante, donde Z' juega el papel de mediador entre los sectores oscuro y visible. Hemos implementado dentro del marco de Z'-explorer, la búsqueda realizada por ATLAS en el canal con un *mono-jet*, con 139 fb $^{-1}$ de datos, haciendo la primera reinterpretación pública del mismo. Hemos encontrado una buena concordancia entre nuestras simulaciones y los resultados de ATLAS (ver Figs. 5.1, 5.2 y 5.3), lo que nos permitió hacer un viaje exploratorio de varios modelos de Z'. También comentamos sobre las dificultades encontradas en la reinterpretación del estudio de mono-jet dado el material de reinterpretación disponible, así como los detalles y diferencias de la implementación de los límites de exclusión en 2 dimensiones (en vez de 1), dentro de nuestro software Z'-explorer.

Hemos estudiado la interacción no trivial entre los canales visibles y el de materia oscura, demostrándo cómo depende de las diferentes opciones de acoplamiento. Hemos adoptado un enfoque simplificado, considerando los diferentes acoplamientos de Z' como parámetros libres e independientes entre sí. Nos hemos apartado del supuesto en extremo simplificador de acoplamientos universales a quarks y leptones (adoptado en los resultados experimentales), mostrando la rica paleta de posibilidades fenomenológicas. También hemos explorado el impacto de tener un Z' con acoplamiento tanto vectorial como axial a la partícula de materia oscura, mostrando que incluso para una configuración no trivial que involucra más canales, Z'-explorer se erige como una herramienta poderosa para probar las diferentes regiones de el espacio de parámetros. Estas conclusiones resaltan además la importancia de tener un programa amplio de búsquedas experimentales, ya que ningún canal domina todo el espacio de parámetros.

Estamos en una época de experimentos sin precedentes en cuanto a precisión y sofisticación, pero, sin embargo, nos enfrentamos a una larga lista de preguntas sin respuesta sobre lo que hay más allá del ME. La comunidad de Física de Altas Energías solo ha conjeturado sobre cuáles serán los próximos grandes descubrimientos, y es en este contexto que las propuestas fenomenológicas pueden abrir caminos inexplorados hasta la fecha. Esta tesis intenta aportar propuestas de este tipo, centrándose tanto en métodos de detección indirecta, que apuntan a procesos con posible NF oculta que puede pasar desapercibida, así como en experimentos de detección directa, con resultados que deben ser tenidos en cuenta en su totalidad a la hora de imponer límites a los modelos de NF, los cuales no solo son un esfuerzo por encontrar respuestas a preguntas abiertas, sino que también orientarán a los experimentales en las próximas búsquedas que se realizarán en los próximos años en el Gran Colisionador de Hadrones de Alta Luminosidad.

Chapter 6

Conclusions

Within the indirect search of new particles framework, in Chapter 3 we have studied the phenomenology of four-top production at the LHC for a variety of simplified NP models consisting in a top-philic resonance whose mass is below the $t\bar{t}$ threshold. We have analyzed a set of observables at parton and detector level and studied how they could be used to probe NP contributions, as well as discriminate among them. The models considered, presented in Chapter 2, include a Scalar, Pseudo-scalar, vector Z', and a Graviton. Lorentz invariance in spin-0 resonances requires both top-quark chiralities in the interaction, whereas spin-1 and spin-2 models can be set to couple only to t_R, being less constrained by $SU(2)_L$ precision tests. The Graviton non-renormalizable Lagrangian includes an extra set of four-point interactions (involving two top quarks, a Graviton, and a SM gauge boson) which provides a distinguishing feature for the model.

Our study focuses on regions of parameter space where the four-top production cross-section is 1.5 and 2 times the SM-expected cross-section, which is consistent with the latest experimental results. We have found that these regions are very sensitive to tree-level QED corrections when NP contributions are included, indicating that full NLO predictions including NP contributions would be an important development for the correct interpretation of future experimental results. We have found that available $\gamma\gamma$ resonance searches exclude masses above 65 GeV for the spin-0 models, while the spin-2 model remains largely unconstrained. In the remaining allowed parameter space, we have defined some benchmark points to face our phenomenology study.

Focusing on the 2LSS channel, which is one of the most sensitive final state signatures being probed experimentally, we have studied the distribution of the scalar sum of all objects p_T, H_{T}, which is widely used by the experimental searches at the LHC. We have found that, in comparison to the SM, the spin-0 and spin-1 models predict a softer spectrum, whereas the spin-2 model predicts a harder one. We conclude that such a change in shape towards the softer spectrum region for spin-0 and spin-1 could be translated into an incorrect estimation of the measured four-top production cross-section. On the other hand, the harder $H_{\rm T}$-spectrum in the Graviton model would be a valuable discriminating feature for this model.

Given the different Lorentz structures of the interactions in each NP model, we have also investigated the spin correlation in four-top production, and its traces in the final-state particles. At the parton-level, we have studied the relative helicity of both top quarks by defining a top-quark Like/Unlike helicity asymmetry (see Eq. (3.1)) and comparing the predictions from the SM and the different NP models considered. We have found negative contributions to the asymmetry for the spin-0 models and positive contributions for a high-mass Z' and Graviton. To relate this helicity asymmetry to the azimuthal separation between same-sign leptons, $\Delta\phi(\ell^{\pm},\ell^{\pm})$, we have also studied the parton-level azimuthal separation between the same-sign top quarks. We have found that the $\Delta\phi(\ell^{\pm},\ell^{\pm})$ distribution can be particularly sensitive to spin-0 NP.

The available results in Chapter 3 provide in principle a set of tools that would be useful, not only to detect the presence of light non-resonant NP in four-top production but also to determine the nature of this NP. We find that to convert clues from these observables into hard evidence, resonance searches in the $\gamma\gamma$ and $t\bar{t}\gamma\gamma$ channels would be crucial in all cases, except for the spin-1 NP. In the latter case, the corroboration could come by resonance searches replacing $\gamma\gamma$ by $\gamma\gamma^* \to \gamma\ell^+\ell^-$.

On the other hand, focusing on one of the favorites NP candidates in direct detection experiments, in Chapter 4 is presented Z'-explorer, a tool to easily test any NP model containing a Z' boson coupling to SM particles. The main idea behind this software is to extract the bounds in production times branching ratio from the ATLAS and CMS results for each visible Z' decay channel and apply them systematically to a given Z' model, providing a useful tool to the community, both for theorists and experimentalists.

The software just needs the Z' mass, couplings to charged SM fermions and partial widths to neutrinos, WW and Zh (o alternatively the production cross-section and branching ratios to all decay channels, for Z'-explorer-BR version), in a simple text file, where each row is a different theoretical signal point to be tested. The output is a positive number for each channel, which is its corresponding strength. If this number is larger than one, the signal point is rejected by the limits in the corresponding channel. Moreover, the sensitivity of each possible visible final state may be compared by studying the strength: the larger the strength, the more sensitive is the channel to reject (or observe) the given signal point in the parameter space of the model. Since Z'-explorer is intended to be as simple as possible, all calculations are analytical (within the NWA), without any Monte Carlo simulation, and therefore is very fast: in a simple computer, it can test $\mathcal{O}(10^3)$ points in a few seconds. The whole program is open source written in `C++` and can be used, modified, and improved by other users through its `Github` interface [137].

We have validated Z'-explorer by applying it to the Sequential Standard Model (SSM), re-obtaining its currents limits (shown in Fig. 4.1). We have also applied Z'-explorer to the $B-L$ model presented in Chapter 2 to explicitly show the functioning and scope of the program (see Figs. 4.2 and 4.3), sketching the required work before running the software. The discussion of the output of Z'-explorer on these NP models has shown how Z'-explorer condenses the theoretical side of the model, with the experimental aspects for each channel that can not be ignored when determining sensitivities and setting bounds, exhibiting the power of the presented tool. We also review advantages, issues, and possible improvements to Z'-explorer, such as including correlation between channels, low-energy physics results, and Dark Matter bounds. The last is the main driver behind Chapter 5.

In Chapter 5 is presented Z' explorer 2.0, the expansion of the code to further include missing energy searches, where Z' plays the role of a mediator between the dark and visible sectors. We have implemented within the existing Z'-explorer framework, the ATLAS mono-jet study with 139 fb^{-1} of data, making the first public reinterpretation of it. We have found a good agreement between our simulations and the ATLAS results(see Figs. 5.1, 5.2 and 5.3), which allowed us to make an exploratory journey of several Z' models. In passing, we also commented on the difficulties encountered in the reinterpretation of the mono-jet study given the available reinterpretation material, as well as the details and differences of the implementing 2D exclusion bounds within our Z'-explorer framework.

We have studied the non-trivial interplay between the visible and invisible channels for DM and showed how they depend on the different coupling choices. We have taken a bottom-up approach, considering the different Z' couplings as free, independent parameters. We have departed from the simplifying assumptions of universal couplings for quarks and leptons (adopted by the experimental Collaborations), showing the rich palette of phenomenological possibilities. We have also explored the impact of the Z' coupling neither vectorially nor axially to the DM particle, showing that even for a non-trivial configuration that involves more channels Z'-explorer arises as a powerful tool to test the different regions of the parameter space. These excursions in the simplified model space highlight the importance of having a broad program of experimental searches, as no single channel dominates over the whole parameter space.

We are in an age where experiments are unprecedented in precision and sophistication, but yet we are faced with a long list of unanswered questions about what lies beyond the SM. The HEP community only has conjectured about what the next great discoveries will be, and it is in this context that phenomenological proposals can open paths unexplored up to now. This thesis attempts to provide proposals of this type, focusing both on indirect detection methods, on processes where new hidden physics can go unnoticed, as well as on direct detection experiments, with results that must be taken into account in their entirety at the time of set constraints on NP models, which are not only an effort to find answers to open questions, but also guide the experimentalists in the next searches to be carried out in the forthcoming years at the HL-LHC.

Lista de Publicaciones

La siguiente es la lista de trabajos realizados durante mi doctorado:

- E. Alvarez, A. Juste and R. M. Sandá Seoane. *Four-top as probe of light top-philic New Physics.* In *Journal of High Energy Physics* 12 (2019), 080.
  DOI: 10.1007/JHEP12(2019)080. [1910.09581]

- E. Alvarez, M. Estevez, and R. M. Sandá Seoane. *Z'-explorer: a simple tool to probe Z' models against LHC data.* In *Computer Physics Communications* 269 (2021), 108144.
  DOI: 10.1016/j.cpc.2021.108144. [2005.05194]

- V. Martín Lozano, R. M. Sandá Seoane, and J. Zurita. *Z'-explorer 2.0: reconnoitering the dark matter landscape. Aguardando publicación.* [2109.13194]

List of Publications

The following is the list of the works published during my PhD:

- E. Alvarez, A. Juste and R. M. Sandá Seoane. *Four-top as probe of light top-philic New Physics.* In *Journal of High Energy Physics* 12 (2019), 080.
  DOI: 10.1007/JHEP12(2019)080. [1910.09581]

- E. Alvarez, M. Estevez, and R. M. Sandá Seoane. *Z'-explorer: a simple tool to probe Z' models against LHC data.* In *Computer Physics Communications* 269 (2021), 108144.
  DOI: 10.1016/j.cpc.2021.108144. [2005.05194]

- V. Martín Lozano, R. M. Sandá Seoane, and J. Zurita. *Z'-explorer 2.0: reconnoitering the dark matter landscape. Awaiting publication.* [2109.13194]

APPENDIX A

Decay widths for NP simplified models in Chapter 3

We provide the decay widths of the NP Simplified models presented in Section 2.3 and used along with Chapter 3 to study NP effects in four-top phenomenology at LHC.

Scalar NP: ϕ

From Ref. [4]

$$\Gamma(\phi \to gg) = \frac{\alpha_s^2 M_\phi^3}{72\pi^3} \left| \frac{g_{\phi t}}{m_t} F(z_t) \right|^2 \tag{A.1}$$

$$\Gamma(\phi \to \gamma\gamma) = \frac{\alpha^2 M_\phi^3}{81\pi^3} \left| \frac{g_{\phi t}}{m_t} F(z_t) \right|^2 \tag{A.2}$$

where $F(z_t)$ is defined as

$$F(z_t) = \frac{3}{2} z_t \left[1 + (1 - z_t) \arcsin^2 \left(\sqrt{1/z_t} \right) \right] \tag{A.3}$$

with

$$z_t = (2m_t / M_\phi)^2 \tag{A.4}$$

We checked that the three-body decay $\phi \to W^+ b\bar{t}$ and $\phi \to W^- \bar{b} t$ (see Ref. [176] for analytic formulas) have negligible contributions for the BPs considered in Chapter 3.

Pseudo-scalar NP: A

From Ref. [4]

$$\Gamma(A \to gg) = \frac{\alpha_s^2 M_\phi^3}{72\pi^3}\left|\frac{g_{At}}{m_t}H(z_t)\right|^2 \tag{A.5}$$

$$\Gamma(A \to \gamma\gamma) = \frac{\alpha^2 M_A^3}{81\pi^3}\left|\frac{g_{At}}{m_t}H(z_t)\right|^2 \tag{A.6}$$

where $H(z_t)$ is defined as

$$H(z_t) = z_t \arcsin^2\left(\sqrt{1/z_t}\right) \tag{A.7}$$

with

$$z_t = (2m_t/M_A)^2 \tag{A.8}$$

We also checked in this case that the three-body decay $A \to W^+ b\bar{t}$ and $A \to W^- \bar{b} t$ (see Ref. [176] for analytic formulas) have negligible contributions for the BPs considered in Chapter 3.

Graviton NP: G

From Ref. [47]

$$\Gamma(G \to gg) = \frac{M_G^3}{\pi\Lambda^2}\frac{\alpha_s^2}{1440\pi^2}\left|g_{Gt}A_G(z_t,\mu_0)\right|^2 \tag{A.9}$$

$$\Gamma(G \to \gamma\gamma) = \frac{M_G^3}{\pi\Lambda^2}\frac{\alpha^2}{1620\pi^2}\left|g_{Gt}A_G(z_t,\mu_0)\right|^2 \tag{A.10}$$

with $A_G(z_t,\mu_0)$ defined as

$$\begin{aligned} A_G(z_t,\mu_0) = & -\frac{1}{12}\left\{\frac{9}{4}z_t(z_t+2)\left[2\tan^{-1}\left(\sqrt{z_t-1}\right)-\pi\right]^2\right. \\ & \left. -3(5z_t+4)\sqrt{z_t-1}\left[2\tan^{-1}\left(\sqrt{z_t-1}\right)-\pi\right]-39z_t-35-12\ln\frac{\mu_0^2}{m_t^2}\right\} \end{aligned} \tag{A.11}$$

with

$$z_t = (2m_t/M_G)^2 \tag{A.12}$$

Appendix B

Simulation details for Chapter 3

Along with Chapter 3, for the phenomenological study of the impact of light top-philic NP in four-top production at the LHC, we have used MadGraph5_aMC@NLO for matrix level generation, Pythia 8 for showering, hadronization and ISR and FSR, and Delphes 3.4.2 for detector simulation. We have used Madspin [177, 178] to decay top quarks while preserving the spin orientation. The NP models, presented in Section 2.3, have been implemented through FeynRules.

In all cases, we have included in the simulation QCD and Electroweak leading order effects. Although Electroweak corrections are a minor correction of the order ~ 5% in SM $pp \to t\bar{t}t\bar{t}$ production, it can account for up to ~ 30% for some studied NP Benchmark Points. In general, the interference is enhanced with the Electroweak particles of the same Nature as the NP. For the sake of obtaining reasonable results in a reasonable time, we have restricted the proton partons to the gluon, the valence quarks u and d, and their anti-particles $\bar{u}$ and $\bar{d}$. This approximation is converted into a difference in cross-section of about 1% and was originally suggested by the fact that most of the Feynman diagrams in four-top production are initiated through gluon-fusion, as can be seen in Fig. B.1.

The spin-0 and spin-1 NP models contain 524 Feynman diagrams to produce a four-top final state in the aforementioned conditions, whereas the spin-2 NP model requires 588 Feynman diagrams. These extra 64 diagrams are because of the 4-particle vertices needed to conserve gauge invariance in the spin-2 NP Lagrangian.

In 3.2.1 we have simulated SM and NP processes using MadGraph5_aMC@NLO in its original tune. Since it is the ratio of NP to SM what we compute, we have not required a k-factor. We have not applied cuts on the $pp \to t\bar{t}t\bar{t}$ process, whereas for the di-photon generation we have used the same cuts as the cited searches.

In Section 3.3 we have simulated tops decaying to final state using Madspin, Pythia and Delphes. All simulations are at leading order using NNPDF30_lo_as_0118 PDF and a k-factor of 1.26 is extracted

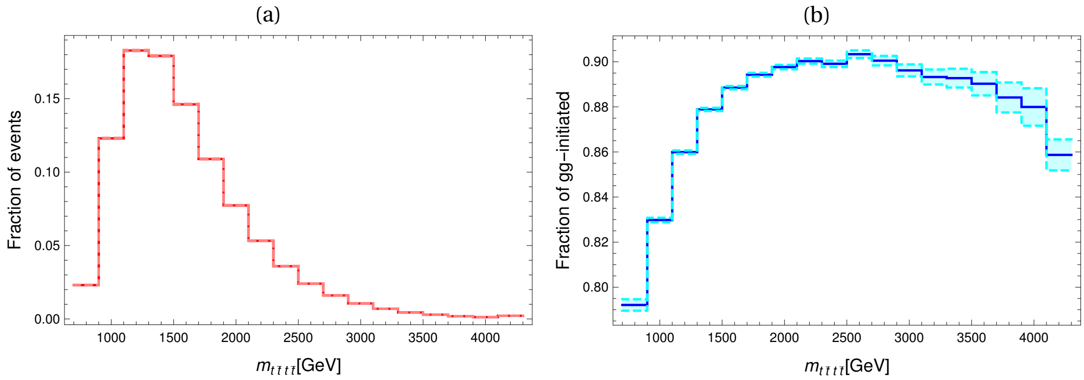

FIGURE B.1. Invariant mass distribution and fraction of events initiated through gluon-fusion for SM four-top production, in proton-proton collisions at $\sqrt{s} = 13$ TeV. Shadow areas correspond to the error bars (dashed lines), associated to the number of simulated events in each exclusive bin.

from Ref.[86, 106]. For the sake of computational resources we have only decayed the tops using `Madspin`. We have set Delphes parameters as in Ref. [179] which is tuned for CMS results in Ref. [102].

Objects at the detector level are defined as follows. Electrons are required to have $p_T > 20$ GeV and $|\eta| < 2.5$. Muons are required to have $p_T > 20$ GeV and $|\eta| < 2.4$. Hadronically decaying taus $p_T > 20$ GeV and $|\eta| < 2.5$. Jets are required to have $p_T > 40$ GeV and $|\eta| < 2.4$. Whereas b-tagged jets are demanded to have $p_T > 25$ GeV and $|\eta| < 2.4$.

B.1 Computational resources overview

Four-top is a very populated final state, and with ∼ 500 Feynman diagrams when the proton PDF is restricted to g, u, $\bar{u}$, d and $\bar{d}$. If in addition this partonic state is decayed with correlated spins in at least two of the partons, the simulation becomes still more involved. When simulating only SM the simulation includes QED tree corrections. When including NP, the Feynman diagrams are increased because of new diagrams. Table B.1 is a representative sample of the computational resources used to simulate some of the results in Chapter 3.

`Madgraph`	Model	CPU specifications	Comments	CPU hours
$pp \to t\bar{t}t\bar{t}$ QED=2 adapted for like-helicity tops	Scalar/ Pseudo-scalar	Intel Quad 2.4GHz	Figs. 3.5(a)-3.5(d). Grid of 4 BPs with 1M events each. Total: 4M events	100
$pp \to t\bar{t}t\bar{t}$ QED=2 `+Madspin` `+Pythia` `+Delphes`	Scalar/ Pseudo-scalar/ Vector Z'	Intel i7 3.4GHz	Complete calculation for each BP in Figs. 3.4, 3.7, C.4–C.6. Total: 0.5M events	200
$pp \to t\bar{t}t\bar{t}$ QED=2	Graviton	Intel i7 4GHz	Fig. 3.2(d) four-top contour levels. Grid of 170 BPs with 10K events each. Total: 1.7M events	1400

TABLE B.1. Representative computational resources used in Chapter 3.

Appendix C

Complementary plots for Chapter 3

We present in this appendix the plots which complement the results in Chapter 3. Figs. C.1, C.2 and C.3 (C.4, C.5, C.6 and C.7) contain the same (similar) analysis as those presented in Section 3.3, for loose (all) benchmark points.

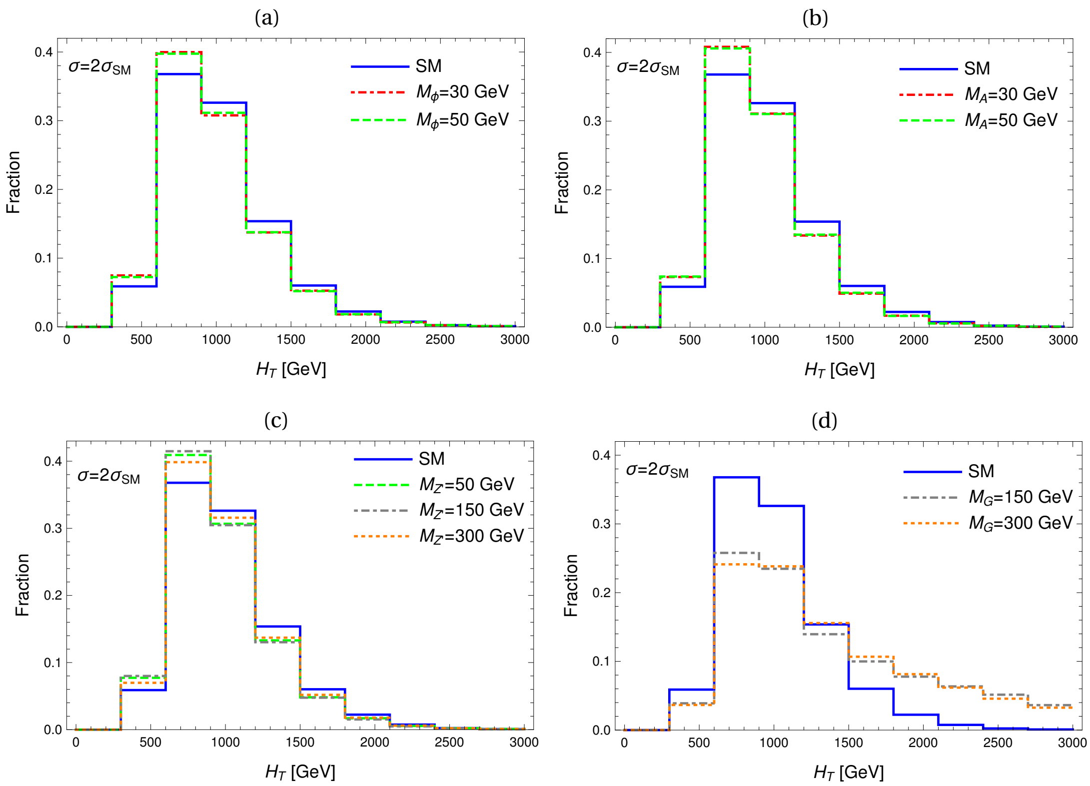

FIGURE C.1. Distribution of the H_T variable for the 2LSS channel after preselection (see text for details), normalized to unit area. Shown are the predictions for the SM (blue) and the loose benchmark points (i.e. giving $\sigma = 2\sigma_{SM}$) of the NP models considered: (a) Scalar, (b) Pseudo-scalar, (c) Z', and (d) Graviton. The distinctive behavior in the Graviton is due to the symmetry in one of its main Feynman diagrams (see Fig. 3.1(c)). Analogous results for tight benchmark points are shown in Fig. 3.4.

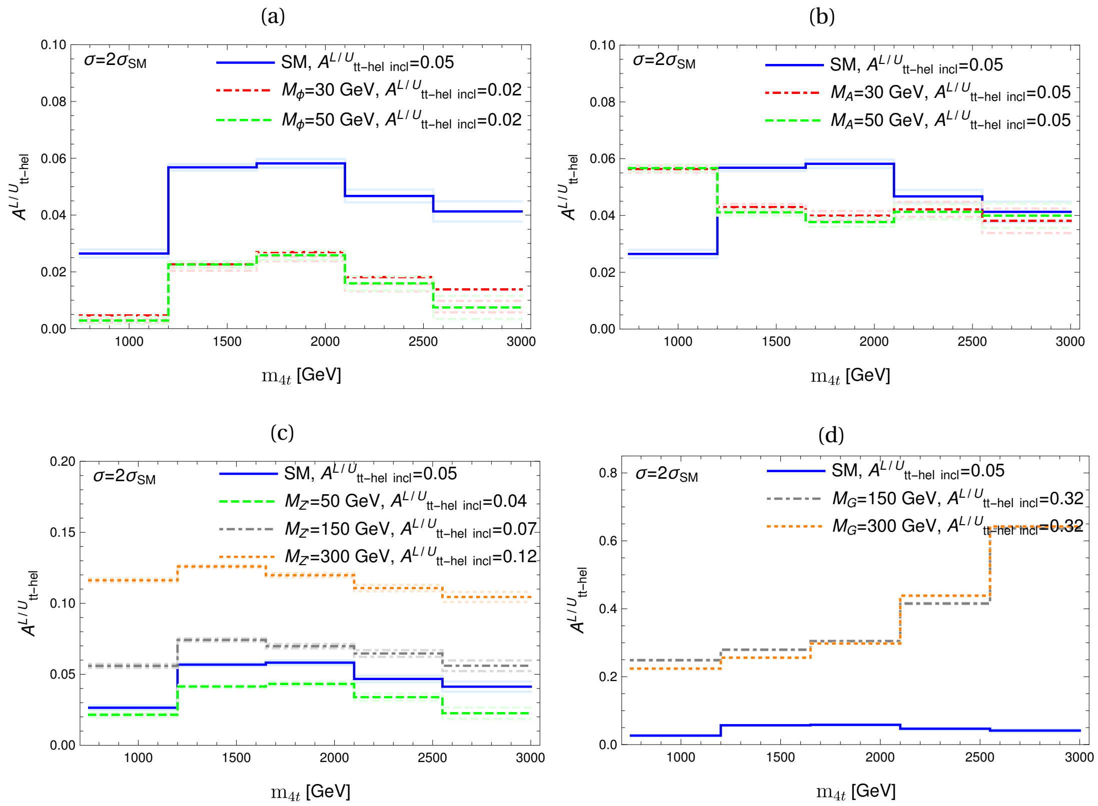

FIGURE C.2. $A^{L/U}_{\text{tt-hel}}$ asymmetry (see Eq. (3.1)) as a function of the invariant mass of the four-top system. Shown are the predictions for the SM (blue) and the loose benchmark points (i.e. giving $\sigma = 2\sigma_{SM}$) of the NP models considered: (a) Scalar, (b) Pseudo-scalar, (c) Z', and (d) Graviton. Also quoted are the inclusive asymmetries, i.e. averaged over the four-top invariant mass spectrum. Analogous results for the tight benchmark points (i.e. giving $\sigma = 1.5\sigma_{SM}$) are shown in Fig. 3.5.

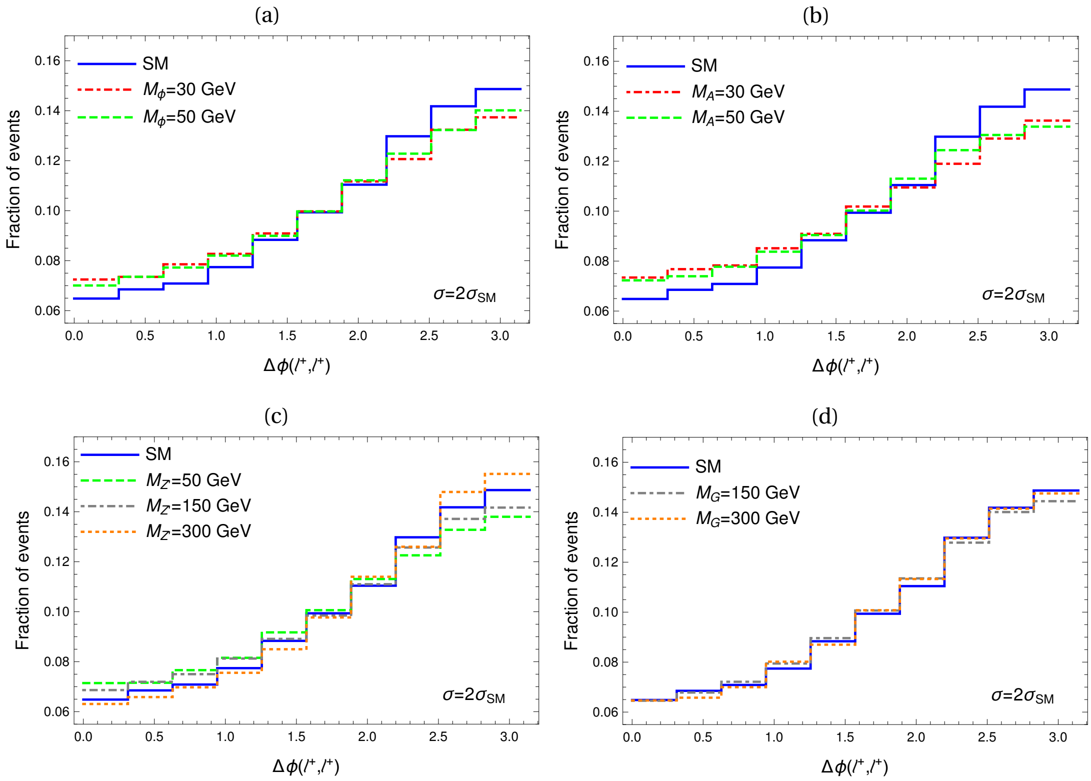

FIGURE C.3. Distribution of the azimuthal separation between the same-sign leptons, $\Delta\phi(\ell^+,\ell^+)$, for the 2LSS channel after preselection (see text for details), normalized to unit area. Shown are the predictions for the SM (blue) and the loose benchmark points (i.e. giving $\sigma = 2\sigma_{SM}$) of the NP models considered: (a) Scalar, (b) Pseudo-scalar, (c) Z', and (d) Graviton. Analogous results for the tight benchmark points (i.e. giving $\sigma = 1.5\sigma_{SM}$) are shown in Fig. 3.7.

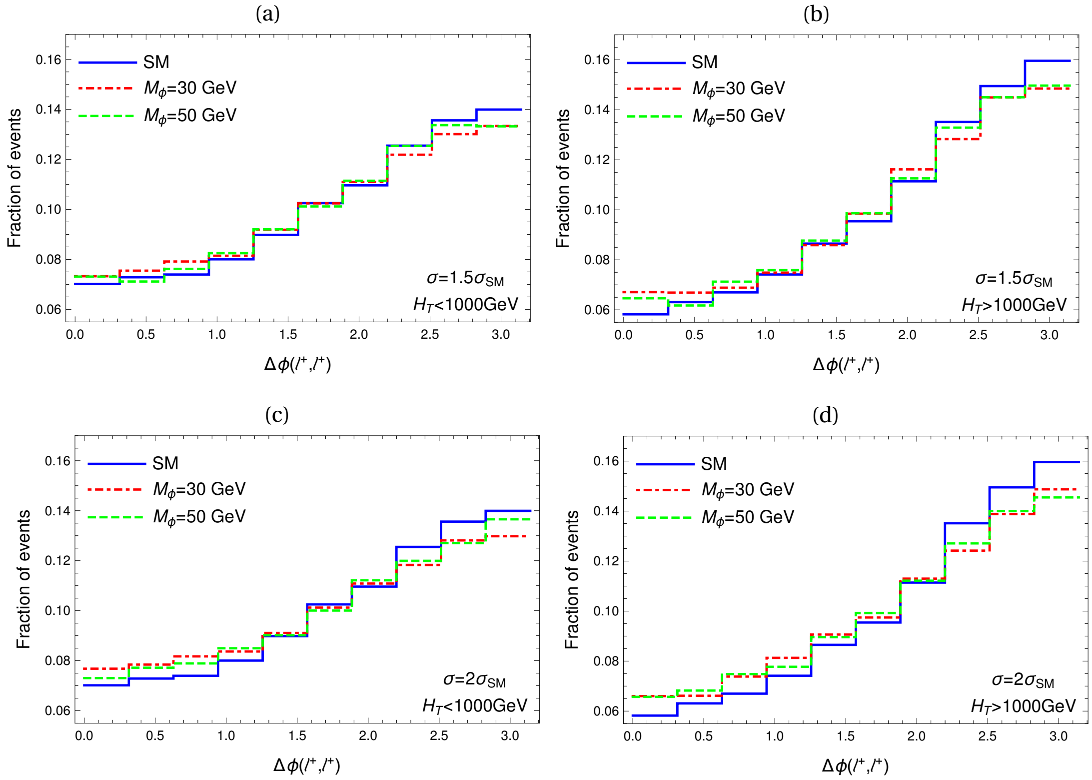

FIGURE C.4. Distribution of the azimuthal separation between the same-sign leptons, $\Delta\phi(\ell^+,\ell^+)$, for the 2LSS channel after preselection (see text for details) with (left) $H_{\mathrm{T}} < 1000$ GeV and (right) $H_{\mathrm{T}} > 1000$ GeV, normalized to unit area. Shown are the predictions for the SM (blue) and the Scalar model for (a, b) the tight benchmark points (i.e. giving $\sigma = 1.5\sigma_{SM}$) and (c, d) the loose benchmark points (i.e. giving $\sigma = 2\sigma_{SM}$).

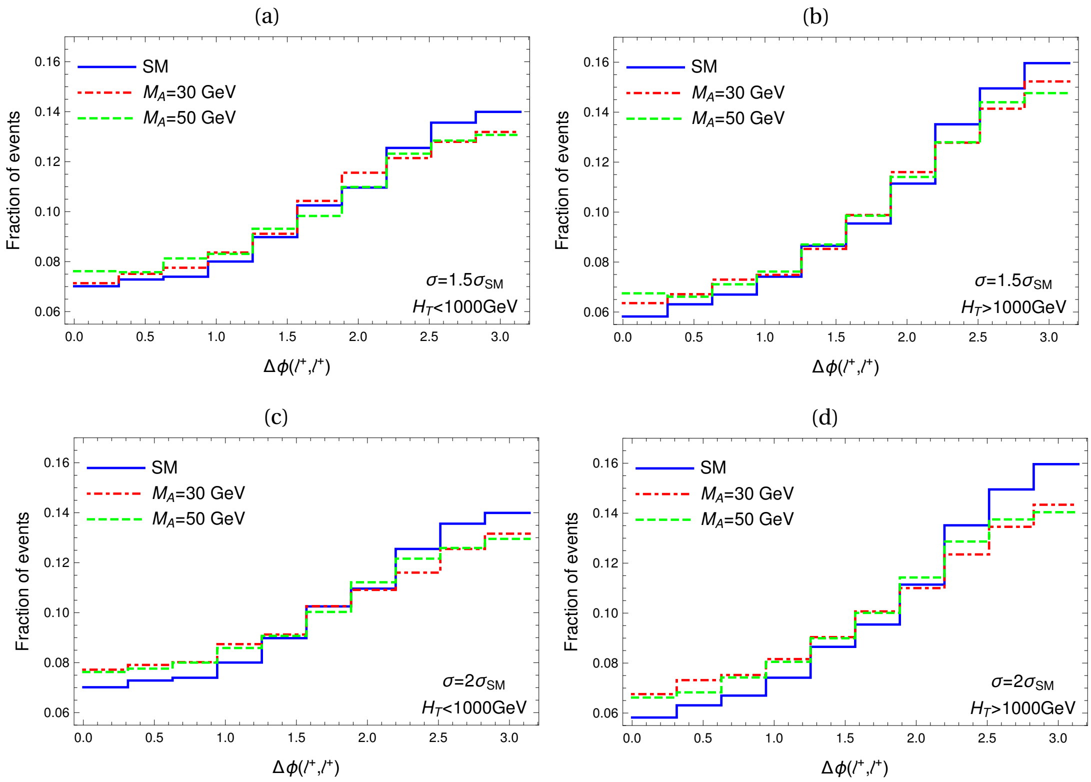

FIGURE C.5. Distribution of the azimuthal separation between the same-sign leptons, $\Delta\phi(\ell^+,\ell^+)$, for the 2LSS channel after preselection (see text for details) with (left) $H_T < 1000$ GeV and (right) $H_T > 1000$ GeV, normalized to unit area. Shown are the predictions for the SM (blue) and the Pseudo-scalar model for (a, b) the tight benchmark points (i.e. giving $\sigma = 1.5\sigma_{SM}$) and (c, d) the loose benchmark points (i.e. giving $\sigma = 2\sigma_{SM}$).

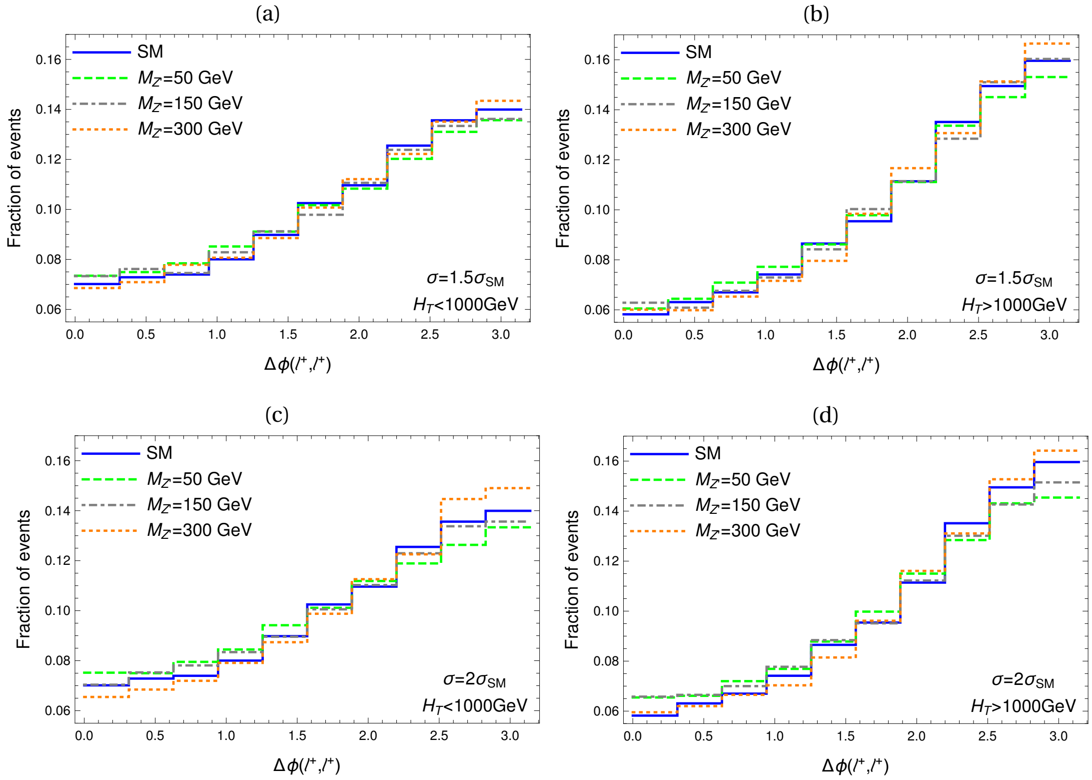

FIGURE C.6. Distribution of the azimuthal separation between the same-sign leptons, $\Delta\phi(\ell^+, \ell^+)$, for the 2LSS channel after preselection (see text for details) with (left) $H_T < 1000$ GeV and (right) $H_T > 1000$ GeV, normalized to unit area. Shown are the predictions for the SM (blue) and the Z' model for (a, b) the tight benchmark points (i.e. giving $\sigma = 1.5\sigma_{SM}$) and (c, d) the loose benchmark points (i.e. giving $\sigma = 2\sigma_{SM}$).

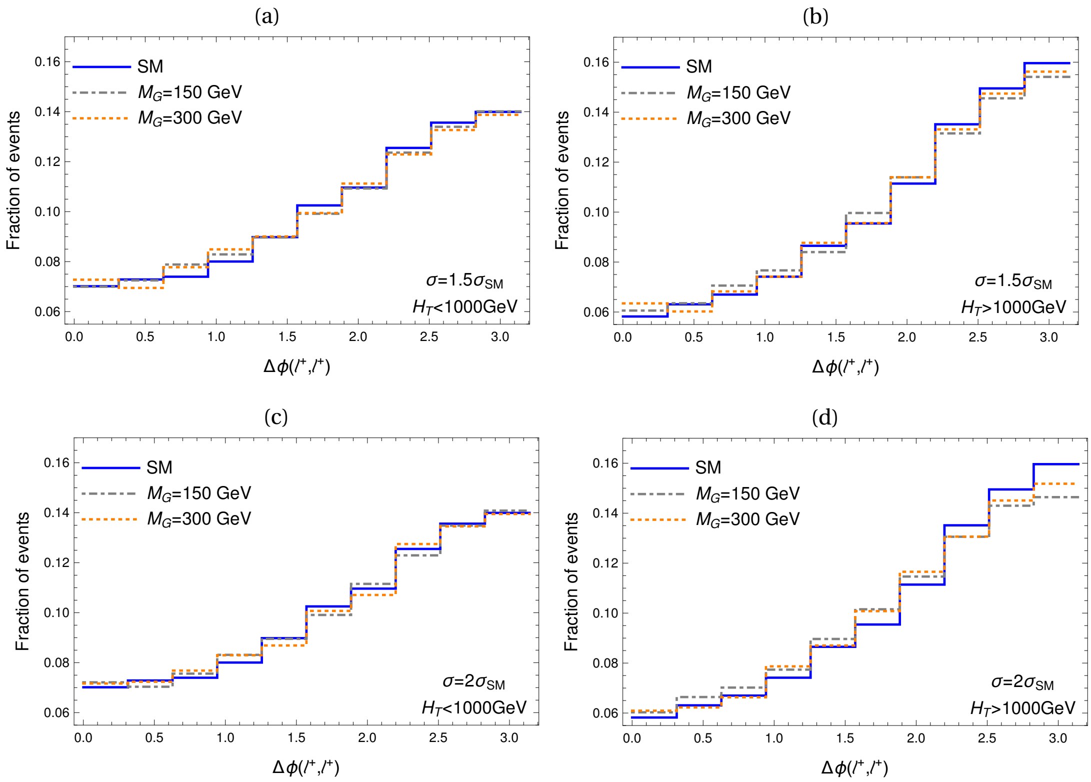

FIGURE C.7. Distribution of the azimuthal separation between the same-sign leptons, $\Delta\phi(\ell^+,\ell^+)$, for the 2LSS channel after preselection (see text for details) with (left) $H_\mathrm{T} < 1000$ GeV and (right) $H_\mathrm{T} > 1000$ GeV, normalized to unit area. Shown are the predictions for the SM (blue) and the Graviton model for (a, b) the tight benchmark points (i.e. giving $\sigma = 1.5\sigma_{SM}$) and (c, d) the loose benchmark points (i.e. giving $\sigma = 2\sigma_{SM}$).

APPENDIX D

Implementing Z'-explorer with taylored PDFs and/or other collider and run settings

In this Appendix we explained how to replace the default simulation cards in Z'-explorer (presented in 4.3.1), for new ones with other PDF and/or other `MadGraph5_aMC@NLO` collider and run choices. The first step is to download the UFO-model to implement the effective Z' lagrangian (`/extra-Zprime/`), from [137], and move it to your `MadGraph5_aMC@NLO` `/models/` local directory. Then also download all the files in the `/TayloredPDFs/` directory (`sim_cards_generator_1.bash`, `sim_cards_generator_2.bash`, `sim_cards.dat` and `masses_couplings_sim_cards.dat`) from [137], and copy them into your `MadGraph5_aMC@NLO` main directory. Once in it, considering a Linux environment, execute from terminal shell the following instruction:

```
>bash sim_cards_generator_1.bash
```

This `bash` file access the `MadGraph5_aMC@NLO` shell and execute the corresponding on-line commands (from `sim_cards.dat`) to generate five output directories (`/sim1uu/`, `/sim2dd/`, `/sim3cc/`, `/sim4ss/` and `/sim5bb/`), each of them with the Z' production process associated to the annhilation of the corresponding quark-antiquark pair. Go to the `/Cards/run_card.dat` inside each directory to modified the default PDF and set the one of your preference. Other parameters can be customized for the event generation, such us the number of events in each run (we recommend a minimum of 1K for a reliable computation of the cross-sections), or the renormalization and factorization scales. After that, once in the `MadGraph5_aMC@NLO` main directory again, execute the second `bash` file:

```
>bash sim_cards_generator_2.bash
```

This `bash` file access each output directory and automatically launch events generation for a set of values of Z' masses between 0.4 and 8.1 TeV, with a step of 0.01 TeV. These M_Z' are extracted from masses_couplings_sim_cards.dat. Changes inside the /Cards/param_card.dat of each folder are automatically done to ensure also that the corresponding quark couples with unity to Z' in each process. The bash file also extracts the corresponding cross-section in each iteration, to build the five simulation cards (see Table 4.1 for numbering scheme) inside your MadGraph5_aMC@NLO main directory. After execution, the simulation cards are ready to be used by Z'-explorer . Copy them into /Z'-explorer/cards/. No other step is required.

Bibliography

[1] F. Halzen and A. D. Martin, *Quarks and Leptons: An Introductory course in Modern Particle Physics* (1984), ISBN 978-0-471-88741-6.

[2] D. Griffiths, *Introduction to elementary particles* (2008), ISBN 978-3-527-40601-2

[3] M. D. Schwartz, *TASI Lectures on Collider Physics*, in *Proceedings of Theoretical Advanced Study Institute in Elementary Particle Physics : Exploring New Frontiers Using Colliders and Neutrinos (TASI 2006): Boulder, Colorado, June 4-30, 2006*, pp. 65–100, 2006. [1709.04533].

[4] J. F. Gunion, H. E. Haber, G. L. Kane and S. Dawson, *The Higgs Hunter's Guide*, Front. Phys. **80** (2000), 1-404 SCIPP-89/13.

[5] *LHC Machine*, *JINST* **3** (2008) S08001.

[6] ATLAS Collaboration, *Observation of a new particle in the search for the Standard Model Higgs boson with the ATLAS detector at the LHC*, *Phys. Lett. B* **716** (2012) 1, [1207.7214].

[7] CMS Collaboration, *Observation of a New Boson at a Mass of 125 GeV with the CMS Experiment at the LHC*, *Phys. Lett. B* **716** (2012) 30, [1207.7235].

[8] S. Capozziello and M. De Laurentis, *Extended Theories of Gravity*, *Phys. Rept.* **509** (2011) 167–321, [1108.6266].

[9] PLANCK Collaboration, N. Aghanim et al., *Planck 2018 results. VI. Cosmological parameters*, *Astron. Astrophys.* **641** (2020) A6, [1807.06209]. [Erratum: Astron.Astrophys. 652, C4 (2021)].

[10] PARTICLE DATA GROUP Collaboration, P. A. Zyla et al., *Review of Particle Physics*, *PTEP* **2020** (2020) 083C01.

[11] J. Silk et al., *Particle Dark Matter: Observations, Models and Searches*. Cambridge Univ. Press, Cambridge (2010), 10.1017/CBO9780511770739.

[12] SUPER-KAMIOKANDE Collaboration, Y. Fukuda et al., *Measurements of the solar neutrino flux from Super-Kamiokande's first 300 days*, *Phys. Rev. Lett.* **81** (1998) 1158–1162, [hep-ex/9805021]. [Erratum: Phys.Rev.Lett. 81, 4279 (1998)].

[13] J. Schechter and J. W. F. Valle, *Neutrino Masses in SU(2) x U(1) Theories*, *Phys. Rev. D* **22** (1980) 2227.

[14] L. Canetti, M. Drewes and M. Shaposhnikov, *Matter and Antimatter in the Universe*, *New J. Phys.* **14** (2012) 095012, [1204.4186].

[15] H.-Y. Cheng, *The Strong CP Problem Revisited*, *Phys. Rept.* **158** (1988) 1.

[16] ATLAS Collaboration, C. Bernius, *HL-LHC prospects from ATLAS and CMS*, tech. rep., CERN, Geneva, Mar, 2019.

[17] C. E. Gerber, *LHC Highlights and Prospects*, *CERN Yellow Rep. School Proc.* **2** (2021) 161, [1909.10919].

[18] D0 Collaboration, S. Abachi et al., *Observation of the top quark*, *Phys. Rev. Lett.* **74** (1995) 2632–2637, [hep-ex/9503003].

[19] C. Campagnari and M. Franklin, *The Discovery of the top quark*, *Rev. Mod. Phys.* **69** (1997) 137–212, [hep-ex/9608003].

[20] G. Mahlon and S. J. Parke, *Angular correlations in top quark pair production and decay at hadron colliders*, *Phys. Rev. D* **53** (1996) 4886–4896, [hep-ph/9512264].

[21] CMS Collaboration, *Measurement of the top polarization in the dilepton final state*, *CMS-PAS-TOP-12-016* (2012) . https://cds.cern.ch/record/1460102.

[22] L. Susskind, *Dynamics of Spontaneous Symmetry Breaking in the Weinberg-Salam Theory*, *Phys. Rev. D* **20** (1979) 2619–2625.

[23] D. B. Kaplan, H. Georgi and S. Dimopoulos, *Composite Higgs Scalars*, *Phys. Lett. B* **136** (1984) 187–190.

[24] N. Arkani-Hamed, A. G. Cohen, E. Katz and A. E. Nelson, *The Littlest Higgs*, *JHEP* **07** (2002) 034, [hep-ph/0206021].

[25] J. Wess and B. Zumino, *Supergauge Transformations in Four-Dimensions*, *Nucl. Phys. B* **70** (1974) 39–50.

[26] G. R. Farrar and P. Fayet, *Phenomenology of the Production, Decay, and Detection of New Hadronic States Associated with Supersymmetry*, *Phys. Lett. B* **76** (1978) 575–579.

[27] M. Toharia and J. D. Wells, *Gluino decays with heavier scalar superpartners*, *JHEP* **02** (2006) 015, [hep-ph/0503175].

[28] S. Calvet, B. Fuks, P. Gris and L. Valery, *Searching for sgluons in multitop events at a center-of-mass energy of 8 TeV*, *JHEP* **04** (2013) 043, [1212.3360].

[29] K. Kumar, T. M. P. Tait and R. Vega-Morales, *Manifestations of Top Compositeness at Colliders*, *JHEP* **05** (2009) 022, [0901.3808].

[30] G. Cacciapaglia, H. Cai, A. Deandrea, T. Flacke, S. J. Lee and A. Parolini, *Composite scalars at the LHC: the Higgs, the Sextet and the Octet*, *JHEP* **11** (2015) 201, [1507.02283].

[31] G. Cacciapaglia, A. Deandrea and J. Llodra-Perez, *A Dark Matter candidate from Lorentz Invariance in 6D*, *JHEP* **03** (2010) 083, [0907.4993].

[32] O. Ducu, L. Heurtier and J. Maurer, *LHC signatures of a Z' mediator between dark matter and the SU(3) sector*, *JHEP* **03** (2016) 006, [1509.05615].

[33] R. Contino, T. Kramer, M. Son and R. Sundrum, *Warped/composite phenomenology simplified*, *JHEP* **05** (2007) 074, [hep-ph/0612180].

[34] D. Marzocca, M. Serone and J. Shu, *General Composite Higgs Models*, *JHEP* **08** (2012) 013, [1205.0770].

[35] F. Caracciolo, A. Parolini and M. Serone, *UV Completions of Composite Higgs Models with Partial Compositeness*, *JHEP* **02** (2013) 066, [1211.7290].

[36] E. Alvarez, D. A. Faroughy, J. F. Kamenik, R. Morales and A. Szynkman, *Four Tops for LHC*, *Nucl. Phys. B* **915** (2017) 19, [1611.05032].

[37] P. S. Bhupal Dev and A. Pilaftsis, *Maximally Symmetric Two Higgs Doublet Model with Natural Standard Model Alignment*, *JHEP* **12** (2014) 024, [1408.3405]. [Erratum: JHEP **11** (2015) 147].

[38] M. Spira, *QCD effects in Higgs physics*, *Fortsch. Phys.* **46** (1998) 203–284, [hep-ph/9705337].

[39] E. Alvarez and M. Estevez, *$t\bar{t}b\bar{b}$ as a probe of new physics at the LHC*, *Phys. Rev. D* **96** (2017) 035016, [1701.04427].

[40] L. D. Landau, *On the angular momentum of a system of two photons*, *Dokl. Akad. Nauk Ser. Fiz.* **60** (1948) 207.

[41] C.-N. Yang, *Selection Rules for the Dematerialization of a Particle Into Two Photons*, *Phys. Rev.* **77** (1950) 242.

[42] P. J. Fox, I. Low and Y. Zhang, *Top-philic Z' forces at the LHC*, *JHEP* **03** (2018) 074, [1801.03505].

[43] W. Beenakker, R. Kleiss and G. Lustermans, *No Landau-Yang in QCD*, [1508.07115].

[44] V. Pleitez, *Angular momentum and parity of a two gluon system*, [1801.09294].

[45] M. Cacciari, L. Del Debbio, J. R. Espinosa, A. D. Polosa and M. Testa, *A note on the fate of the Landau-Yang theorem in non-Abelian gauge theories*, *Phys. Lett. B* **753** (2016) 476, [1509.07853].

[46] V. Pleitez, *The angular momentum of two massless fields revisited*, [1508.01394].

[47] E. Alvarez, L. Da Rold, J. Mazzitelli and A. Szynkman, *Graviton resonance phenomenology and a pseudo-Nambu-Goldstone boson Higgs at the LHC*, *Phys. Rev. D* **95** (2017) 115012, [1610.08451].

[48] C.-Q. Geng and D. Huang, *Note on spin-2 particle interpretation of the 750 GeV diphoton excess*, *Phys. Rev. D* **93** (2016) 115032, [1601.07385].

[49] P. Langacker, *The Physics of Heavy Z' Gauge Bosons*, *Rev. Mod. Phys.* **81** (2009) 1199–1228, [0801.1345].

[50] A. Leike, *The Phenomenology of extra neutral gauge bosons*, *Phys. Rept.* **317** (1999) 143–250, [hep-ph/9805494].

[51] J. L. Hewett and T. G. Rizzo, *Low-Energy Phenomenology of Superstring Inspired E(6) Models*, *Phys. Rept.* **183** (1989) 193.

[52] L. Randall and R. Sundrum, *A Large mass hierarchy from a small extra dimension*, *Phys. Rev. Lett.* **83** (1999) 3370–3373, [hep-ph/9905221].

[53] J. C. Pati and A. Salam, *Lepton Number as the Fourth Color*, *Phys. Rev. D* **10** (1974) 275–289. [Erratum: Phys.Rev.D 11, 703–703 (1975)].

[54] R. N. Mohapatra and J. C. Pati, *Left-Right Gauge Symmetry and an Isoconjugate Model of CP Violation*, *Phys. Rev. D* **11** (1975) 566–571.

[55] R. N. Mohapatra and G. Senjanovic, *Neutrino Masses and Mixings in Gauge Models with Spontaneous Parity Violation*, *Phys. Rev. D* **23** (1981) 165.

[56] R. N. Mohapatra and G. Senjanovic, *Neutrino Mass and Spontaneous Parity Nonconservation*, *Phys. Rev. Lett.* **44** (1980) 912.

[57] M. Bando, T. Kugo and K. Yamawaki, *Nonlinear Realization and Hidden Local Symmetries*, *Phys. Rept.* **164** (1988) 217–314.

[58] U. Baur, D. Schildknecht and K. H. G. Schwarzer, *Excited Weak Vector Bosons*, *Phys. Rev. D* **35** (1987) 297.

[59] M. B. Green and J. H. Schwarz, *Anomaly Cancellation in Supersymmetric D=10 Gauge Theory and Superstring Theory*, *Phys. Lett. B* **149** (1984) 117–122.

[60] G. Cleaver, M. Cvetic, J. R. Espinosa, L. L. Everett, P. Langacker and J. Wang, *Physics implications of flat directions in free fermionic superstring models. 2. Renormalization group analysis*, *Phys. Rev. D* **59** (1999) 115003, [hep-ph/9811355].

[61] W. Buchmuller, C. Greub and P. Minkowski, *Neutrino masses, neutral vector bosons and the scale of B-L breaking*, *Phys. Lett. B* **267** (1991) 395–399.

[62] A. Gutiérrez-Rodríguez and M. A. Hernández-Ruiz, *Z' resonance and associated Zh production at future Higgs boson factory: ILC and CLIC*, *Adv. High Energy Phys.* **2015** (2015) 593898, [1506.07575].

[63] L. Basso, *Phenomenology of the minimal B-L extension of the Standard Model at the LHC.* PhD thesis, Southampton U., 2011. [1106.4462].

[64] S. Khalil, *Low scale $B-L$ extension of the Standard Model at the LHC*, *J. Phys.* **G35** (2008) 055001, [hep-ph/0611205].

[65] T. G. Rizzo, *Z' phenomenology and the LHC*, in *Proceedings of Theoretical Advanced Study Institute in Elementary Particle Physics : Exploring New Frontiers Using Colliders and Neutrinos (TASI 2006): Boulder, Colorado, June 4-30, 2006*, pp. 537–575, 2006. [hep-ph/0610104].

[66] L. Basso, S. Moretti and G. M. Pruna, *A Renormalisation Group Equation Study of the Scalar Sector of the Minimal B-L Extension of the Standard Model*, *Phys. Rev.* **D82** (2010) 055018, [1004.3039].

[67] PARTICLE DATA GROUP Collaboration, M. Tanabashi et al., *Review of Particle Physics*, *Phys. Rev.* **D98** (2018) 030001.

[68] G. Cacciapaglia, C. Csaki, G. Marandella and A. Strumia, *The Minimal Set of Electroweak Precision Parameters*, *Phys. Rev. D* **74** (2006) 033011, [hep-ph/0604111].

[69] V. Barger and K. Whisnant, *Heavy-z-boson decays to two bosons in* e_6 *superstring models*, *Phys. Rev. D* **36** (Dec, 1987) 3429–3437.

[70] V. Barger, P. Langacker and H.-S. Lee, *Six-lepton Z-prime resonance at the LHC*, *Phys. Rev. Lett.* **103** (2009) 251802, [0909.2641].

[71] G. Bertone, D. Hooper and J. Silk, *Particle dark matter: Evidence, candidates and constraints*, *Phys. Rept.* **405** (2005) 279–390, [hep-ph/0404175].

[72] G. Jungman, M. Kamionkowski and K. Griest, *Supersymmetric dark matter*, *Phys. Rept.* **267** (1996) 195–373, [hep-ph/9506380].

[73] Y. Bai and J. Berger, *Fermion Portal Dark Matter*, *JHEP* **11** (2013) 171, [1308.0612].

[74] O. Buchmueller, M. J. Dolan, S. A. Malik and C. McCabe, *Characterising dark matter searches at colliders and direct detection experiments: Vector mediators*, *JHEP* **01** (2015) 037, [1407.8257].

[75] D. Abercrombie et al., *Dark Matter benchmark models for early LHC Run-2 Searches: Report of the ATLAS/CMS Dark Matter Forum*, *Phys. Dark Univ.* **27** (2020) 100371, [1507.00966].

[76] F. Kahlhoefer, K. Schmidt-Hoberg, T. Schwetz, and S. Vogl, *Implications of unitarity and gauge invariance for simplified dark matter models*, *JHEP* **02** (2016) 016, [1510.02110].

[77] Y. Cui and F. D'Eramo, *Surprises from complete vector portal theories: New insights into the dark sector and its interplay with Higgs physics*, *Phys. Rev. D* **96** (2017), no. 9 095006, [1705.03897].

[78] J. Alison et al., *Higgs boson pair production at colliders: status and perspectives*, in *Double Higgs Production at Colliders Batavia, IL, USA, September 4, 2018-9, 2019* (B. Di Micco, M. Gouzevitch, J. Mazzitelli and C. Vernieri, eds.), 2019. [1910.00012].

[79] ATLAS Collaboration, *Search for non-resonant Higgs boson pair production in the $bb\ell\nu\ell\nu$ final state with the ATLAS detector in pp collisions at $\sqrt{s} = 13$ TeV*, [1908.06765].

[80] CMS Collaboration, *Search for the resonant production of a pair of Higgs bosons decaying to the $b\bar{b}ZZ$ final state*, *CMS-PAS-HIG-18-013* (2019) . https://cds.cern.ch/record/2682621.

[81] CMS Collaboration, *Measurement of the associated production of a Higgs boson and a pair of top-antitop quarks with the Higgs boson decaying to two photons in proton-proton collisions at $\sqrt{s} = 13$ TeV*, *CMS-PAS-HIG-18-018* (2018) . https://cds.cern.ch/record/2649208.

[82] D. Madaffari, *Higgs boson production in association with a top quark pair at the LHC*, *PoS* **ALPS2018** (2018) 019.

[83] ATLAS Collaboration, *Observation of Higgs boson production in association with a top quark pair at the LHC with the ATLAS detector*, *Phys. Lett. B* **784** (2018) 173, [1806.00425].

[84] ATLAS Collaboration, *Search for production of vector-like quark pairs and of four top quarks in the lepton-plus-jets final state in pp collisions at $\sqrt{s} = 8$ TeV with the ATLAS detector*, *JHEP* **08** (2015) 105, [1505.04306].

[85] ATLAS Collaboration, *Analysis of events with b-jets and a pair of leptons of the same charge in pp collisions at $\sqrt{s} = 8$ TeV with the ATLAS detector*, *JHEP* **10** (2015) 150, [1504.04605].

[86] CMS Collaboration, *Search for production of four top quarks in final states with same-sign or multiple leptons in proton-proton collisions at $\sqrt{s} = 13$ TeV*, [1908.06463].

[87] Q.-H. Cao, S.-L. Chen and Y. Liu, *Probing Higgs Width and Top Quark Yukawa Coupling from $t\bar{t}H$ and $t\bar{t}t\bar{t}$ Productions*, *Phys. Rev. D* **95** (2017) 053004, [1602.01934].

[88] Q.-H. Cao, S.-L. Chen, Y. Liu, R. Zhang and Y. Zhang, *Limiting top quark-Higgs boson interaction and Higgs-boson width from multitop productions*, *Phys. Rev. D* **99** (2019) 113003, [1901.04567].

[89] C. Englert, G. F. Giudice, A. Greljo and M. Mccullough, *The $\hat{H}$-Parameter: An Oblique Higgs View*, *JHEP* **09** (2019) 041, [1903.07725].

[90] M. Battaglia and G. Servant, *Four-top production and t tbar + missing energy events at multi TeV e+e- colliders*, *Nuovo Cim.* **C033N2** (2010) 203, [1005.4632].

[91] C. Degrande, J.-M. Gerard, C. Grojean, F. Maltoni and G. Servant, *Non-resonant New Physics in Top Pair Production at Hadron Colliders*, *JHEP* **03** (2011) 125, [1010.6304].

[92] B. Lillie, J. Shu and T. M. P. Tait, *Top Compositeness at the Tevatron and LHC*, *JHEP* **04** (2008) 087, [0712.3057].

[93] N. Greiner, K. Kong, J.-C. Park, S. C. Park and J.-C. Winter, *Model-Independent Production of a Top-Philic Resonance at the LHC*, *JHEP* **04** (2015) 029, [1410.6099].

[94] HL-LHC, HE-LHC WORKING GROUP Collaboration, P. Azzi et al., *Standard Model Physics at the HL-LHC and HE-LHC*, [1902.04070].

[95] L. Darmé, B. Fuks and M. Goodsell, *Cornering sgluons with four-top-quark events*, *Phys. Lett. B* **784** (2018) 223, [1805.10835].

[96] C. Zhang, *Constraining $qqtt$ operators from four-top production: a case for enhanced EFT sensitivity*, *Chin. Phys. C* **42** (2018) 023104, [1708.05928].

[97] E. Alvarez, F. Lamagna and M. Szewc, *Topic Model for four-top at the LHC*, [1911.09699].

[98] ATLAS Collaboration, *Search for supersymmetry at $\sqrt{s} = 8$ TeV in final states with jets and two same-sign leptons or three leptons with the ATLAS detector*, *JHEP* **06** (2014) 035, [1404.2500].

[99] CMS Collaboration, *Search for Standard Model Production of Four Top Quarks in the Lepton + Jets Channel in pp Collisions at $\sqrt{s} = 8$ TeV*, *JHEP* **11** (2014) 154, [1409.7339].

[100] CMS Collaboration, *Search for standard model production of four top quarks in proton-proton collisions at $\sqrt{s} = 13$ TeV*, *Phys. Lett. B* **772** (2017) 336, [1702.06164].

[101] CMS Collaboration, *Search for physics beyond the standard model in events with two leptons of same sign, missing transverse momentum, and jets in proton-proton collisions at $\sqrt{s} = 13$ TeV*, *Eur. Phys. J. C* **77** (2017) 578, [1704.07323].

[102] CMS Collaboration, *Search for standard model production of four top quarks with same-sign and multilepton final states in proton-proton collisions at* $\sqrt{s} = 13$ *TeV*, *Eur. Phys. J. C* **78** (2018) 140, [1710.10614].

[103] ATLAS Collaboration, *Search for four-top-quark production in the single-lepton and opposite-sign dilepton final states in pp collisions at* $\sqrt{s} = 13$ *TeV with the ATLAS detector*, *Phys. Rev. D* **99** (2019) 052009, [1811.02305].

[104] ATLAS Collaboration, *Search for new phenomena in events with same-charge leptons and b-jets in* pp *collisions at* $\sqrt{s} = 13$ *TeV with the ATLAS detector*, *JHEP* **12** (2018) 039, [1807.11883].

[105] CMS Collaboration, *Search for the Production of Four Top Quarks in the Single-Lepton and Opposite-Sign Dilepton Final States in Proton-Proton Collisions at* $\sqrt{s} = 13$ *TeV*, [1906.02805].

[106] R. Frederix, D. Pagani and M. Zaro, *Large NLO corrections in* $t\bar{t}W^{\pm}$ *and* $t\bar{t}t\bar{t}$ *hadroproduction from supposedly subleading EW contributions*, *JHEP* **02** (2018) 031, [1711.02116].

[107] J. H. Kühn, A. Scharf and P. Uwer, *Weak Interactions in Top-Quark Pair Production at Hadron Colliders: An Update*, *Phys. Rev. D* **91** (2015) 014020, [1305.5773].

[108] CMS Collaboration, *Constraining the top quark Yukawa coupling from* $t\bar{t}$ *differential cross sections in the lepton+jets final state in proton-proton collisions at* $\sqrt{s} = 13$ *TeV*, *CMS-PAS-TOP-17-004* (2019) . https://cds.cern.ch/record/2665937.

[109] ATLAS Collaboration, *Search for Scalar Diphoton Resonances in the Mass Range* 65 – 600 *GeV with the ATLAS Detector in* pp *Collision Data at* $\sqrt{s} = 8\ TeV$, *Phys. Rev. Lett.* **113** (2014) 171801, [1407.6583].

[110] ATLAS Collaboration, *Search for new phenomena in high-mass diphoton final states using 37* fb^{-1} *of proton–proton collisions collected at* $\sqrt{s} = 13$ *TeV with the ATLAS detector*, *Phys. Lett. B* **775** (2017) 105, [1707.04147].

[111] ATLAS Collaboration, *Search for resonances in the 65 to 110 GeV diphoton invariant mass range using 80* fb^{-1} *of* pp *collisions collected at* $\sqrt{s} = 13$ *TeV with the ATLAS detector*, *ATLAS-CONF-2018-025* (2018) . https://cds.cern.ch/record/2628760.

[112] CMS Collaboration, *Search for diphoton resonances in the mass range from 150 to 850 GeV in pp collisions at* $\sqrt{s} = 8$ *TeV*, *Phys. Lett. B* **750** (2015) 494, [1506.02301].

[113] CMS Collaboration, *Search for a standard model-like Higgs boson in the mass range between 70 and 110 GeV in the diphoton final state in proton-proton collisions at* $\sqrt{s} = 8$ *and 13 TeV*, *Phys. Lett. B* **793** (2019) 320, [1811.08459].

[114] G. Bevilacqua and M. Worek, *Constraining BSM Physics at the LHC: Four top final states with NLO accuracy in perturbative QCD*, *JHEP* **07** (2012) 111, [1206.3064].

[115] J. J. van der Bij and E. W. N. Glover, *Z Boson Production and Decay via Gluons*, *Nucl. Phys. B* **313** (1989) 237.

[116] ATLAS Collaboration, G. Aad et al., *Search for new resonances in mass distributions of jet pairs using 139 fb^{-1} of pp collisions at $\sqrt{s} = 13$ TeV with the ATLAS detector*, [1910.08447].

[117] CMS Collaboration, *A search for dijet resonances in proton-proton collisions at $\sqrt{s} = 13$ TeV with a new background prediction method*, *CCMS-PAS-EXO-19-012* (2019) . https://cds.cern.ch/record/2682120

[118] ATLAS Collaboration, M. Aaboud et al., *Search for low-mass dijet resonances using trigger-level jets with the ATLAS detector in pp collisions at $\sqrt{s} = 13$ TeV*, *Phys. Rev. Lett.* **121** (2018) 081801, [1804.03496].

[119] ATLAS Collaboration, M. Aaboud et al., *Search for resonances in the mass distribution of jet pairs with one or two jets identified as b-jets in proton-proton collisions at $\sqrt{s} = 13$ TeV with the ATLAS detector*, *Phys. Rev.* **D98** (2018) 032016, [1805.09299].

[120] CMS Collaboration, A. M. Sirunyan et al., *Search for resonant $\mathrm{t\bar{t}}$ production in proton-proton collisions at $\sqrt{s} = 13$ TeV*, *JHEP* **04** (2019) 031, [1810.05905].

[121] ATLAS Collaboration, M. Aaboud et al., *Search for heavy particles decaying into top-quark pairs using lepton-plus-jets events in proton-proton collisions at $\sqrt{s} = 13$ TeV with the ATLAS detector*, *Eur. Phys. J.* **C78** (2018) 565, [1804.10823].

[122] CMS Collaboration, *Search for a narrow resonance in high-mass dilepton final states in proton-proton collisions using 140 fb^{-1} of data at $\sqrt{s} = 13$ TeV*, *CMS-PAS-EXO-19-019* (2019) . https://cds.cern.ch/record/2684757.

[123] ATLAS collaboration, M. Aaboud et al., *Performance of top-quark and W-boson tagging with ATLAS in Run 2 of the LHC*, *Eur. Phys. J. C* **79** (2019) 375, [1808.07858].

[124] ATLAS Collaboration, G. Aad et al., *Search for high-mass dilepton resonances using 139 fb^{-1} of pp collision data collected at $\sqrt{s}$ = 13 TeV with the ATLAS detector*, *Phys. Lett.* **B796** (2019) 68–87, [1903.06248].

[125] ATLAS Collaboration, M. Aaboud et al., *Search for additional heavy neutral Higgs and gauge bosons in the ditau final state produced in 36 fb^{-1} of pp collisions at $\sqrt{s} = 13$ TeV with the ATLAS detector*, *JHEP* **01** (2018) 055, [1709.07242].

[126] CMS Collaboration, V. Khachatryan et al., *Search for heavy resonances decaying to tau lepton pairs in proton-proton collisions at $\sqrt{s} = 13$ TeV*, *JHEP* **02** (2017) 048, [1611.06594].

[127] ATLAS Collaboration, M. Aaboud et al., *Search for WW/WZ resonance production in $\ell\nu qq$ final states in pp collisions at $\sqrt{s}$ = 13 TeV with the ATLAS detector*, *JHEP* **03** (2018) 042, [1710.07235].

[128] CMS Collaboration, A. M. Sirunyan et al., *Combination of CMS searches for heavy resonances decaying to pairs of bosons or leptons*, *Phys. Lett.* **B798** (2019) 134952, [1906.00057].

[129] E. Alvarez, L. Da Rold, J. Mazzitelli and A. Szynkman, *A 750 GeV graviton and the Higgs as a pNGB*, [1606.05326].

[130] S. Kraml, S. Kulkarni, U. Laa, A. Lessa, W. Magerl, D. Proschofsky-Spindler et al., *SModelS: a tool for interpreting simplified-model results from the LHC and its application to supersymmetry*, *Eur. Phys. J.* **C74** (2014) 2868, [1312.4175].

[131] M. Papucci, K. Sakurai, A. Weiler and L. Zeune, *Fastlim: a fast LHC limit calculator*, *Eur. Phys. J.* **C74** (2014) 3163, [1402.0492].

[132] M. Drees, H. Dreiner, D. Schmeier, J. Tattersall and J. S. Kim, *CheckMATE: Confronting your Favourite New Physics Model with LHC Data*, *Comput. Phys. Commun.* **187** (2015) 227–265, [1312.2591].

[133] D. Dercks, N. Desai, J. S. Kim, K. Rolbiecki, J. Tattersall and T. Weber, *CheckMATE 2: From the model to the limit*, *Comput. Phys. Commun.* **221** (2017) 383–418, [1611.09856].

[134] D. Barducci, G. Belanger, J. Bernon, F. Boudjema, J. Da Silva, S. Kraml et al., *Collider limits on new physics within micrOMEGAs_4.3*, *Comput. Phys. Commun.* **222** (2018) 327–338, [1606.03834].

[135] J. M. Butterworth, D. Grellscheid, M. Krämer, B. Sarrazin and D. Yallup, *Constraining new physics with collider measurements of Standard Model signatures*, *JHEP* **03** (2017) 078, [1606.05296].

[136] F. Kahlhoefer, A. Mück, S. Schulte and P. Tunney, *Interference effects in dilepton resonance searches for Z' bosons and dark matter mediators*, *JHEP* **03** (2020) 104, [1912.06374].

[137] E. Alvarez, M. Estévez and R.M. Sandá Seoane, source scripts for software in this work, GIT repository https://github.com/ro-sanda/Z–explorer.

[138] J. Alwall, R. Frederix, S. Frixione, V. Hirschi, F. Maltoni, O. Mattelaer et al., *The automated computation of tree-level and next-to-leading order differential cross sections, and their matching to parton shower simulations*, *JHEP* **07** (2014) 079, [1405.0301].

[139] A. Alloul, N. D. Christensen, C. Degrande, C. Duhr and B. Fuks, *FeynRules 2.0 - A complete toolbox for tree-level phenomenology*, *Comput. Phys. Commun.* **185** (2014) 2250, [1310.1921].

[140] https://www.hepdata.net/.

[141] P. Uwer, *EasyNData: A Simple tool to extract numerical values from published plots*, [0710.2896].

[142] Wolfram Research, Inc., *Mathematica, Version 12.3.1*, Champaign, IL (2021).

[143] G. Altarelli, B. Mele and M. Ruiz-Altaba, *Searching for New Heavy Vector Bosons in $p\bar{p}$ Colliders*, *Z. Phys.* **C45** (1989) 109. [Erratum: Z. Phys.C47,676(1990)].

[144] LHC Reinterpretation Forum collaboration, W. Abdallah et al., *Reinterpretation of LHC Results for New Physics: Status and Recommendations after Run 2*, *SciPost Phys.* **9** (2020) 022, [2003.07868].

[145] B. Dumont, B. Fuks, S. Kraml, S. Bein, G. Chalons, E. Conte et al., *Toward a public analysis database for LHC new physics searches using MADANALYSIS 5*, *Eur. Phys. J. C* **75** (2015) 56, [1407.3278].

[146] E. Conte and B. Fuks, *Confronting new physics theories to LHC data with MADANALYSIS 5*, *Int. J. Mod. Phys. A* **33** (2018) 1830027, [1808.00480].

[147] GAMBIT Collaboration, P. Athron et al., *GAMBIT: The Global and Modular Beyond-the-Standard-Model Inference Tool*, *Eur. Phys. J. C* **77** (2017) 784, [1705.07908]. [Addendum: Eur.Phys.J.C 78, 98 (2018)].

[148] H. Bahl, V. M. Lozano, T. Stefaniak and J. Wittbrodt, *Testing Exotic Scalars with HiggsBounds*, [2109.10366].

[149] P. Bechtle, S. Heinemeyer, T. Klingl, T. Stefaniak, G. Weiglein and J. Wittbrodt, *HiggsSignals-2: Probing new physics with precision Higgs measurements in the LHC 13 TeV era*, *Eur. Phys. J. C* **81** (2021) 145, [2012.09197].

[150] S. Kraml, S. Kulkarni, U. Laa, A. Lessa, W. Magerl, D. Proschofsky-Spindler et al., *SModelS: a tool for interpreting simplified-model results from the LHC and its application to supersymmetry*, *Eur. Phys. J.* **C74** (2014) 2868, [1312.4175].

[151] ATLAS Collaboration, G. Aad et al., *Search for new phenomena in events with an energetic jet and missing transverse momentum in pp collisions at $\sqrt{s}$ =13 TeV with the ATLAS detector*, *Phys. Rev. D* **103** (2021) 112006, [2102.10874].

[152] E. Bernreuther, J. Horak, T. Plehn and A. Butter, *Actual Physics behind Mono-X*, *SciPost Phys.* **5** (2018) 034, [1805.11637].

[153] D. M. Straub, *flavio: a Python package for flavour and precision phenomenology in the Standard Model and beyond*, [1810.08132].

[154] V.M. Lozano, R.M. Sandá Seoane and J. Zurita, source scripts for software in this work, GIT repository `https://github.com/ro-sanda/Z--explorer-2.0`.

[155] ATLAS Collaboration, G. Aad et al., *Search for dark matter produced in association with a Standard Model Higgs boson decaying into b-quarks using the full Run 2 dataset from the ATLAS detector*, [2108.13391].

[156] ATLAS Collaboration, M. Aaboud et al., *Search for dark matter in events with a hadronically decaying vector boson and missing transverse momentum in pp collisions at $\sqrt{s} = 13$ TeV with the ATLAS detector*, *JHEP* **10** (2018) 180, [1807.11471].

[157] ATLAS Collaboration, M. Aaboud et al., *Search for an invisibly decaying Higgs boson or dark matter candidates produced in association with a Z boson in pp collisions at $\sqrt{s}$ = 13 TeV with the ATLAS detector*, *Phys. Lett. B* **776** (2018) 318–337, [1708.09624].

[158] ATLAS Collaboration, G. Aad et al., *Search for dark matter in association with an energetic photon in pp collisions at $\sqrt{s}$ = 13 TeV with the ATLAS detector*, *JHEP* **02** (2021) 226, [2011.05259].

[159] CMS Collaboration, A. Tumasyan et al., *Search for new particles in events with energetic jets and large missing transverse momentum in proton-proton collisions at $\sqrt{s}$ = 13 TeV*, [2107.13021].

[160] CMS Collaboration, A. M. Sirunyan et al., *Search for new physics in final states with an energetic jet or a hadronically decaying W or Z boson and transverse momentum imbalance at* $\sqrt{s} = 13$ TeV, *Phys. Rev. D* **97** (2018) 092005, [1712.02345].

[161] CMS Collaboration, A. M. Sirunyan et al., *Search for dark matter produced with an energetic jet or a hadronically decaying W or Z boson at $\sqrt{s} = 13$ TeV*, *JHEP* **07** (2017) 014, [1703.01651].

[162] CMS Collaboration, A. M. Sirunyan et al., *Search for new physics in the monophoton final state in proton-proton collisions at $\sqrt{s} = 13$ TeV*, *JHEP* **10** (2017) 073, [1706.03794].

[163] ATLAS Collaboration, M. Aaboud et al., *Search for dark matter and other new phenomena in events with an energetic jet and large missing transverse momentum using the ATLAS detector*, *JHEP* **01** (2018) 126, [1711.03301].

[164] C. Degrande, C. Duhr, B. Fuks, D. Grellscheid, O. Mattelaer and T. Reiter, *UFO - The Universal FeynRules Output*, *Comput. Phys. Commun.* **183** (2012) 1201–1214, [1108.2040].

[165] `http://feynrules.irmp.ucl.ac.be/wiki/DMsimp`.

[166] T. Sjöstrand, S. Ask, J. R. Christiansen, R. Corke, N. Desai, P. Ilten et al., *An Introduction to PYTHIA 8.2*, *Comput. Phys. Commun.* **191** (2015) 159, [1410.3012].

[167] T. Sjöstrand, S. Mrenna and P. Z. Skands, *PYTHIA 6.4 Physics and Manual*, *JHEP* **05** (2006) 026, [hep-ph/0603175].

[168] J. de Favereau, C. Delaere, P. Demin, A. Giammanco, V. Lemaître, A. Mertens et al., *DELPHES 3, A modular framework for fast simulation of a generic collider experiment*, *JHEP* **02** (2014) 057, [1307.6346].

[169] M. Backović, M. Krämer, F. Maltoni, A. Martini, K. Mawatari and M. Pellen, *Higher-order QCD predictions for dark matter production at the LHC in simplified models with s-channel mediators*, *Eur. Phys. J. C* **75** (2015) 482, [1508.05327].

[170] J. Alwall, C. Duhr, B. Fuks, O. Mattelaer, D. G. Öztürk and C.-H. Shen, *Computing decay rates for new physics theories with FeynRules and MadGraph 5_aMC@NLO*, *Comput. Phys. Commun.* **197** (2015) 312–323, [1402.1178].

[171] CMS Collaboration, A. M. Sirunyan et al., *Search for resonant and nonresonant new phenomena in high-mass dilepton final states at $\sqrt{s} = 13$ TeV*, *JHEP* **07** (2021) 208, [2103.02708].

[172] CMS Collaboration, A. Tumasyan et al., *Search for heavy resonances decaying to WW, WZ, or WH boson pairs in the lepton plus merged jet final state in proton-proton collisions at $\sqrt{s} = 13$ TeV*, [2109.06055].

[173] C. Shimmin and D. Whiteson, *Boosting low-mass hadronic resonances*, *Phys. Rev. D* **94** (2016) 055001, [1602.07727].

[174] CMS Collaboration, A. M. Sirunyan et al., *Search for low mass vector resonances decaying into quark-antiquark pairs in proton-proton collisions at $\sqrt{s} = 13$ TeV*, *JHEP* **01** (2018) 097, [1710.00159].

[175] ATLAS Collaboration, M. Aaboud et al., *Search for light resonances decaying to boosted quark pairs and produced in association with a photon or a jet in proton-proton collisions at $\sqrt{s} = 13$ TeV with the ATLAS detector*, *Phys. Lett. B* **788** (2019) 316–335, [1801.08769].

[176] A. Djouadi, J. Kalinowski and P. M. Zerwas, *Two and three-body decay modes of SUSY Higgs particles*, *Z. Phys. C* **70** (1996) 435–448, [hep-ph/9511342].

[177] P. Artoisenet, R. Frederix, O. Mattelaer and R. Rietkerk, *Automatic spin-entangled decays of heavy resonances in Monte Carlo simulations*, *JHEP* **03** (2013) 015, [1212.3460].

[178] S. Frixione, E. Laenen, P. Motylinski and B. R. Webber, *Angular correlations of lepton pairs from vector boson and top quark decays in Monte Carlo simulations*, *JHEP* **04** (2007) 081, [hep-ph/0702198].

[179] E. Alvarez, L. Da Rold, A. Juste, M. Szewc and T. Vazquez Schroeder, *A composite pNGB leptoquark at the LHC*, *JHEP* **12** (2018) 027, [1808.02063].

[180] P. Draper, T. Liu and C. E. Wagner, *Prospects for Higgs Searches at the Tevatron and LHC in the MSSM with Explicit CP-violation*, *Phys. Rev. D* **81** (2010) 015014, [0911.0034].

[181] E. Arganda, X. Marcano, N. I. Mileo, R. A. Morales and A. Szynkman, *Model-independent search strategy for the lepton-flavor-violating heavy Higgs boson decay to $\tau\mu$ at the LHC*, *Eur. Phys. J. C* **79** (2019) 738, [1906.08282].

[182] G. Cowan, K. Cranmer, E. Gross and O. Vitells, *Asymptotic formulae for likelihood-based tests of new physics*, *Eur. Phys. J. C* **71** (2011) 1554, [1007.1727]. [Erratum: Eur.Phys.J.C 73, 2501 (2013)].